INVESTIGATION OF DYNAMIC WAKE THEORY WITH RUN-TIME VARYING NUMBER OF DYNAMIC INFLOW STATES

A THESIS SUBMITTED TO
THE GRADUATE SCHOOL OF NATURAL AND APPLIED SCIENCES
OF
MIDDLE EAST TECHNICAL UNIVERSITY

BY

ALI KARAKAYA

IN PARTIAL FULFILLMENT OF THE REQUIREMENTS
FOR
THE DEGREE OF MASTER OF SCIENCE
IN
AEROSPACE ENGINEERING

NOVEMBER 2019

Approval of the thesis:

INVESTIGATION OF DYNAMIC WAKE THEORY WITH RUN-TIME VARYING NUMBER OF DYNAMIC INFLOW STATES

submitted by **ALI KARAKAYA** in partial fulfillment of the requirements for the degree of **Master of Science in Aerospace Engineering Department, Middle East Technical University** by,

Prof. Dr. Halil Kalıpçılar
Dean, Graduate School of **Natural and Applied Sciences** _____

Prof. Dr. İsmail Hakkı Tuncer
Head of Department, **Aerospace Engineering** _____

Assoc. Prof. Dr. İlkay Yavrucuk
Supervisor, **Aerospace Engineering, METU** _____

Examining Committee Members:

Prof. Dr. Ozan Tekinalp
Aerospace Engineering, METU _____

Assoc. Prof. Dr. İlkay Yavrucuk
Aerospace Engineering, METU _____

Prof. Dr. Metin Uymaz Salamcı
Mechanical Engineering, Gazi University _____

Assoc. Prof. Dr. Nilay Sezer Uzol
Aerospace Engineering, METU _____

Assist. Prof. Dr. Ali Türker Kutay
Aerospace Engineering, METU _____

Date: 21.11.2019

I hereby declare that all information in this document has been obtained and presented in accordance with academic rules and ethical conduct. I also declare that, as required by these rules and conduct, I have fully cited and referenced all material and results that are not original to this work.

Name, Surname: Ali Karakaya

Signature:

ABSTRACT

INVESTIGATION OF DYNAMIC WAKE THEORY WITH RUN-TIME VARYING NUMBER OF DYNAMIC INFLOW STATES

Karakaya, Ali
Master of Science, Aerospace Engineering
Supervisor: Assoc. Prof. Dr. İlkay Yavrucuk

November 2019, 125 pages

The effect of number of inflow states to inflow distribution is investigated when dynamic wake inflow is used to represent the rotor inflow. A simulation is set-up to be able to change the number of inflow states in run-time. The number of inflow states are changed with respect to advance ratio and the controls to the rotor. In this thesis, a new method to compute inflow distribution is proposed. The number of inflow states are decreased during run-time to reduce computation time when the higher state inflow models are not required. When conditions on the rotor requires higher state inflow models, the number of inflow states are increased to calculate inflow distribution.

Keywords: Helicopter, Rotor, Inflow, Peters – He, Rotor Simulation, Dynamic Wake Theory

ÖZ

DİNAMİK KUYRUKLU İÇ AKIŞ TEORİSİNİN DURUM DEĞİŞKENLERİ SAYISININ GERÇEK-ZAMANLI OLARAK DEĞİŞTİRİLEREK İNCELENMESİ

Karakaya, Ali
Yüksek Lisans, Havacılık ve Uzay Mühendisliği
Tez Danışmanı: Doç. Dr. İlkay Yavrucuk

Kasım 2019, 125 sayfa

Helikopter rotorlarının iç akışlarının modellenmesi için dinamik kuyruklu iç-akış teorisi kullanilmasi durumda, dinamik iç-akış durum değişkenlerinin sayısının iç-akış dağılımına etkisi incelenmektedir. İç-akış değişkenlerinin koşu-zamanında değiştirelebileceği bir simülasyon ortamı hazırlanmıştır. Durum değişkenlerinin sayısı helikopterin hızına ve rotora verilen kontrollere göre değiştirilmiştir. Bu tezde, iç-akış dağılımının hesaplanması için yeni bir method önerilmektedir. Yüksek durum değişkeni kullanan iç akış modellerine ihtiyaç duyulmadığı zamanlarda, durum değişkeni sayısının düşürülerek işlem süresinin kısaltılması sağlanmıştır. Uçuş koşulları yüksek durum değişkenli inflow modeli kullanılmasını gerektirdiği durumlarda ise durum değişkeni sayısı artırılarak iç-akış dağılımının hesaplanması sağlanmıştır.

Anahtar Kelimeler: Helikopter, Rotor, İç-Akış, Peters – He, Dinamik iç-akış kuyruk teorisi

To my family and friends

ACKNOWLEDGEMENTS

I would like to express my gratitude to Assoc. Prof. Dr. İlkay Yavrucuk for supervising this thesis study and introducing me to the field of helicopter modeling and control. He allowed this thesis to be my own work but steered me in the right direction whenever he thought I needed it.

I would like to extend my sincere thanks to examining committee members Prof. Dr. Ozan Tekinalp, Prof. Dr. Metin Salamcı, Assoc. Prof. Dr. Nilay Sezer Uzol and Assist. Prof. Dr. Ali Türker Kutay for their valuable comments and suggestions to improve my thesis.

I would like to express my gratitude to my former colleagues Dr. Sinan Özcan and Mustafa Gürler for our tough discussions about helicopter physics. That allow me to form a solid understanding of the helicopter physics and control. One of the biggest thanks belong to Anıl Öztürk who helped me to learn programming which I benefited to the limits while generating the codes used in thesis. His contributions to my career are invaluable.

I would like to express my sincere thanks to my dear friends, Çağatay Taşcı, Akif Altun, Esat Tavukçu, Gizem Ezgi Çınar, Aslıhan Altun, Yiğit Anıl Yücesan, Eren Narin and Himmet Arın Özkul. Without them, I could have finished my thesis earlier.

I would like to thank my parents Ayla and Alim Karakaya for their support and encouragement. All that I am, or hope to be, I owe to them. I also thank my sister Cansu Erdogan to let me be the bright one in the family.

Finally, I would like to thank to my beloved wife and love of my life İzel Baç for always being there for me. With her beside me, everything seems easy and fun.

TABLE OF CONTENTS

LIST OF TABLES

TABLES

LIST OF FIGURES

FIGURES

LIST OF SYMBOLS

$a_j^r(t),\ b_j^r(t)$	induced inflow states for cosine and sine terms
$\mathcal{A}[\cdot], \mathcal{B}[\cdot]$	linear operators representing mapping
A	rotor disc area
c	blade chord
C_L, C_D	lift and drag coefficients
$C_n^m(t),\ D_n^m(t)$	arbitrary Coefficients of the harmonics
e	non-dimensional hinge offset
i	imaginary number
j, n	polynomial number
$[L]$	gain matrix
$[L_{jn}^{rm(c)}]$	cosine part of [L] gain matrix
$[L_{jn}^{rm(s)}]$	sine part of [L] gain matrix
L_q	blade section lift
m, r	harmonic number
$[M]$	apparent mass matrix
P	pressure across disc
$P_n^m(v)$	associated Legendre function of the first kind
$\bar{P}_n^m(v)$	normalized Legendre function
$Q_n^m(i\eta)$	associated Legendre function of the second kind
$\bar{Q}_n^m(i\eta)$	normalized Legendre function
Q	number of blade elements
q	blade element identifier
p, q, r	body angular velocities
R	rotor radius
t	time
$\bar{t}$	non-dimensional time, $\bar{t} = \Omega t$

V_T	total flow at rotor
V_∞	free-stream velocity
w, v_i	normal component of the induced flow, positive downward
X	function of skew angle, $X = \tan\left(\left\|\frac{\chi}{2}\right\|\right)$
x, y, z	rotor

Greek Symbols

α	angle between free-stream and rotor disc
α_{eff}	effective angle of attack
α_j^r, β_j^r	induced inflow states for cosine and sine terms
β	flapping angle, $\beta = \beta_0 + \beta_{1c}\cos(\psi) + \beta_{1s}\sin(\psi)$
$\beta_0,\ \beta_{1c}, \beta_{1s}$	coning angle, longitudinal flapping angle, lateral flapping angle
δ_{ij}	kronecker delta
χ	wake skew angle
θ	blade pitch angle, $\theta = \theta_0 + \theta_{1c}\sin(\psi) + \theta_{1s}\cos(\psi)$
$\theta_0, \theta_{1c}, \theta_{1s}$	collective blade pitch angle, lateral blade pitch angle, longitudinal blade pitch angle
λ	non-dimensional total inflow through rotor disc, $\lambda = \lambda_{v_\infty} + \lambda_m$
λ_{v_∞}	non-dimensional inflow through rotor disc due to incoming velocity
λ_m	non-dimensional mean inflow, $\lambda_m = \sqrt{3}\, a_1^0$
μ	advance ratio of rotor
$v, \eta, \bar{\psi}$	ellipsoidal coordinate system
ξ	coordinate along free-stream, positive to upstream
ρ	density
σ	rotor solidity
τ_n^{mc}, τ_n^{ms}	cosine and sine parts of pressure coefficients

Φ	pressure function
ψ	azimuth location on rotor disc
$\Psi_j^r(\bar{r})$	general expression function
Ω	rotational speed

Superscripts

$(\cdot)^{(c)}$	cosine element
$(\cdot)^{(s)}$	sine element
$(\cdot)^{(time)}$	time element
$(\cdot)^{(convection)}$	convection element
$(\dot{\cdot})$	time derivative $\frac{\partial(\cdot)}{\partial t}$
$(\cdot)^*$	non-dimensional time derivative $\frac{\partial(\cdot)}{\partial \bar{t}}$

Subscripts

$(\cdot)_q$	q'th blade element
$(\cdot)_n$	n'th blade

CHAPTER 1

INTRODUCTION

1.1. Introduction

Mathematical modeling of physical systems come to play a significant role in design and development of electro-mechanical systems. Especially in aerospace applications, due to its expensive development and operational costs, engineers mostly rely on computer simulations to drive their overall designs and control systems. In addition, these simulations are used extensively used to train operators of these aerospace platforms.

In rotorcraft applications, the main contributor to system behavior is its rotor. Thus, engineers are researching more reliable, more accurate models to represent rotor dynamics realistically. Modeling of a rotor is mainly centered around the flapping of the rotor blades and the inflow motion through the rotor disc. The differential equations representing these dynamics do not have explicit solutions and they are required to be solved simultaneously. However, for such solutions there are two options besides the dynamic wake inflow model.[6][7] First one is the quasi-steady, two-dimensional momentum theory which results in static inflow with crude approximation, and the second one is the highly sophisticated computation intensive three-dimensional vortex theory. The latter includes a full aerodynamic analysis of the flow in and around the rotor and capable of predicting fuselage interactions. Therefore, it is impractical for real-time applications. In the middle ground, there is the dynamic inflow theory of Peters – He. It is basically a theory of an unsteady aerodynamics over the actuator disc exited by the rotor lift. The number of the states which used to represent Peters – He inflow is dictated by the engineer with respect to the application type.

1.2. Literature Review

The behavior of a generic helicopter mainly depends on the behavior of its main rotor. This led scientist and engineers to develop sophisticated models for blade motion during its operation. However, the mathematical rotor models of the past were lacking the comparable level of detail in its aerodynamic counterpart. In the core of rotor aerodynamic lies the induced inflow at the rotor and its proximity.[7] In the past, most models used the uniform inflow approach to reduce the computational intensity to stay relevant in the real-time simulations. However, the exponential growth of the computational capabilities of the last decades enabled more detailed and complex inflow representations to be implemented for real-time environments.

The methods of representing the induced inflow are categorized like the following figure.

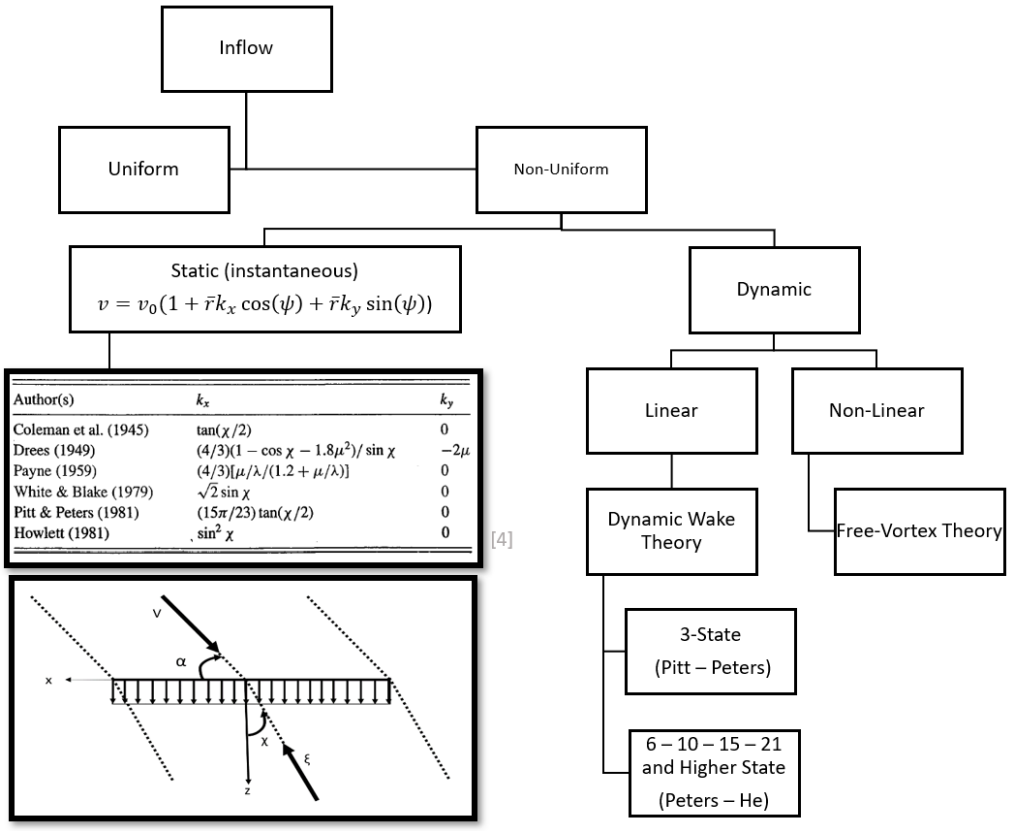

Author(s)	k_x	k_y
Coleman et al. (1945)	$\tan(\chi/2)$	0
Drees (1949)	$(4/3)(1 - \cos\chi - 1.8\mu^2)/\sin\chi$	-2μ
Payne (1959)	$(4/3)[\mu/\lambda/(1.2 + \mu/\lambda)]$	0
White & Blake (1979)	$\sqrt{2}\sin\chi$	0
Pitt & Peters (1981)	$(15\pi/23)\tan(\chi/2)$	0
Howlett (1981)	$\sin^2\chi$	0

[4]

Figure 1.1. Methods of Inflow Modeling

In the early days of inflow modelling, the uniform inflow was the only options. In hovering conditions, the performance of the uniform inflow is relatively good due to the symmetrical conditions on the rotor. [12] In the forward flight conditions, this inflow becomes highly asymmetrical due to the relative velocities experienced by the blade along the radius. In order to better represent the inflow, in 1926 Glauert[13] suggested a longitudinal variation using the following formula:

$$v_i = v_0(1 + \bar{r}\, k_x \cos(\psi)) \tag{1.1}$$

Where the v_0 is the uniform inflow, $\bar{r}$ is the non-dimensional distance from root to blade location, k_x is the variation coefficient in the longitudinal axis and ψ is the azimuthal location on the rotor.

This formula is merely a geometrical remapping of the uniform inflow on the rotor disc meaning that the overall integration of the non-uniform inflow is same as that of the uniform inflow. This formula is the root of the non-uniform, static inflow. After this formulation, a great effort is made determine the value of the k_x value. In 1934 Wheatley [45] suggested that using $k_x = 0.5$ results better correlation with the experimental data. Wheatley also stated that without an accurate inflow distribution model, the motion of the model cannot be determined. Then, in his paper Coleman et. al. [8] a cylindrical rotor wake and linked the k_x value with the skew angle of the rotor wake. They proposed a longitudinal variation $k_x = \tan\left(\frac{\chi}{2}\right)$ Figure 2.2. However, Brotherhood [5] investigated the flight tests and showed that the value for k_x was in the range from 1.3 to 1.6 for advance ratios 0.14 to 0.19. This study showed that Coleman underestimated the values of k_x meaning that the longitudinal variation was greater than initially thought. Later Drees [10] proposed a variation which accounts for the advance ratio of the helicopter rotor. He also proposed a variation in the lateral axis in the following form.

$$v_i = v_0(1 + \bar{r}\, k_x \cos(\psi) + \bar{r}\, k_y \sin(\psi)) \tag{1.2}$$

He suggested the following values for k_x and k_y:

$$k_x = \frac{4}{3}\left(1 - \cos(\chi) - 1.8\mu^2\right) / \sin(\chi) \tag{1.3}$$

$$k_y = -2\mu \tag{1.4}$$

For a period, the only way to estimate inflow was to find these k_x and k_y . The following table shows some suggested values for k_x throughout the inflow modeling history.

Table 1.1 *Suggested k_x values*

Authors	k_x
Payne [33]	$\frac{4}{3}\frac{\mu}{\lambda_0}\frac{1}{\left(1+\frac{\mu}{\lambda}\right)}$
White & Blake [46]	$\sqrt{2}\sin(\chi)$
Pitt & Peters [39]	$\left(\frac{15\pi}{23}\right)\tan\left(\frac{\chi}{2}\right)$
Howlett[22]	$\sin^2(\chi)$

Using the table above, the static prediction of the inflow can be made at different flight conditions. The skew angle greatly affected by the angle of attack of the rotor disc plane and forward velocities of the helicopter. The detailed comparison of these static models at different flight conditions are presented in the Chen's paper. [7].

Although static models were widely used, they lack the transient behavior which observed in the experiments. This lead the study of Carpenter and Fridovich [7]. They observed the time delay between the sudden pitch changes on the blade and the thrust and inflow response. Inflow was lagging behind the inputs. This clearly showed that the induced inflow created inertia effects. Therefore, the requirement for a dynamic inflow theory arose. These inertial effects were named as apparent mass of the flow which then used to account for the acceleration of the stagnant flow. The inclusion of these dynamic effects resulted better correlation with the experimental data especially below 0.4 advance ratios [2].

The early work on the dynamic inflow was made by Sissingh. [42] He employed the instantaneous thrust and inflow perturbations to deduce the linear relations between two phenomena. He also showed that the dynamic effects of inflow improved the damping of helicopter during pitch and roll maneuvers. Later, Curtiss and Shupe [9] formulated the dynamic relation between the induced inflow and the flapping behavior using equivalent Lock number.

$$\dot{\gamma} = \frac{\gamma}{1 + \frac{\partial \sigma}{\partial v_i}} \tag{1.5}$$

Where γ is the equivalent Lock number and σ is the rotor solidity. However, the first formulation of the dynamic inflow as it is known made by the Ormiston and Peters [31]. They expressed the dynamic inflow in the following matrix form:

$$\begin{Bmatrix} w_0 \\ w_s \\ w_c \end{Bmatrix} = \frac{1}{\mu} \begin{bmatrix} \frac{1}{2} & 0 & 0 \\ 0 & -\frac{3}{2} & 0 \\ 0 & 0 & -\frac{3}{2} \end{bmatrix} \begin{Bmatrix} C_T \\ C_L \\ C_M \end{Bmatrix} \tag{1.6}$$

Where $K_m = \frac{8}{3\pi}$, $K_I = \frac{16}{45\pi}$, and

$$V = \frac{\mu^2 + \lambda(\lambda + \lambda_{mean})}{\sqrt{(\mu^2 + \lambda^2)}}$$

Above values are the empirical observations made by Pitt and Peters. Following this new method, Peters work on a generalized version of this three-state dynamic inflow model. [35][37] The general form of the generalized dynamic wake theory is in the following form:

$$\left[M_{nj}^{mr}\right]\left\{\begin{matrix}\vdots\\ \{a_j^r\}\\ \vdots\end{matrix}\right\}^{*} + \left[L_{nj}^{mr(c)}\right]^{-1}\left\{\begin{matrix}\vdots\\ \{a_j^r\}\\ \vdots\end{matrix}\right\} = \left\{\begin{matrix}\vdots\\ \{\tau_n^{m(c)}\}\\ \vdots\end{matrix}\right\} \tag{1.7}$$

$$\left[M_{nj}^{mr}\right]\left\{\begin{matrix}\vdots\\ \{b_j^r\}\\ \vdots\end{matrix}\right\}^{*} + \left[L_{nj}^{mr(s)}\right]^{-1}\left\{\begin{matrix}\vdots\\ \{b_j^r\}\\ \vdots\end{matrix}\right\} = \left\{\begin{matrix}\vdots\\ \{\tau_n^{m(s)}\}\\ \vdots\end{matrix}\right\} \tag{1.8}$$

The detailed derivation of this theory is given in the Chapter 2. This solution formulated by Peters and He rely on the acceleration potential on the elliptic coordinates and assumes the wake as a cylindrical dynamic wake. This theory offers a solution for inflow which is expressed by Fourier series in azimuth variation and Legendre functions in radial variation. [14]

In 2009, Van Hoydonck et.al.[43] reviewed the modern solutions for inflow which use the free-vortex computation. Free-Vortex method makes less assumption about the wake and let it evolve freely in its own influence. They concluded that a completely-free-vortex theory took multiple days to compute a 10 seconds maneuver. As the constraints on the wake are increased, the solution time is shortened to real-time. In addition, they also stated that the dynamic inflow models still have their use in the flight simulator models.

Murakami [29] extended the usage of Peters – He dynamic wake theory to be applicable on autorotation.

Guner et.al. [15] compared the fidelity of the above-mentioned inflow models. They concluded that the greater number of inflow states increased the correleation between experimental data in high asymmetry flight conditions such as high advance ratio conditions. They also concluded that during symmetrical flight condition, such as hovering flight, the higher number of inflow states do not contribute to the fidelity of the inflow model.

1.3. Objective of the Thesis

The inflow models that are mentioned in the literature survey section have their usage in the rotor simulations. These models are implemented beforehand the simulations and do not change throughout the simulation run. High state models take more time to compute whereas low-state models can not cover all flight conditions in acceptable fidelity. Therefore, a problem of simulation fidelity and computation time arise.

In this thesis, a new method to implement dynamic wake theory is proposed which changes its active inflow states during run-time with respect to some flight conditions. Objective of this work is to construct a logic to adjust the number of dynamic inflow states to reduce computation time while keeping a low deviation from high-state inflow models. In this new method, the switching logic of the dynamic inflow states are investigated with respect to advance ratio and with respect to pilot controls, collective and cyclics.

The number of inflow states greatly affect the distribution of inflow over the rotor disc. Especially in highly asymmetric conditions, low-state dynamic inflow models deviates from the high-state models. In this thesis, these conditions are tried to be isolated and investigated. Main contributor to this asymmetry is found to be the advance ratio and cyclic & collective control inputs. The state-number switching logic is emerged from these isolated tests and depends on the thresholds for advance ratio and controls.

In this thesis, a varying state inflow model is employed to represent the induced velocity field over an actuator disc. Two simulations which represent a flight envelope are run. The computation times of these simulations are compared.

1.4. Organization of the Thesis

In chapter 1, a brief introduction to thesis is made. Also, the objective of the thesis and the organization of the thesis are included in this section. In chapter 2, the analytical derivation to the generalized dynamic wake inflow model is made. In Chapter 3, an

attempt is made to generate a procedure to implement varying-state dynamic inflow model. In Chapter 4, the simple rotor model is introduced. In Chapter 5, total of 96 simulation runs are made and presented. These tests are used to create a state-number switching logic. In Chapter 6, the state-number switching logic is explained and two long simulations are made to assess the performance of varying-state inflow model. In Chapter 7, the conclusion to the thesis is made.

CHAPTER 2

FORMULATION OF DYNAMIC WAKE INFLOW THEORY

2.1. Background and Fundamental Equations

The dynamic wake inflow theory is a rotor disk inflow theory that is based on conservation of mass (continuity equation) and conservation momentum [35]. The continuity equation is given as follows:

$$\frac{\partial \rho}{\partial t} + \nabla \cdot (\rho \mathrm{V}) = 0 \tag{2.1}$$

where ρ is the density, t is time and V is the flow velocity vector field. However, in dynamic wake inflow theory, the fluid is assumed to be incompressible meaning that the density is constant. Therefore the Eq. (*2.1*) can be written as:

$$\nabla \cdot \mathrm{V} = 0 \tag{2.2}$$

The behavior of flow is described by Navier – Stokes equation:

$$\frac{\partial V}{\partial t} + (V \cdot \nabla)V = -\nabla \Phi + \nu \Delta V \tag{2.3}$$

where the ν is viscosity. However, fluid is assumed to be inviscid meaning that $\nu = 0$ and the flow is governed by the Euler equation given in Eq. (*2.4*)

$$\frac{\partial V}{\partial t} + (V \cdot \nabla)V = -\nabla \Phi \tag{2.4}$$

where Φ is the pressure potential function driving the flow. The dynamic inflow model is basically a set of linear equations. However, the Eq. (*2.4*) represents a non-linear behavior that requires to be linearized.

It is beneficial to divide Eq. (*2.4*) into two terms, time derivative term (unsteadiness) and spatial derivate term (convection). In order to linearize the non-linear convection term, $(V \cdot \nabla)V$, the flow velocity is written as $V = V_s + v$ where V_s is the steady flow and v is the perturbation.

$$\begin{aligned} &(V \cdot \nabla)V = 0 \text{ can be expanded as,} \\ &(V \cdot \nabla)V = \big((V_s + v) \cdot \nabla\big)(V_s + v) \\ &(V \cdot \nabla)V = V_s \cdot \nabla V_s + v \cdot \nabla V_s + V_s \cdot \nabla v + v \cdot \nabla v \end{aligned} \tag{2.5}$$

since the V_s is the steady flow (e.g. $\nabla V_s = 0$), Eq. (*2.5*) can be rearranged as following:

$$(V \cdot \nabla)V = V_s \cdot \nabla v + v \cdot \nabla v \tag{2.6}$$

The term $(v \cdot \nabla v)$ is a higher order error which can be neglected for this context. [11]

In addition, the time derivative term can be written as:

$$\frac{\partial V}{\partial t} = \frac{\partial (V_s + v)}{\partial t} \tag{2.7}$$

$$\frac{\partial V}{\partial t} = \frac{\partial (V_s)}{\partial t} + \frac{\partial (v)}{\partial t} \text{ , } and \frac{\partial V_s}{\partial t} = 0 \tag{2.8}$$

Finally, the combining Eq. (*2.6*) and (*2.8*) into Eq. (*2.4*):

$$\frac{\partial (v)}{\partial t} + V_s \cdot \nabla v = -\nabla \Phi \tag{2.9}$$

In Eq. (2.9), it is easier to see that the v is the induced velocity in the rotor disc. Basically, the equation defines that, for a velocity field over the rotor disc, the change of the momentum of the flow is caused by the change in the pressure field, namely the lift force generated by the rotor disc.[35] This lift can be better explained as a

discontinuous momentum change in the upper & lower sides of the rotor disc. The Peters – He inflow model is based on this principle.

From Eq. (*2.9*) both unsteadiness of the flow and the spatial variation of the flow contribute to the spatial variation of the pressure gradient. Therefore, the pressure difference can be written as:

$$\Phi = \Phi^{(\text{time})} + \Phi^{(convection)} \tag{2.10}$$

where $\Phi^{(convection)}$ is the pressure gradient that is generated by the spatial variation of the velocity field and $\Phi^{(time)}$ is the pressure gradient that is generated by the time derivative of the velocity field.

In references [19], [29], [35], [38] and [39] it is suggested that the Eq. (*2.10*) shall be written as follows:

$$\frac{\partial(v)}{\partial t} = -\nabla\Phi^{(time)} \quad , \qquad V_s \cdot \nabla v = \nabla\Phi^{(convection)} \tag{2.11}$$

When both equations in Eq. (*2.11*) are multiplied by ∇ Eq. (*2.12*) are obtained.

$$\nabla\left(\frac{\partial(v)}{\partial t}\right) = -\nabla^2\Phi^{(time)} \tag{2.12}$$

$$\nabla(V_s \cdot \nabla v) = \nabla^2\Phi^{(convection)} \tag{2.13}$$

In Eq. (*2.12*) left – hand side is the time dependent derivative of the velocity field. Therefore, the spatial derivation of the term is zero. In addition, combining the Eq. (*2.13*) with the Eq. (*2.2*), for incompressible flow, the term $\nabla(V_s \cdot \nabla v)$ becomes zero. Finally, following Laplace's equations for the pressure potential function can be written.

$$\nabla^2\Phi^{(time)} = 0 \tag{2.14}$$

$$\nabla^2\Phi^{(convection)} = 0 \tag{2.15}$$

$$\nabla^2\Phi = \nabla^2\Phi^{(convection)} + \nabla^2\Phi^{(time)} = 0 \tag{2.16}$$

The Eq. *(2.14)* and *(2.15)* are in the form of an acceleration potential and there exist an analytical solution to acceleration potential function [44]. Thus, the derivation of the Eq. *(2.16)* are essential for the formulation of Peters – He inflow. In order to solve these equations, following boundary conditions are defined [36].

- The pressure distribution is required to be linearly proportional to the disc loading. Since the Eq. (2.9) is linearized, disc loading is directly proportional to the induced velocity [28].

- The Pressure distribution is required to be zero at infinity.

- Becomes zero at the edge of the rotor.

In refs. [19], [29], [35] and [36] it is stated that when the Laplace's equation is written in ellipsoidal coordinate system (see the Appendix A), the Eq. *(2.16)* defining a pressure distribution on a circular disc can be solved by using the separation of variables method. When the boundary conditions are applied in ellipsoidal coordinate system, following solution for the pressure distribution is proposed from Prandtl's potential function.

$$\Phi(v,\eta,\bar{\psi},\bar{t}) = \sum_{m=0}^{\infty}\sum_{n=m+1,m+3,\ldots}^{\infty} P_n^m(v)Q_n^m(i\eta)[C_n^m(\bar{t})\cos(m\bar{\psi}) + D_n^m(\bar{t})\sin(m\bar{\psi})] \tag{2.17}$$

where v, η and $\bar{\psi}$ are the coordinates of ellipsoidal coordinate system.

Note that the variables $P_n^m(v)$ and $Q_n^m(i\eta)$ are called associated Legendre function of the first and second kind respectively. $C_n^m(t)$ and $D_n^m(\mathrm{t})$ are arbitrary coefficients of the harmonics.

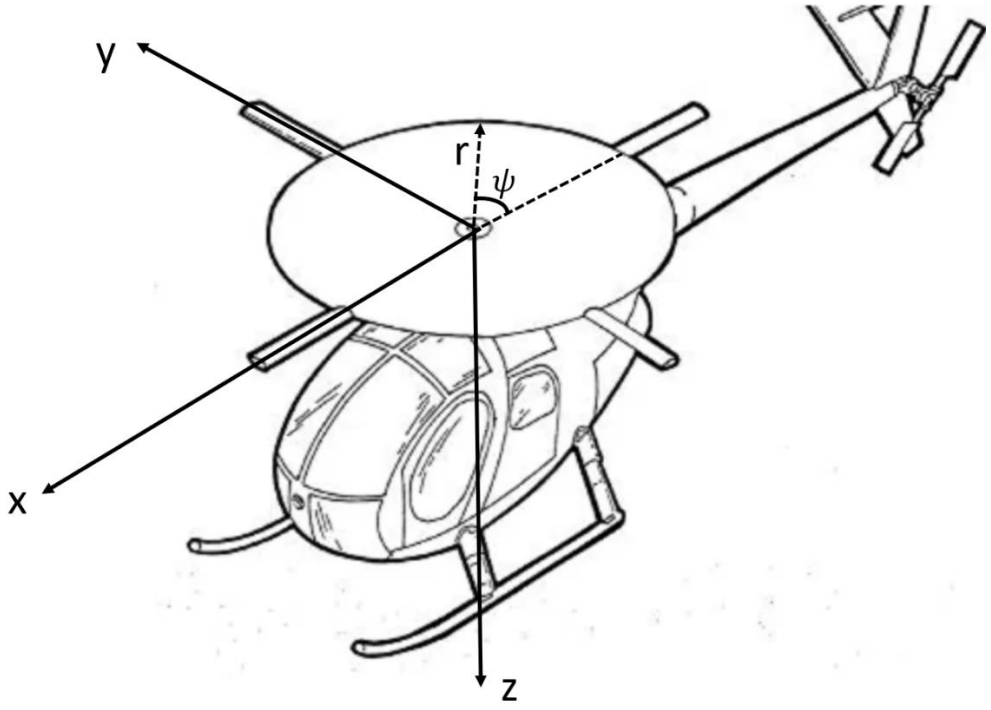

Figure 2.1. Rotor Disc Frame Cylindrical and Cartesian Coordinate System

The Eq. *(2.17)* defines the pressure field around the rotor. The difference of the pressure between upper and lower surfaces of the rotor results in the lift generated by the rotor. Therefore, upper and lower surfaces of the rotor need to be represented in the elliptical coordinate system.

In Figure 2.1, the cylindrical coordinate system is given where "r" represents rotor radius and "ψ" is the counter-clockwise azimuth angle. In both cartesian and

cylindrical coordinate system, z-axis is pointing downward through the vehicle body. In elliptical coordinates, rotor disc is represented as $\eta = 0$, $v = \sqrt{1 - \bar{r}^2}$ and $\bar{\psi} = \psi$, the region above the rotor disc is where $v < 0$ and the region below the rotor disc is where $v > 0$. Therefore, the pressure discontinuity on rotor disc is represented using appropriate η and v .

In elliptical coordinates the lower and upper surfaces can be represented as,

- $\Phi^{(upper)} = \Phi(\bar{r}, \psi, \bar{t})$ where $\eta = 0,\ v \to 0^-$
- $\Phi^{(lower)} = \Phi(\bar{r}, \psi, \bar{t})$ where $\eta = 0,\ v \to 0^+$

Then the rotor load can be written as:

$$P(\bar{r}, \psi, \bar{t}) = \Phi^{(upper)} - \Phi^{(lower)} \tag{2.18}$$

Plugging Eq. *(2.17)* into Eq. *(2.18)*:

$$\mathrm{P}(v, \bar{\psi}, \bar{t}) = -2 \sum_{m=0}^{\infty} \sum_{n=m+1,m+3,\ldots}^{\infty} P_n^m(v) Q_n^m(i0)[C_n^m(\bar{t}) \cos(m\bar{\psi}) + D_n^m(\bar{t}) \sin(m\bar{\psi})] \tag{2.19}$$

Rewriting the Eq. *(2.19)* in the following format [11]:

$$\mathrm{P}(v, \bar{\psi}, \bar{t}) = \sum_{m=0}^{\infty} \sum_{n=m+1,m+3,\ldots}^{\infty} \bar{P}_n^m(v)[\tau_n^{mc}(\bar{t}) \cos(m\bar{\psi}) + \tau_n^{ms}(\bar{t}) \sin(m\bar{\psi})] \tag{2.20}$$

Where the term $\left(-2 \cdot Q_n^m(i0)\right)$ is plugged in the coefficient terms $C_n^m(\bar{t})$ and $D_n^m(\bar{t})$. These terms are renamed as $\tau_n^{mc}(\bar{t})$ and $\tau_n^{ms}(\bar{t})$ and given as follows:

$$\bar{P}_n^m(v) = (-1)^m \frac{\bar{P}_n^m(v)}{\rho_n^m} \tag{2.21}$$

$$\rho_n^m = \frac{1}{2n+1}\frac{(n+m)!}{(n-m)!} \tag{2.22}$$

$$\tau_n^{mc} = (-1)^{m+1} 2 Q_n^m(i0) \rho_n^m C_n^m \tag{2.23}$$

$$\tau_n^{ms} = (-1)^{m+1} 2 Q_n^m(i0) \rho_n^m D_n^m \tag{2.24}$$

The Eq. *(2.20)* can be divided into time – dependent contributions and convection contributions.

$$\mathrm{P}^{(\mathrm{time})}(v, \bar{\psi}, \bar{t}) = \sum_{m=0}^{\infty} \sum_{n=m+1,m+3,\ldots}^{\infty} \bar{P}_n^m(v)\left[\tau_n^{mc}(\bar{t})^{(time)} \cos(m\bar{\psi}) + \tau_n^{ms}(\bar{t})^{(\mathrm{time})} \sin(m\bar{\psi})\right] \tag{2.25}$$

$$\mathrm{P}^{(\mathrm{conv})}(v, \bar{\psi}, \bar{t}) = \sum_{m=0}^{\infty} \sum_{n=m+1,m+3,\ldots}^{\infty} \bar{P}_n^m(v)\left[\tau_n^{mc}(\bar{t})^{(\mathrm{conv})} \cos(m\bar{\psi}) + \tau_n^{ms}(\bar{t})^{(\mathrm{conv})} \sin(m\bar{\psi})\right] \tag{2.26}$$

In Eq. *(2.25)* and Eq. *(2.26)* terms $\tau_n^{mc}(\bar{t})^{(time)}$, $\tau_n^{ms}(\bar{t})^{(\mathrm{time})}$, $\tau_n^{mc}(\bar{t})^{(\mathrm{conv})}$ and $\tau_n^{ms}(\bar{t})^{(\mathrm{conv})}$ are the Fourier coefficients. In order to determine these coefficients, the rotor loading, namely the lift, needs to be calculated.

In the context of induced inflow, the induced inflow, v, is a vector which have three induced inflow components in space such that $\vec{v} = (u, v, w)$. The radial and azimuthal components of the induced inflow, u and v respectively, are negligible compared to the normal component of the inflow, namely w. In fact, in the literature the term induced inflow directly refers to the w of $\vec{v}$. [19][35]

In the equations, *(2.17)* to *(2.26)*, the effort is to determine $\nabla\Phi^{(time)}$ and $\nabla\Phi^{(convection)}$. However, to establish a link between induced inflow and pressure potential, Eq. *(2.11)* is addressed below.

Firstly, the time dependent term of Eq. *(2.11)* is rewritten using only the normal component of the induced inflow.

$$\frac{\partial(w)}{\partial t} = -\frac{\partial\Phi^{(time)}}{\partial z} \ , at\ \eta = 0\ , (across\ the\ rotor\ disc) \tag{2.27}$$

Note that Eq. *(2.27)* fundamentally implies that the difference in time – dependent component of pressure distribution above and below of the surface of the rotor disc gives the acceleration of the induced inflow.

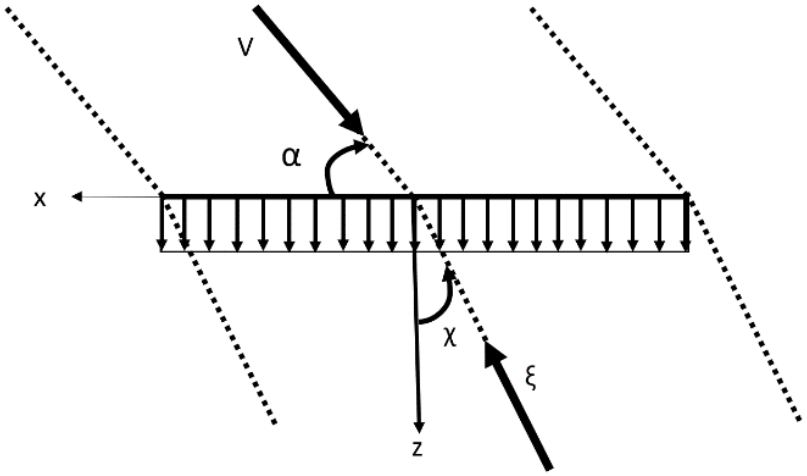

Figure 2.2. Streamline Coordinate System

In (Figure 2.2) α is the angle between rotor disc and the free-stream velocity. The flow passing through the rotor disc combined with the induced inflow skews into the normal of the disc. Therefore, the angle between normal of the rotor disc and the flow below the rotor is called the skew angle (χ) .

Secondly, when written in the streamline coordinate system, the inflow through the rotor disc becomes a scalar, because the direction of the inflow is selected as the $\xi - axis$ by definition. Therefore, the convection term of the Eq. *(2.11)* becomes as follows:

$$V_s \cdot \frac{\partial w}{\partial \xi} = -\frac{\partial \Phi^{(conv)}}{\partial z}\ , at\ \eta = 0, (across\ the\ rotor\ disc) \tag{2.28}$$

Equations *(2.27)* and *(2.28)* are the differential equations which relates the lift to the inflow distribution across the rotor disc. The solutions to these differential equations complete the Peters – He inflow model.

$$\frac{\partial (w)}{\partial t} = -\frac{\partial \Phi^{(time)}}{\partial z}\bigg|_{\eta=0} \tag{2.29}$$

$$w = \frac{1}{V_s}\int_{\infty}^{0} \frac{\partial \Phi^{(c)}}{\partial z}\ \partial \xi \tag{2.30}$$

The pressure discontinuity functions defined in Eq. *(2.25)* and *(2.26)* are linear functions that are generated by the superposition of the $\tau_n^{mc}(t)^{(time)}$, $\tau_n^{ms}(t)^{(\mathrm{time})}$, $\tau_n^{mc}(t)^{(\mathrm{conv})}$. Therefore, the mapping of these equations can be represented by linear operations $\mathcal{A}\left[\Phi^{(t)}\right]$ and $\mathcal{B}\left[\Phi^{(c)}\right]$. Note that the set ($\tau_n^{mc}(t)^{(time)}$, $\tau_n^{ms}(t)^{(\mathrm{time})}$, $\tau_n^{mc}(t)^{(\mathrm{conv})}$) consists of linearly independent elements, since they are generated by the associated Legendre function of the second kind which itself defines an orthonormal set [30].

The Eq. *(2.29)* and Eq. *(2.30)* can be rewritten as:

$$\frac{\partial (w)}{\partial t} \equiv -\frac{\partial \Phi^{(time)}}{\partial z}\bigg|_{\eta=0} \equiv \mathcal{A}\left[\Phi^{(time)}\right] \tag{2.31}$$

$$w = \frac{1}{V_s}\int_{\infty}^{0} \frac{\partial \Phi^{(conv)}}{\partial z}\ \partial \xi \equiv \mathcal{B}\left[\Phi^{(conv)}\right] \tag{2.32}$$

When a proper series is selected in order to expand the induced flow, the linear mapping $\mathcal{A}\left[\Phi^{(t)}\right]$ and $\mathcal{B}\left[\Phi^{(c)}\right]$ becomes invertible [19][35]. Then Eq. *(2.29)* and Eq. *(2.30)* are rearranged as follows:

$$\mathcal{A}^{-1}[\dot{w}] = \Phi^{(time)}, \qquad where\ \dot{w} = \frac{\partial w}{\partial \bar{t}} \tag{2.33}$$

$$\mathcal{B}^{-1}[w] = \Phi^{(\mathrm{conv})} \tag{2.34}$$

$$\mathcal{A}^{-1}[\dot{w}] + \mathcal{B}^{-1}[w] = \Phi^{(time)} + \Phi^{(\mathrm{conv})} = \Phi \tag{2.35}$$

2.2. Matrix Form

The Inflow distribution can be expanded as the pressure distribution formulated by Eq. *(2.17)* . Such expansion of the inflow accounts for the radial distribution and harmonic distribution on azimuth. The Fourier series expansion of the induced inflow is given as follows:

$$w(\bar{r}, \psi, \bar{t}) =$$

$$\sum_{r=0}^{\infty} \sum_{j=r+1,r+3,\ldots}^{\infty} \Psi_j^r(\bar{r})\left[a_j^r(\bar{t})\cos(r\psi) + b_j^r(\bar{t})\sin(r\psi)\right] \tag{2.36}$$

In Eq. *(2.36)* the well-known Peters – He induced inflow is formulated. Where,

Ψ_j^r : The radial distribution function,

a_j^r : Time dependent cosine coefficient state of inflow,

b_j^r : Time dependent sine coefficient state of inflow.

Note that the values r and j in above equation (*2.36*) dictates the final state number of the Peters – He inflow model, whose effects are investigated throughout this thesis.

The radial distribution function, $\Psi_j^r(\bar{r})$, can be chosen as:

$$\Psi_j^r(\bar{r}) = \frac{1}{v}\,\bar{P}_j^r(v) \tag{2.37}$$

which is expanded as follows:

$$\Psi_j^r(\bar{r}) = \sqrt{(2j+1)H_j^r} \sum_{q=r,r+2,\dots}^{j-1} r^{-q}\,\frac{(-1)^{\frac{(q-r)}{2}}(j+q)!!}{(q-r)!!\,(q+r)!!\,(j-q-1)!!} \tag{2.38}$$

Note that the radial expansion function has either only even or only odd power of $\bar{r}$.

where,

$$H_j^r = \frac{(j+r-1)!!\,(j-r-1)!!}{(j+r)!!\,(j-r)!!} \tag{2.39}$$

In Eq. *(2.35)* the equation $\Phi^{(time)} + \Phi^{(\mathrm{conv})} = \Phi$ is defined. Plugging Eq.*(2.33)* and *(2.34)* , and decoupling cosine and sine equations, the Eq. *(2.35)* can be rearranged in the following form:

$$\mathcal{A}^{(c)-1}\begin{Bmatrix}\vdots\\ \{a_j^r\}\\ \vdots\end{Bmatrix}^{*} + \mathcal{B}^{(c)-1}\begin{Bmatrix}\vdots\\ \{a_j^r\}\\ \vdots\end{Bmatrix} = \begin{Bmatrix}\vdots\\ \{\tau_n^{m(c)}\}\\ \vdots\end{Bmatrix} \tag{2.40}$$

$$\mathcal{A}^{(s)-1}\begin{Bmatrix}\vdots\\ \{b_j^r\}\\ \vdots\end{Bmatrix}^{*} + \mathcal{B}^{(s)-1}\begin{Bmatrix}\vdots\\ \{b_j^r\}\\ \vdots\end{Bmatrix} = \begin{Bmatrix}\vdots\\ \{\tau_n^{m(s)}\}\\ \vdots\end{Bmatrix} \tag{2.41}$$

With the Eq. *(2.40)* and *(2.41)*, the well-known Peters – He inflow model can be written as:

$$\left[M_{nj}^{mr}\right]\begin{Bmatrix}\vdots\\ \{a_j^r\}\\ \vdots\end{Bmatrix}^{*} + \left[L_{nj}^{mr(c)}\right]^{-1}\begin{Bmatrix}\vdots\\ \{a_j^r\}\\ \vdots\end{Bmatrix} = \begin{Bmatrix}\vdots\\ \{\tau_n^{m(c)}\}\\ \vdots\end{Bmatrix} \tag{2.42}$$

$$\left[M_{nj}^{mr}\right]\begin{Bmatrix}\vdots\\ \{b_j^r\}\\ \vdots\end{Bmatrix}^{*} + \left[L_{nj}^{mr(s)}\right]^{-1}\begin{Bmatrix}\vdots\\ \{b_j^r\}\\ \vdots\end{Bmatrix} = \begin{Bmatrix}\vdots\\ \{\tau_n^{m(s)}\}\\ \vdots\end{Bmatrix} \tag{2.43}$$

where M_{nj}^{mr} represents the inverse of linear operator $\mathcal{A}$, and the operators $L_{nj}^{mr\,(c)}$ and $L_{nj}^{mr\,(s)}$ are the linear operator $\mathcal{B}$ defined in the Eq.*(2.31)* and *(2.32)* respectively. Note that the $\left[M_{nj}^{mr}\right]$ matrix does not change for sine and cosine equations, since it is a mapping in time [29]. Furthermore, the behavior of the L-operators for sine and cosine matrices are uncoupled. This is explained in ref. [19] by the neglect of wake rotation effects.

In the next section computation of these matrices are investigated.

2.2.1. Computation of Apparent Mass Matrix [M]

The matrix [M] is the part that is associated with the acceleration of the flow, since it is the coefficient matrix of the time derivative of the velocity field states. Therefore, it is called as apparent mass matrix in this context.

In order to compute the elements of [M] matrix, the Eq. *(2.29)* is needed to be carried out. The Eq. *(2.29)* is written in the ellipsoidal coordinate system. Therefore, the operator $\frac{\partial}{\partial z}$ is redefined in the ellipsoidal coordinate system (See the appendix A) as:

$$\frac{\partial}{\partial z} = -\frac{1}{v^2+\eta^2}\left[\left(\eta(1-v^2)\frac{\partial}{\partial v}\right)+\left(v(1+\eta^2)\frac{\partial}{\partial \eta}\right)\right] \tag{2.44}$$

when $\eta = 0$ is applied in Eq. *(2.44)*, equation reduced to following form:

$$\frac{\partial}{\partial \eta} = -\frac{1}{v}\frac{\partial}{\partial \eta} \tag{2.45}$$

When Eq. *(2.27)* is solved with help of Eq. *(2.17)*, *(2.37)*, *(2.45)* following relations are obtained [23][11][19].

$$\dot{\alpha}_n^m = \left.\frac{d\bar{Q}_n^m(i\eta)}{\partial \eta}\right|_{\eta=0} (\tau_n^{mc})^{(time)} \tag{2.46}$$

$$\dot{\beta}_n^m = \left.\frac{d\bar{Q}_n^m(i\eta)}{\partial\eta}\right|_{\eta=0} (\tau_n^{ms})^{(time)} \tag{2.47}$$

Note that α_j^r and β_j^r are the induced inflow states (a_j^r and b_j^r) represented in $\frac{1}{v}\bar{P}_n^m$ orthonormal set such that:

$$\{a_j^r\} = [Y]\{\alpha_j^r\}, and\ \{b_j^r\} = [Y]\{\beta_j^r\}, \tag{2.48}$$

where [Y] is the mapping from the basis $\frac{1}{v}\bar{P}_n^m$ to basis $\frac{1}{v}\ \bar{P}_j^r(v)$, given in Eq. *(2.37)*. Note that the basis selection to solve Eq.*(2.45)* is identical to radial distribution function in Eq. *(2.37)* except the harmonics subscript.

In addition, the derivative which used in Eq.*(2.47)* and *(2.48)* evaluated as:

$$-\left.\frac{d\bar{Q}_n^m(i\eta)}{\partial\eta}\right|_{\eta=0} = \frac{\pi}{2}\ (H_n^m)^{-1} \equiv (K_n^m)^{-1} \tag{2.49}$$

Thus, the relation between $\dot{a}_n^m$ and $(\tau_n^{mc})^{(time)}$, and $\dot{b}_n^m$ and $(\tau_n^{ms})^{(time)}$ is shown.

Finally, the mass matrix [M] can be written as:

$$\left[M_{jn}^{rm}\right] = \begin{bmatrix} \ddots & & \\ & M_{jn}^{rm} & \\ & & \ddots \end{bmatrix} \tag{2.50}$$

$$M_{jn}^{rm} = K_{jn}^{rm}\delta_{jn}\delta_{rm} \tag{2.51}$$

where,

$$\delta_{jn} = 1 \text{ when j = n, and } \delta_{jn} = 0 \text{ elsewhere} \tag{2.52}$$

$$M_{jn}^{rm} = K_{jn}^{rm}\delta_{jn}\delta_{rm} = K_n^m = \frac{2}{\pi}\ H_n^m \tag{2.53}$$

Note that the matrix [M] is purely in diagonal form due to the terms $\delta_{jn}\delta_{rm}$ in Eq.*(2.51)*. As a result, there is no radial or harmonic coupling in this operator. This property of the mass matrix [M] simplifies the computation of time-response of the states and eigenvalue analysis [19].

2.2.2. Computation of Gain Matrix [L]

The [L] matrix is divided into two square matrices due to its uncoupled structure, $[L^{(c)}]$ and $[L^{(s)}]$ for the harmonic terms that are multiplying cosine and sine terms respectively. In order to compute matrix [L], Eq.*(2.17)* and *(2.36)* are substituted into Eq. *(2.32)*. and multiplied by either $\bar{P}_n^m(v)\cos(r\psi)$ or $\frac{1}{v}\bar{P}_n^m(v)\sin(r\psi)$.

In addition, elements in [L] matrix are divided by the free – stream velocity, such that the governing equation becomes:

$$\{c_j^r\} = \frac{1}{V_\infty}[\bar{L}]\left\{\tau_n^{m(c)^V}\right\}, \text{ where superscript V indicates the division by V.} \quad (2.54)$$

$$\{d_j^r\} = \frac{1}{V_\infty}[\bar{L}]\left\{\tau_n^{m(s)^V}\right\} \quad (2.55)$$

Note that c_j^r and d_j^r are the induced inflow states (a_j^r and b_j^r) represented in $\bar{P}_n^m$ orthonormal set. The following transformation relation in Eq. *(2.58)* can be made between given basis sets.

$$\{a_j^r\} = [Z]\{c_j^r\}, and\ \{b_j^r\} = [Z]\{c_j^r\}, \quad (2.56)$$

where [Z] is the mapping from the basis $\bar{P}_j^r(v)$ to basis $\frac{1}{v}\bar{P}_j^r(v)$, given in Eq. *(2.37)*,

These operation results in definition of following integrals.

$$\bar{L}_{jn}^{0mc} = \frac{1}{4\pi}\int_0^{2\pi}\int_0^{1}\bar{P}_j^0(v)\int_0^{\infty}\frac{\partial}{\partial z}\left[\bar{P}_j^0(v)\bar{Q}_j^m(i\eta)\right]\cos(m\psi)\,d\eta\,dv\,d\psi \tag{2.57}$$

$$\bar{L}_{jn}^{rm(c)} = \frac{1}{2\pi}\int_0^{2\pi}\int_0^{1}\bar{P}_j^0(v)\cos(\mathrm{r}\psi)\int_0^{\infty}\frac{\partial}{\partial z}\left[\bar{P}_j^0(v)\bar{Q}_j^m(i\eta)\right]\cos(m\psi)\,d\eta\,dv\,d\psi \tag{2.58}$$

$$\bar{L}_{jn}^{rm(s)} = \frac{1}{2\pi}\int_0^{2\pi}\int_0^{1}\bar{P}_j^0(v)\sin(\mathrm{r}\psi)\int_0^{\infty}\frac{\partial}{\partial z}\left[\bar{P}_j^0(v)\bar{Q}_j^m(i\eta)\right]\sin(m\psi)\,d\eta\,dv\,d\psi \tag{2.59}$$

The solutions to these integrals are highly complex, and it is out of the scope of this thesis. In the Refs. [19] and [28] a rigorous solution of these integrals is carried out and the results are presented below.

$$\left[\,\bar{L}_{jn}^{0m}\,\right]^{(c)} = (X^m)\left[\Lambda_{jn}^{0m}\right] \tag{2.60}$$

$$\left[\,\bar{L}_{jn}^{rm}\,\right]^{(c)} = \left(X^{|m-r|} + (-1)^{\ell}X^{|m+r|}\right)\left[\Lambda_{jn}^{rm}\right] \tag{2.61}$$

$$\left[\,\bar{L}_{jn}^{rm}\,\right]^{(s)} = \left(X^{|m-r|} - (-1)^{\ell}X^{|m+r|}\right)\left[\Lambda_{jn}^{rm}\right] \tag{2.62}$$

where $\ell = \min(r, m)$ and $X = \tan\left|\frac{\chi}{2}\right|$. Note that, χ is the skew angle given in Figure 2.2 .

$$\chi = \frac{\pi}{2} - \tan^{-1}\left|\frac{\lambda}{\mu}\right| \tag{2.63}$$

where λ is the total inflow due to both oncoming flow and induced inflow, and μ is the advance ratio of the rotor.

Generation of the gain matrix depends on the computation of variable Λ_{jn}^{rm}.

The function Λ_{jn}^{rm} is defined as follows [28][29][35]:

For r + m is odd, and n < r,

$$\Lambda_{jn}^{\mathrm{rm}} = 0 \tag{2.64}$$

For r + m is odd, and n ≥ r, and r > m,

$$\Lambda_{jn}^{\mathrm{rm}} = (-1)^{\frac{n+j-2r-1}{2}} \frac{\pi H_n^r}{\left(2\sqrt{H_n^m H_j^r}\right)} \frac{\sqrt{(2j+1)(2n+1)}}{(j-n)(n+j+1)} \tag{2.65}$$

For r + m is odd, and n ≥ r, and r < m,

$$\Lambda_{jn}^{\mathrm{rm}} = (-1)^{\frac{n+j-2r+1}{2}} \frac{\pi H_n^r}{\left(2\sqrt{H_n^m H_j^r}\right)} \frac{\sqrt{(2j+1)(2n+1)}}{(j-n)(n+j+1)} \tag{2.66}$$

For r + m is even, and n < r,

$$\Lambda_{jn}^{\mathrm{rm}} = \frac{(-1)^{\frac{n+j-2r}{2}}}{\sqrt{H_n^m H_j^r}} \frac{(m+r-1)!!\,(r-n-2)!!}{(n+r)!!\,(r-n-1)!!} \frac{\sqrt{(2j+1)(2n+1)}}{(j-n)(n+j+1)} \tag{2.67}$$

For r + m is even, and n ≥ r,

$$\Lambda_{jn}^{\mathrm{rm}} = \delta_{jn} \sqrt{\frac{H_j^r}{H_n^m}} \tag{2.68}$$

2.2.3. Combined Inflow Theory

In sections (2.2.1) and (2.2.2) the computation of matrices $[M]$ in basis $\frac{1}{v}\,\bar{P}_j^r(v)$, and $[\bar{L}]$ in $\bar{P}_j^r(v)$ is made. In addition, the transformation matrix [Y], from basis $\frac{1}{v}\,\bar{P}_j^r(v)$, to basis $\frac{1}{v}\,\bar{P}_j^r(v)$, and transformation matrix [Z], from basis $\bar{P}_j^r(v)$ to basis $\frac{1}{v}\,\bar{P}_j^r(v)$, are given in Eq. *(2.48)* and *(2.56)*. Using these matrices, matrix form of the Peters – He inflow can be constructed.

$$\begin{bmatrix} \ddots & & \\ & M & \\ & & \ddots \end{bmatrix} \begin{Bmatrix} \{\alpha, b\} \end{Bmatrix}^{*} + V_{\infty} \begin{bmatrix} \cdots & \vdots & \cdots \\ & \bar{L} & \\ & \vdots & \end{bmatrix}^{-1} \begin{Bmatrix} \{c, d\} \end{Bmatrix} = \begin{Bmatrix} \{\tau\} \end{Bmatrix} \tag{2.69}$$

Note that the states are not in the form of a and b . Therefore, Eq. *(2.69)* is expanded to give:

$$\begin{bmatrix} \ddots & & \\ & M & \\ & & \ddots \end{bmatrix}\begin{bmatrix} \ddots & & \\ & Y & \\ & & \ddots \end{bmatrix}\begin{Bmatrix} \{a,b\} \end{Bmatrix}^{*} +$$

$$V_{\infty}\begin{bmatrix} \cdots & \vdots & \cdots \\ & \bar{L} & \\ & \vdots & \end{bmatrix}\begin{bmatrix} \cdots & \vdots & \cdots \\ & Z & \\ & \vdots & \end{bmatrix}\begin{Bmatrix} \{a,b\} \end{Bmatrix} = \begin{Bmatrix} \{\tau\} \end{Bmatrix} \tag{2.70}$$

Rearranging Eq.*(2.70)* such that,

$$[M][Y] = [M], \tag{2.71}$$

$$[\bar{L}][Z] \ = [L] \tag{2.72}$$

Substituting Eq.*(2.71)* and *(2.72)* into Eq.*(2.70)*, well-known Peters – He inflow equations in matrix form is obtained.

$$\begin{bmatrix} \ddots & & \\ & K_n^m & \\ & & \ddots \end{bmatrix}\begin{Bmatrix} \{\alpha_j^r\} \end{Bmatrix}^{*} + [V]\begin{bmatrix} \cdots & \vdots & \cdots \\ & L_{jn}^{rm(c)} & \\ & \vdots & \end{bmatrix}^{-1}\begin{Bmatrix} \alpha_j^r \end{Bmatrix} = \begin{Bmatrix} \{\tau_j^{r(c)}\} \end{Bmatrix} \tag{2.73}$$

$$\begin{bmatrix} \ddots & & \\ & K_n^m & \\ & & \ddots \end{bmatrix}\begin{Bmatrix} \{\alpha_j^r\} \end{Bmatrix}^{*} + [V]\begin{bmatrix} \cdots & \vdots & \cdots \\ & L_{jn}^{rm(s)} & \\ & \vdots & \end{bmatrix}^{-1}\begin{Bmatrix} b_j^r \end{Bmatrix} = \begin{Bmatrix} \{\tau_j^{r(s)}\} \end{Bmatrix} \tag{2.74}$$

where K_n^m is computed as in Eq. *(2.53)*, and $\left[L_{jn}^{rm}\right]$ are computed as:

$$\left[L_{jn}^{0m}\right]^{(c)} = X^m\left[\Gamma_{jn}^{0m}\right] \tag{2.75}$$

$$\left[L_{jn}^{rm}\right]^{(c)} = \left[X^{|m-r|} + (-1)^{\ell}X^{|m+r|}\right]\left[\Gamma_{jn}^{rm}\right] \tag{2.76}$$

$$\left[L_{jn}^{rm}\right]^{(s)} = \left[X^{|m-r|} - (-1)^{\ell}X^{|m+r|}\right]\left[\Gamma_{jn}^{rm}\right] \tag{2.77}$$

where $\ell = \min(m,r)$ and $X = \tan\left(\frac{\chi}{2}\right)$. In addition, the Γ function is given below:

for r + m is even:

$$\Gamma_{jn}^{rm} = \frac{(-1)^{\frac{n+j-2r}{2}}}{\sqrt{(H_n^m)(H_j^r)}} \frac{2\sqrt{(2n+1)(2j+1)}}{(j+n)(j+n+2)[(j-n)^2-1]} \tag{2.78}$$

for r + m is odd and $j = n \pm 1$:

$$\Gamma_{jn}^{rm} = -\frac{\pi}{2\sqrt{(H_n^m)(H_j^r)}} \frac{sgn(r-m)}{\sqrt{(2n+1)(2j+1)}} \tag{2.79}$$

For r + m is odd and $j \neq n \pm 1$:

$$\Gamma_{jn}^{rm} = 0 \tag{2.80}$$

The forcing term of the dynamic inflow differential equation is $\tau_j^{r(s)}$and $\tau_j^{r(c)}$ which needs to be computed using a proper lift theory. (See Chapter 4)

2.2.4. V_∞ Contributions

In Eq. *(2.54)* and *(2.55)* the gain matrix [L] is divided by free stream velocity. In addition, in Eq. *(2.73)* and *(2.74)* V_∞ is replaced with an equivalent V matrix. This refinement of the theory accounts for the energy discontinuity in rotor.

In Ref. [25] it is suggested to use V as following:

$$[V] = \begin{bmatrix} V_{total} & & & \\ & V_s & & \\ & & V_s & \\ & & & \ddots \end{bmatrix} \tag{2.81}$$

where,

$$V_{total} = \sqrt{(\mu^2 + \lambda^2)} \tag{2.82}$$

$$V_s = \frac{\mu^2 + (\lambda + \lambda_m)\lambda}{V_{total}} \tag{2.83}$$

where,

λ: non-dimensional total inflow through rotor disc, $\lambda = \lambda_{V_\infty} + \lambda_m$

λ_{V_∞}: non-dimensional inflow through rotor disc due to oncoming flow of air.

λ_m: non-dimensional mean induced inflow given as follows:

$\lambda_m = \sqrt{3}\alpha_1^0$, where a_1^0 is the Peters – He inflow state for r = 0 and j =1

μ: advance ratio of rotor

The coupling between the state a_1^0 and the V_{total} introduces non-linearity to the inflow theory, such that V_{total} becomes dependent on the inflow states.

CHAPTER 3

IMPLEMENTATION OF PETERS – HE INFLOW THEORY

3.1. Introduction

In Chapter 2 theoretical background of the Peters – He inflow theory is briefly revisited. In Refs. [14],[19],[28],[29],[34],[35],[36],[38],[39] and [47] the details of the theory are rigorously studied, and the implementation of the theory is shown. However, where the mathematical rigor and complexity are increased in these studies, implementation clarity and simplicity fall short. Therefore, an attempt is made to generate a procedure which can be followed step-by-step and yield a complete inflow model.

3.2. Implementation of inflow theory

3.2.1. Selection of State Number

The number of Peters – He inflow states are dictated by the requirements of the application in which the model is generated. In Refs. [15] and [16], authors rigorously investigated the advantages and disadvantages of using different number of states while constructing Peters – He inflow model and break down the flight condition with respect to the fidelity compared to the number of inflow states. However, at this point of the thesis, the selection of the number of inflow states is merely to demonstrate the implementation and it is selected 21 – state arbitrarily.

In the Peters – He inflow model, the final inflow at station $\bar{r}, \psi$ and at time = t, is given in the Eq. *(2.36)*.

$$w(\bar{r}, \psi, \bar{t}) = \sum_{r=0}^{\infty} \sum_{j=r+1,r+3,\ldots}^{\infty} \Psi_j^r(\bar{r}) \left[a_j^r(\bar{t}) \cos(r\psi) + b_j^r(\bar{t}) \sin(r\psi) \right]$$

The inflow $w(\bar{r}, \psi, \bar{t})$ is represented as an infinite Fourier expansion. For practical purposes, Fourier expansion of the inflow function is required to be finite. Therefore, the harmonic expansion is determined using following table for r and j.

Table 3.1. *Choice for the Number of Spatial Modes*

Highest Power of r	j													Total Inflow States
	0	1	2	3	4	5	6	7	8	9	10	11	12	
0	1													1
1	1	1												3
2	2	1	1											6
3	2	2	1	1										10
4	3	2	2	1	1									15
5	3	3	2	2	1	1								21
6	4	3	3	2	2	1	1							28
7	4	4	3	3	2	2	1	1						36
8	5	4	4	3	3	2	2	1	1					45
9	5	5	4	4	3	3	2	2	1	1				55
10	6	5	5	4	4	3	3	2	2	1	1			66
11	6	6	5	5	4	4	3	3	2	2	1	1		78
12	7	6	6	5	5	4	4	3	3	2	2	1	1	91

The value of the r determines the harmonic variation in azimuth and radial distribution of the inflow. To illustrate, for the selected value of $r = 7$ following row of the Table 3.1 is of importance:

Table 3.2. *Number of Spatial Modes when r = 5*

Highest Power of r	j													Total Inflow States
	0	1	2	3	4	5	6	7	8	9	10	11	12	
5	3	3	2	2	1	1								21

The selection of the j value dictates the expansion range for the Fourier series. Each increment of the j adds a new pair of sine and cosine states. (e.g. $a_j^r \cos(r\psi) + b_j^r \sin(r\psi)$). The values written in the table is the number of spatial variation states corresponding the highest values of r.

The collective number of the states can be computed as:

Table 3.3. *Total Number of States When r = 5 and j =5*

Value of j	Non-Harmonic State	Cosine State	Sine State
0	3	-	-
1	-	3	3
2	-	2	2
3	-	2	2
4	-	1	1
5	-	1	1

Note that the number of states is determined from the summation (Eq. *(2.36)*):

$$w(\bar{r},\psi,\bar{t}) = \sum_{r=0}^{\infty}\sum_{j=r+1,r+3,\ldots}^{\infty} \Psi_j^r(\bar{r})\left[a_j^r(\bar{t})\cos(r\psi) + b_j^r(\bar{t})\sin(r\psi)\right]$$

Total number of states for r = 5 is given in Table *3.3* is as follows:

$$3+3+3+2+2+2+2+1+1+1+1=21 \tag{3.1}$$

The inflow equation for 21 – state becomes:

$$for\ t = \bar{t}, \text{ where } \bar{t} \text{ is non-dimensional time} \tag{3.2}$$

$$\begin{aligned} w(\bar{r},\psi,\bar{t}) = \quad & \Psi_1^0(\bar{r})a_1^0(\bar{t}) + \Psi_3^0(\bar{r})a_3^0(\bar{t}) + \Psi_5^0(\bar{r})a_5^0(\bar{t}) \\ & + \Psi_2^1(\bar{r})[a_2^1(\bar{t})\cos(1\psi) + b_2^1(\bar{t})\sin(1\psi)] \\ & + \Psi_4^1(\bar{r})[a_4^1(\bar{t})\cos(1\psi) + b_4^1(\bar{t})\sin(1\psi)] \\ & + \Psi_6^1(\bar{r})[a_6^1(\bar{t})\cos(1\psi) + b_6^1(\bar{t})\sin(1\psi)] \\ & + \Psi_3^2(\bar{r})[a_3^2(\bar{t})\cos(2\psi) + b_3^2(\bar{t})\sin(2\psi)] \\ & + \Psi_5^2(\bar{r})[a_5^2(\bar{t})\cos(2\psi) + b_5^2(\bar{t})\sin(2\psi)] \\ & + \Psi_4^3(\bar{r})[a_4^3(\bar{t})\cos(3\psi) + b_4^3(\bar{t})\sin(3\psi)] \\ & + \Psi_6^3(\bar{r})[a_6^3(\bar{t})\cos(3\psi) + b_6^3(\bar{t})\sin(3\psi)] \\ & + \Psi_5^4(\bar{r})[a_5^4(\bar{t})\cos(4\psi) + b_5^4(\bar{t})\sin(4\psi)] \\ & + \Psi_6^5(\bar{r})[a_6^5(\bar{t})\cos(5\psi) + b_6^5(\bar{t})\sin(5\psi)] \end{aligned}$$

Table 3.4. *State list when r=5 and j=5*

Radial Distribution Function $\Psi_j^r(\bar{r})$	Cosine Coefficients $a_j^r \cos(r\psi)$	Sine Coefficients b_j^r
$\Psi_1^0(\bar{r})$	$a_1^0(\bar{t})\cos(0\psi)$	$b_1^0(\bar{t})\sin(0\psi)$
$\Psi_3^0(\bar{r})$	$a_3^0(\bar{t})\cos(0\psi)$	$b_3^0(\bar{t})\sin(0\psi)$
$\Psi_5^0(\bar{r})$	$a_5^0(\bar{t})\cos(0\psi)$	$b_5^{0(\bar{t})}\sin(0\psi)$
$\Psi_2^1(\bar{r})$	$a_2^1(\bar{t})\cos(1\psi)$	$b_2^{1(\bar{t})}\sin(1\psi)$
$\Psi_4^1(\bar{r})$	$a_4^1(\bar{t})\cos(1\psi)$	$b_4^1(\bar{t})\sin(1\psi)$
$\Psi_6^1(\bar{r})$	$a_6^1(\bar{t})\cos(1\psi)$	$b_6^1(\bar{t})\sin(1\psi)$
$\Psi_3^2(\bar{r})$	$a_3^2(\bar{t})\cos(2\psi)$	$b_3^2(\bar{t})\sin(2\psi)$
$\Psi_5^2(\bar{r})$	$a_5^2(\bar{t})\cos(2\psi)$	$b_5^2(\bar{t})\sin(2\psi)$
$\Psi_4^3(\bar{r})$	$a_4^3(\bar{t})\cos(3\psi)$	$b_4^3(\bar{t})\sin(3\psi)$
$\Psi_6^3(\bar{r})$	$a_6^3(\bar{t})\cos(3\psi)$	$b_6^{3(\bar{t})}\sin(3\psi)$
$\Psi_5^4(\bar{r})$	$a_5^4(\bar{t})\cos(4\psi)$	$b_5^{4(\bar{t})}\sin(4\psi)$
$\Psi_6^5(\bar{r})$	$a_6^5(\bar{t})\cos(5\psi)$	$b_6^5(\bar{t})\sin(5\psi)$

Note that in *Table 3.4* total number of states is 24. However, for the 0th harmonics, $\sin(0) = 0$. Thus, the states b_1^0, b_3^0 and b_5^0 disappears from the equation. Also note that the $\cos(0\psi) = 1$, which results in the non-harmonic inflow states a_1^0, a_3^0 and a_5^0 that when combined with the radial distribution functions, $\Psi_1^0(\bar{r}), \Psi_3^0(\bar{r})$ and $\Psi_5^0(\bar{r})$ respectively, give the mean inflow on the rotor disc.

Throughout the Chapter 2, the state vectors for sine and cosine terms are decoupled. In addition, the matrix form of the theory is given as two separate equations in Eq.*(2.73)* and *(2.74)* for sine and cosine states. Therefore, both equations require to be constructed separately. (e.g. $\left[L_{jn}^{rm}\right]^{(c)}$ and $\left[L_{jn}^{rm}\right]^{(s)}$)

3.2.2. Apparent Mass Matrix [M]

In order to construct M matrix of a 21–State Peters–He inflow theory, the state vectors $\{a_j^r\}$ and $\{b_j^r\}$ are written separately.

Cosine States:

$$\{a_j^r\} = \begin{Bmatrix} a_1^0 \\ a_3^0 \\ a_5^0 \\ a_2^1 \\ a_4^1 \\ a_6^1 \\ a_3^2 \\ a_5^2 \\ a_4^3 \\ a_6^3 \\ a_5^4 \\ a_6^5 \end{Bmatrix} \tag{3.3}$$

Sine States:

$$\{b_j^r\} = \begin{Bmatrix} b_2^1 \\ b_4^1 \\ b_6^1 \\ b_3^2 \\ b_5^2 \\ b_4^3 \\ b_6^3 \\ b_5^4 \\ b_6^5 \end{Bmatrix} \tag{3.4}$$

Elements of $[M]^{(c)}$ and $[M]^{(s)}$ the elements given in Eq.*(2.53)* needs to be computed.

$$M_{jn}^{rm} = K_{jn}^{rm}\delta_{jn}\delta_{rm} = K_n^m = \frac{2}{\pi} H_n^m \qquad (2.53)$$

Since the terms δ_{rm} and δ_{jn} make matrix M is a purely diagonal one, there is no need to compute off – diagonal elements. Therefore, using state vectors given in Eq. *(3.3)* and *(3.4)* following table can be generated.

Table 3.5. *Elements of Cosine States Apparent Mass Matrix*

K_1^0	0	0	0	0	0	0	0	0	0	0	0
0	K_3^0	0	0	0	0	0	0	0	0	0	0
0	0	K_5^0	0	0	0	0	0	0	0	0	0
0	0	0	K_2^1	0	0	0	0	0	0	0	0
0	0	0	0	K_4^1	0	0	0	0	0	0	0
0	0	0	0	0	K_6^1	0	0	0	0	0	0
0	0	0	0	0	0	K_3^2	0	0	0	0	0
0	0	0	0	0	0	0	K_5^2	0	0	0	0
0	0	0	0	0	0	0	0	K_4^3	0	0	0
0	0	0	0	0	0	0	0	0	K_6^3	0	0
0	0	0	0	0	0	0	0	0	0	K_5^4	0
0	0	0	0	0	0	0	0	0	0	0	K_6^5

Using Eq. *(2.53)*, values of the above matrix are calculated as follows:

$$[M]^{(c)} = \qquad (3.5)$$

$$\begin{bmatrix}
0.6366 & 0 & 0 & 0 & 0 & 0 & 0 & 0 & 0 & 0 & 0 & 0 \\
0 & 0.2829 & 0 & 0 & 0 & 0 & 0 & 0 & 0 & 0 & 0 & 0 \\
0 & 0 & 0.1811 & 0 & 0 & 0 & 0 & 0 & 0 & 0 & 0 & 0 \\
0 & 0 & 0 & 0.4244 & 0 & 0 & 0 & 0 & 0 & 0 & 0 & 0 \\
0 & 0 & 0 & 0 & 0.2264 & 0 & 0 & 0 & 0 & 0 & 0 & 0 \\
0 & 0 & 0 & 0 & 0 & 0.1552 & 0 & 0 & 0 & 0 & 0 & 0 \\
0 & 0 & 0 & 0 & 0 & 0 & 0.3395 & 0 & 0 & 0 & 0 & 0 \\
0 & 0 & 0 & 0 & 0 & 0 & 0 & 0.1940 & 0 & 0 & 0 & 0 \\
0 & 0 & 0 & 0 & 0 & 0 & 0 & 0 & 0.2910 & 0 & 0 & 0 \\
0 & 0 & 0 & 0 & 0 & 0 & 0 & 0 & 0 & 0.1725 & 0 & 0 \\
0 & 0 & 0 & 0 & 0 & 0 & 0 & 0 & 0 & 0 & 0.2587 & 0 \\
0 & 0 & 0 & 0 & 0 & 0 & 0 & 0 & 0 & 0 & 0 & 0.2352
\end{bmatrix}$$

In order to write apparent mass matrix for the sine states, same procedure is applied.

Table 3.6. *Elements of Cosine States Apparent Mass Matrix*

K_2^1	0	0	0	0	0	0	0	0
0	K_4^1	0	0	0	0	0	0	0
0	0	K_6^1	0	0	0	0	0	0
0	0	0	K_3^2	0	0	0	0	0
0	0	0	0	K_5^2	0	0	0	0
0	0	0	0	0	K_4^3	0	0	0
0	0	0	0	0	0	K_6^3	0	0
0	0	0	0	0	0	0	K_5^4	0
0	0	0	0	0	0	0	0	K_6^5

Using Eq. *(2.53)*, values of the above matrix are calculated as follows:

$$[M]^{(s)} = \begin{bmatrix} 0.4244 & 0 & 0 & 0 & 0 & 0 & 0 & 0 & 0 \\ 0 & 0.2264 & 0 & 0 & 0 & 0 & 0 & 0 & 0 \\ 0 & 0 & 0.1552 & 0 & 0 & 0 & 0 & 0 & 0 \\ 0 & 0 & 0 & 0.3395 & 0 & 0 & 0 & 0 & 0 \\ 0 & 0 & 0 & 0 & 0.1940 & 0 & 0 & 0 & 0 \\ 0 & 0 & 0 & 0 & 0 & 0.2910 & 0 & 0 & 0 \\ 0 & 0 & 0 & 0 & 0 & 0 & 0.1725 & 0 & 0 \\ 0 & 0 & 0 & 0 & 0 & 0 & 0 & 0.2587 & 0 \\ 0 & 0 & 0 & 0 & 0 & 0 & 0 & 0 & 0.2352 \end{bmatrix} \tag{3.6}$$

Note that the sine states apparent mass matrix $[M]^{(s)}$ is a submatrix of the matrix $[M]^{(c)}$. The rows and columns corresponding to $\cos(0\psi)$ multiplying states a_1^0, a_3^0 and a_5^0 are truncated in sine states mass matrix. The reason for this truncation is that the counterparts of a_1^0, a_3^0 and a_5^0 states, namely b_1^0, b_3^0 and b_5^0, are removed from the inflow equation. (see *Table 3.4*)

3.2.3. Gain Matrices $[L]^{(c)}$ and $[L]^{(s)}$

The calculation of the elements of $[L]^{(c)}$ and $[L]^{(s)}$ matrices are given in Eq. *(2.75)*, *(2.76)* and *(2.77)* as:

$$\left[L_{jn}^{0m}\right]^{(c)} = X^m\left[\Gamma_{jn}^{0m}\right] \qquad (2.75)$$

$$\left[L_{jn}^{rm}\right]^{(c)} = \left[X^{|m-r|} + (-1)^{\ell} X^{|m+r|}\right]\left[\Gamma_{jn}^{rm}\right] \qquad (2.76)$$

$$\left[L_{jn}^{rm}\right]^{(s)} = \left[X^{|m-r|} - (-1)^{\ell} X^{|m+r|}\right]\left[\Gamma_{jn}^{rm}\right] \qquad (2.77)$$

where $\left[\Gamma_{jn}^{rm}\right]$ is given in Eq. *(2.78)*,*(2.79)* and *(2.80)*. It is important to notice that the elements $\left[L_{jn}^{rm}\right]$ are dependent on skew angle.

Let us rewrite Eq. *(2.78)*,*(2.79)* and *(2.80)* in the following form:

$$\left[L_{jn}^{0m}\right]^{(c)} = \theta^{(0c)}(\chi)\left[\Gamma_{jn}^{0m}\right], \text{ where } \theta^{(0c)}(\chi) = X^m \qquad (3.7)$$

$$\left[L_{jn}^{rm}\right]^{(c)} = \theta^{(c)}(\chi)\left[\Gamma_{jn}^{rm}\right], \text{ where } \theta^{(c)}(\chi) = \left[X^{|m-r|} + (-1)^{\ell} X^{|m+r|}\right] \qquad (3.8)$$

$$\left[L_{jn}^{rm}\right]^{(s)} = \theta^{(s)}(\chi)\left[\Gamma_{jn}^{rm}\right], \text{ where } \theta^{(s)}(\chi) = \left[X^{|m-r|} - (-1)^{\ell} X^{|m+r|}\right] \qquad (3.9)$$

where,

$X = \tan\left(\frac{\chi}{2}\right)$ and $\ell = \min(r, m)$

Unlike the apparent mass matrix, the $\left[L_{jn}^{rm}\right]^{(c)}$ and $\left[L_{jn}^{rm}\right]^{(s)}$ matrices are not diagonal, and thus there are four variables, namely r, m, j, n, to construct L matrices. The determination of the subscripts and superscripts are done in the following manner.

Table 3.7. *Subscripts and Superscripts of Cosine States L matrix elements*

States	$\boldsymbol{a_1^0}$	$\boldsymbol{a_3^0}$	$\boldsymbol{a_5^0}$	$\boldsymbol{a_2^1}$	$\boldsymbol{a_4^1}$	$\boldsymbol{a_6^1}$	$\boldsymbol{a_3^2}$	$\boldsymbol{a_5^2}$	$\boldsymbol{a_4^3}$	$\boldsymbol{a_6^3}$	$\boldsymbol{a_5^4}$	$\boldsymbol{a_6^5}$
$\boldsymbol{a_1^0}$	L_{11}^{00}	L_{13}^{00}	L_{15}^{00}	L_{12}^{01}	L_{14}^{01}	L_{16}^{01}	L_{13}^{02}	L_{15}^{02}	L_{14}^{03}	L_{16}^{03}	L_{15}^{04}	L_{16}^{05}
$\boldsymbol{a_3^0}$	L_{31}^{00}	L_{33}^{00}	L_{35}^{00}	L_{32}^{01}	L_{34}^{01}	L_{36}^{01}	L_{33}^{02}	L_{35}^{02}	L_{34}^{03}	L_{36}^{03}	L_{35}^{04}	L_{36}^{05}
$\boldsymbol{a_5^0}$	L_{51}^{00}	L_{53}^{00}	L_{55}^{00}	L_{52}^{01}	L_{54}^{01}	L_{56}^{01}	L_{53}^{02}	L_{55}^{02}	L_{54}^{03}	L_{56}^{03}	L_{55}^{04}	L_{56}^{05}
$\boldsymbol{a_2^1}$	L_{21}^{10}	L_{23}^{10}	L_{25}^{10}	L_{22}^{11}	L_{24}^{11}	L_{26}^{11}	L_{23}^{12}	L_{25}^{12}	L_{24}^{13}	L_{26}^{13}	L_{25}^{14}	L_{26}^{15}
$\boldsymbol{a_4^1}$	L_{41}^{10}	L_{43}^{10}	L_{45}^{10}	L_{42}^{11}	L_{44}^{11}	L_{46}^{11}	L_{43}^{12}	L_{45}^{12}	L_{44}^{13}	L_{46}^{13}	L_{45}^{14}	L_{46}^{15}
$\boldsymbol{a_6^1}$	L_{61}^{10}	L_{63}^{10}	L_{65}^{10}	L_{62}^{11}	L_{64}^{11}	L_{66}^{11}	L_{63}^{12}	L_{65}^{12}	L_{64}^{13}	L_{66}^{13}	L_{65}^{14}	L_{66}^{15}
$\boldsymbol{a_3^2}$	L_{31}^{20}	L_{33}^{20}	L_{35}^{20}	L_{32}^{21}	L_{34}^{21}	L_{36}^{21}	L_{33}^{22}	L_{35}^{22}	L_{34}^{23}	L_{36}^{23}	L_{35}^{24}	L_{36}^{25}
$\boldsymbol{a_5^2}$	L_{51}^{20}	L_{53}^{20}	L_{55}^{20}	L_{52}^{21}	L_{54}^{21}	L_{56}^{21}	L_{53}^{22}	L_{55}^{22}	L_{54}^{23}	L_{56}^{23}	L_{55}^{24}	L_{56}^{25}
$\boldsymbol{a_4^3}$	L_{41}^{30}	L_{43}^{30}	L_{45}^{30}	L_{42}^{31}	L_{44}^{31}	L_{46}^{31}	L_{43}^{32}	L_{45}^{32}	L_{44}^{33}	L_{46}^{33}	L_{45}^{34}	L_{46}^{35}
$\boldsymbol{a_6^3}$	L_{61}^{30}	L_{63}^{30}	L_{65}^{30}	L_{62}^{31}	L_{64}^{31}	L_{66}^{31}	L_{63}^{32}	L_{65}^{32}	L_{64}^{33}	L_{66}^{33}	L_{65}^{34}	L_{66}^{35}
$\boldsymbol{a_5^4}$	L_{51}^{40}	L_{53}^{40}	L_{55}^{40}	L_{52}^{41}	L_{54}^{41}	L_{56}^{41}	L_{53}^{42}	L_{55}^{42}	L_{54}^{43}	L_{56}^{43}	L_{55}^{44}	L_{56}^{45}
$\boldsymbol{a_6^5}$	L_{61}^{50}	L_{63}^{50}	L_{65}^{50}	L_{62}^{51}	L_{64}^{51}	L_{66}^{51}	L_{63}^{52}	L_{65}^{52}	L_{64}^{53}	L_{66}^{53}	L_{65}^{54}	L_{66}^{55}

In Table *3.7*, the states at first column drive the r and j values of L_{jn}^{rm} in their row. Similarly, the states in first row drive m and n values of L_{jn}^{rm} in their column.

As seen in Eq. *(2.75), (2.76)* and *(2.77)* elements can be divided into two parts. The part that is independent of the skew angle can directly be computed using the definition of Γ function given in Eq. *(2.78), (2.79)* and *(2.80)*.

$$L_{jn}^{rm} = \theta_{jn}^{rm}(\chi)\Gamma_{jn}^{rm} \tag{3.10}$$

The Γ_{jn}^{rm} part of the L_{jn}^{rm} for r, m, j, n given in Table *3.7* is calculated as:

Table 3.8. *Column (1-6) of Cosine States Γ Matrix*

	Γ_{j1}^{r0}	Γ_{j3}^{r0}	Γ_{j5}^{r0}	Γ_{j2}^{r1}	Γ_{j4}^{r1}	Γ_{j6}^{r1}
Γ_{1n}^{0m}	0.7500	0.1909	-0.0299	-0.4967	0.0000	0.0000
Γ_{3n}^{0m}	0.1909	0.6563	0.2057	-0.4878	-0.4978	0.0000
Γ_{5n}^{0m}	-0.0299	0.2057	0.6445	0.0000	-0.4964	-0.4988
Γ_{2n}^{1m}	0.4967	0.4878	0.0000	0.6250	0.1914	-0.0333
Γ_{4n}^{1m}	0.0000	0.4978	0.4964	0.1914	0.6328	0.2041
Γ_{6n}^{1m}	0.0000	0.0000	0.4988	-0.0333	0.2041	0.6348
Γ_{3n}^{2m}	0.1743	0.5991	0.1877	0.4453	0.4545	0.0000
Γ_{5n}^{2m}	-0.0289	0.1987	0.6227	0.0000	0.4796	0.4819
Γ_{4n}^{3m}	0.0000	0.4391	0.4378	0.1688	0.5581	0.1800
Γ_{6n}^{3m}	0.0000	0.0000	0.4732	-0.0316	0.1936	0.6022
Γ_{5n}^{4m}	-0.0250	0.1721	0.5393	0.0000	0.4153	0.4173
Γ_{6n}^{5m}	0.0000	0.0000	0.4052	-0.0271	0.1658	0.5157

Table 3.9. *Column (7-12) of Cosine States Γ Matrix*

	Γ_{j3}^{r2}	Γ_{j5}^{r2}	Γ_{j4}^{r3}	Γ_{j6}^{r3}	Γ_{j5}^{r4}	Γ_{j6}^{r5}
Γ_{1n}^{0m}	0.1743	-0.0289	0.0000	0.0000	-0.025	0.0000
Γ_{3n}^{0m}	0.5991	0.1987	-0.4391	0.0000	0.1721	0.0000
Γ_{5n}^{0m}	0.1877	0.6227	-0.4378	-0.4732	0.5393	-0.4052
Γ_{2n}^{1m}	-0.4453	0.0000	0.1688	-0.0316	0.0000	-0.0271
Γ_{4n}^{1m}	-0.4545	-0.4796	0.5581	0.1936	-0.4153	0.1658
Γ_{6n}^{1m}	0.0000	-0.4819	0.1800	0.6022	-0.4173	0.5157
Γ_{3n}^{2m}	0.5469	0.1814	-0.4008	0.0000	0.1571	0.0000
Γ_{5n}^{2m}	0.1814	0.6016	-0.4230	-0.4572	0.5210	-0.3915
Γ_{4n}^{3m}	0.4008	0.4230	0.4922	0.1708	-0.3663	0.1462
Γ_{6n}^{3m}	0.0000	0.4572	0.1708	0.5713	-0.3959	0.4892
Γ_{5n}^{4m}	0.1571	0.5210	0.3663	0.3959	0.4512	-0.3390
Γ_{6n}^{5m}	0.0000	0.3915	0.1462	0.4892	0.3390	0.4189

To obtain the gain matrix L for cosine states, the values of $[\theta_{jn}^{rm(c)}(\chi)]$ needs to be computed besides the $\left[\Gamma_{jn}^{\mathrm{rm}}\right]$ matrix. Since function $[\theta_{jn}^{rm(c)}(\chi)]$ is a function of skew angle, χ an arbitrary selection for χ is made such that:

$$\chi = 0.2\ radians \tag{3.11}$$

For the skew angle selected in Eq.*(3.11)* the $\left[\theta_{jn}^{rm}(\chi)\right]$ is calculated as follow:

Table 3.10. *Column (1-6) of Cosine States θ Matrix*

	θ_{j1}^{r0}	θ_{j3}^{r0}	θ_{j5}^{r0}	θ_{j2}^{r1}	θ_{j4}^{r1}	θ_{j6}^{r1}
θ_{1n}^{0m}	1.0000	1.0000	1.0000	0.2000	0.2000	0.2000
θ_{3n}^{0m}	1.0000	1.0000	1.0000	0.2000	0.2000	0.2000
θ_{5n}^{0m}	1.0000	1.0000	1.0000	0.2000	0.2000	0.2000
θ_{2n}^{1m}	0.4000	0.4000	0.4000	0.9600	0.9600	0.9600
θ_{4n}^{1m}	0.4000	0.4000	0.4000	0.9600	0.9600	0.9600
θ_{6n}^{1m}	0.4000	0.4000	0.4000	0.9600	0.9600	0.9600
θ_{3n}^{2m}	0.0800	0.0800	0.0800	0.1920	0.1920	0.1920
θ_{5n}^{2m}	0.0800	0.0800	0.0800	0.1920	0.1920	0.1920
θ_{4n}^{3m}	0.0160	0.0160	0.0160	0.0384	0.0384	0.0384
θ_{6n}^{3m}	0.0160	0.0160	0.0160	0.0384	0.0384	0.0384
θ_{5n}^{4m}	0.0032	0.0032	0.0032	0.0077	0.0077	0.0077
θ_{6n}^{5m}	0.0006	0.0006	0.0006	0.0015	0.0015	0.0015

Table 3.11. *Column (7-12) of Cosine States θ Matrix*

	θ_{j3}^{r2}	θ_{j5}^{r2}	θ_{j4}^{r3}	θ_{j6}^{r3}	θ_{j5}^{r4}	θ_{j6}^{r5}
θ_{1n}^{0m}	0.0400	0.0400	0.0080	0.0080	0.0016	0.0003
θ_{3n}^{0m}	0.0400	0.0400	0.0080	0.0080	0.0016	0.0003
θ_{5n}^{0m}	0.0400	0.0400	0.0080	0.0080	0.0016	0.0003
θ_{2n}^{1m}	0.1920	0.1920	0.0384	0.0384	0.0077	0.0015
θ_{4n}^{1m}	0.1920	0.1920	0.0384	0.0384	0.0077	0.0015
θ_{6n}^{1m}	0.1920	0.1920	0.0384	0.0384	0.0077	0.0015
θ_{3n}^{2m}	1.0016	1.0016	0.2003	0.2003	0.0401	0.0080
θ_{5n}^{2m}	1.0016	1.0016	0.2003	0.2003	0.0401	0.0080
θ_{4n}^{3m}	0.2003	0.2003	0.9999	0.9999	0.2000	0.0400
θ_{6n}^{3m}	0.2003	0.2003	0.9999	0.9999	0.2000	0.0400
θ_{5n}^{4m}	0.0401	0.0401	0.2000	0.2000	1.0000	0.2000
θ_{6n}^{5m}	0.0080	0.0080	0.0400	0.0400	0.2000	1.0000

Finally, both functions to construct $\left[L_{jn}^{rm}\right]^{(c)}$, $\theta_{jn}^{rm}(\chi)$ and Γ_{jn}^{rm}, are ready. Note that the multiplication Γ_{jn}^{rm} and $\theta_{jn}^{rm}(\chi)$ are not a matrix multiplication but an element-wise multiplication such that:

$$\left[L_{jn}^{rm}\right]^{(c)} = [\theta_{jn}^{rm}(\chi)] \bullet [\Gamma_{jn}^{rm}] \tag{3.12}$$

where operator "•" indicates the element – wise multiplication of matrices.

Exact same procedure is applied for the $\left[L_{jn}^{rm}\right]^{(s)}$ matrix for the r, m, j, n combinations given below.

Table 3.12. *Subscripts and Superscripts of Sine States L matrix elements*

States	$\boldsymbol{b_2^1}$	$\boldsymbol{b_4^1}$	$\boldsymbol{b_6^1}$	$\boldsymbol{b_3^2}$	$\boldsymbol{b_5^2}$	$\boldsymbol{b_4^3}$	$\boldsymbol{b_6^3}$	$\boldsymbol{b_5^4}$	$\boldsymbol{b_6^5}$
$\boldsymbol{b_2^1}$	L_{22}^{11}	L_{24}^{11}	L_{26}^{11}	L_{23}^{12}	L_{25}^{12}	L_{24}^{13}	L_{26}^{13}	L_{25}^{14}	L_{26}^{15}
$\boldsymbol{b_4^1}$	L_{42}^{11}	L_{44}^{11}	L_{46}^{11}	L_{43}^{12}	L_{45}^{12}	L_{44}^{13}	L_{46}^{13}	L_{45}^{14}	L_{46}^{15}
$\boldsymbol{b_6^1}$	L_{62}^{11}	L_{64}^{11}	L_{66}^{11}	L_{63}^{12}	L_{65}^{12}	L_{64}^{13}	L_{66}^{13}	L_{65}^{14}	L_{66}^{15}
$\boldsymbol{b_3^2}$	L_{32}^{21}	L_{34}^{21}	L_{36}^{21}	L_{33}^{22}	L_{35}^{22}	L_{34}^{23}	L_{36}^{23}	L_{35}^{24}	L_{36}^{25}
$\boldsymbol{b_5^2}$	L_{52}^{21}	L_{54}^{21}	L_{56}^{21}	L_{53}^{22}	L_{55}^{22}	L_{54}^{23}	L_{56}^{23}	L_{55}^{24}	L_{56}^{25}
$\boldsymbol{b_4^3}$	L_{42}^{31}	L_{44}^{31}	L_{46}^{31}	L_{43}^{32}	L_{45}^{32}	L_{44}^{33}	L_{46}^{33}	L_{45}^{34}	L_{46}^{35}
$\boldsymbol{b_6^3}$	L_{62}^{31}	L_{64}^{31}	L_{66}^{31}	L_{63}^{32}	L_{65}^{32}	L_{64}^{33}	L_{66}^{33}	L_{65}^{34}	L_{66}^{35}
$\boldsymbol{b_5^4}$	L_{52}^{41}	L_{54}^{41}	L_{56}^{41}	L_{53}^{42}	L_{55}^{42}	L_{54}^{43}	L_{56}^{43}	L_{55}^{44}	L_{56}^{45}
$\boldsymbol{b_6^5}$	L_{62}^{51}	L_{64}^{51}	L_{66}^{51}	L_{63}^{52}	L_{65}^{52}	L_{64}^{53}	L_{66}^{53}	L_{65}^{54}	L_{66}^{55}

Table 3.13. *Column (1-5) of Sine States Γ Matrix*

	Γ_{j2}^{r1}	Γ_{j4}^{r1}	Γ_{j6}^{r1}	Γ_{j3}^{r2}	Γ_{j5}^{r2}
Γ_{2n}^{1m}	0.6250	0.1914	-0.0333	-0.4453	0.0000
Γ_{4n}^{1m}	0.1914	0.6328	0.2041	-0.4545	-0.4796
Γ_{6n}^{1m}	-0.0333	0.2041	0.6348	0.0000	-0.4819
Γ_{3n}^{2m}	0.4453	0.4545	0.0000	0.5469	0.1814
Γ_{5n}^{2m}	0.0000	0.4796	0.4819	0.1814	0.6016
Γ_{4n}^{3m}	0.1688	0.5581	0.1800	0.4008	0.4230
Γ_{6n}^{3m}	-0.0316	0.1936	0.6022	0.0000	0.4572
Γ_{5n}^{4m}	0.0000	0.4153	0.4173	0.1571	0.5210
Γ_{6n}^{5m}	-0.0271	0.1658	0.5157	0.0000	0.3915

Table 3.14. *Column (6-9) of Sine States Γ Matrix*

	Γ_{j4}^{r3}	Γ_{j6}^{r3}	Γ_{j5}^{r4}	Γ_{j6}^{r5}
Γ_{2n}^{1m}	0.1688	-0.0316	0.0000	-0.0271
Γ_{4n}^{1m}	0.5581	0.1936	-0.4153	0.1658
Γ_{6n}^{1m}	0.1800	0.6022	-0.4173	0.5157
Γ_{3n}^{2m}	-0.4008	0.0000	0.1571	0.0000
Γ_{5n}^{2m}	-0.4230	-0.4572	0.5210	-0.3915
Γ_{4n}^{3m}	0.4922	0.1708	-0.3663	0.1462
Γ_{6n}^{3m}	0.1708	0.5713	-0.3959	0.4892
Γ_{5n}^{4m}	0.3663	0.3959	0.4512	-0.3390
Γ_{6n}^{5m}	0.1462	0.4892	0.3390	0.4189

Table 3.15. *Column (1-5) of Sine States θ Matrix*

	θ_{j2}^{r1}	θ_{j4}^{r1}	θ_{j6}^{r1}	θ_{j3}^{r2}	θ_{j5}^{r2}
θ_{2n}^{1m}	1.0400	1.0400	1.0400	0.2080	0.2080
θ_{4n}^{1m}	1.0400	1.0400	1.0400	0.2080	0.2080
θ_{6n}^{1m}	1.0400	1.0400	1.0400	0.2080	0.2080
θ_{3n}^{2m}	0.2080	0.2080	0.2080	0.9984	0.9984
θ_{5n}^{2m}	0.2080	0.2080	0.2080	0.9984	0.9984
θ_{4n}^{3m}	0.0416	0.0416	0.0416	0.1997	0.1997
θ_{6n}^{3m}	0.0416	0.0416	0.0416	0.1997	0.1997
θ_{5n}^{4m}	0.0083	0.0083	0.0083	0.0399	0.0399
θ_{6n}^{5m}	0.0017	0.0017	0.0017	0.0080	0.0080

Table 3.16. *Column (6-9) of Sine States θ Matrix*

	$\boldsymbol{\theta_{j4}^{r3}}$	$\boldsymbol{\theta_{j6}^{r3}}$	$\boldsymbol{\theta_{j5}^{r4}}$	$\boldsymbol{\theta_{j6}^{r5}}$
$\boldsymbol{\theta_{2n}^{1m}}$	0.0416	0.0416	0.0083	0.0017
$\boldsymbol{\theta_{4n}^{1m}}$	0.0416	0.0416	0.0083	0.0017
$\boldsymbol{\theta_{6n}^{1m}}$	0.0416	0.0416	0.0083	0.0017
$\boldsymbol{\theta_{3n}^{2m}}$	0.1997	0.1997	0.0399	0.0080
$\boldsymbol{\theta_{5n}^{2m}}$	0.1997	0.1997	0.0399	0.0080
$\boldsymbol{\theta_{4n}^{3m}}$	1.0001	1.0001	0.2000	0.0400
$\boldsymbol{\theta_{6n}^{3m}}$	1.0001	1.0001	0.2000	0.0400
$\boldsymbol{\theta_{5n}^{4m}}$	0.2000	0.2000	1.0000	0.2000
$\boldsymbol{\theta_{6n}^{5m}}$	0.0400	0.0400	0.2000	1.0000

Note that, one can compute L_{jn}^{rm} element without separating skew angle contribution and Γ function contribution. If such method is chosen, the computation of Gamma function becomes redundant. Because Gamma function only required to be computed initially, whereas θ is a function of skew angle, χ, it can be computed once and then use throughout the simulation. Separating θ and Γ functions is merely to increase calculation speed and avoid unnecessary computation of Γ functions.

3.2.4. Velocity [V] Matrix

In Eq. *(2.81)* and *(2.82)*, V_{total} and V_s is computed. The only unknown to compute λ_m is the inflow state a_1^0. The state is initialized to zero, and as the simulation progress replaced with the newly computed a_1^0 state. This yields a relation such that:

$$a_1^0 = a_1^0(\lambda_m) \tag{3.13}$$

$$\lambda_m = \lambda_m(a_1^0) \tag{3.14}$$

Therefore, there is an iterative relation between the inflow states and the mean inflow, which makes this a non-linear theory.

3.2.5. Final Equations

Finally, following equations for Peters – He inflow can be written;

$$\left[M^{(c)}\right]\{a_j^r\}^* + [V]^{(c)}\left[L^{(c)}\right]^{-1}\{a_j^r\} = \{\tau_j^{r\,(c)}\} \tag{3.15}$$

$$\left[M^{(s)}\right]\{b_j^r\}^* + [V]^{(s)}\left[L^{(s)}\right]^{-1}\{b_j^r\} = \{\tau_j^{r\,(s)}\} \tag{3.16}$$

Rearranging equations:

$$\left[M^{(c)}\right]\{a_j^r\}^* + [V]^{(c)}\left[\theta^{(c)}(\chi)\cdot\Gamma^{(c)}\right]^{-1}\{a_j^r\} = \{\tau_j^{r\,(c)}\} \tag{3.17}$$

$$\left[M^{(s)}\right]\{b_j^r\}^* + [V]^{(s)}\left[\theta^{(s)}(\chi)\cdot\Gamma^{(s)}\right]^{-1}\{b_j^r\} = \{\tau_j^{r\,(s)}\} \tag{3.18}$$

The harmonic and radial expansion for the inflow is selected by using Table 3.1. The apparent mass matrices $\left[\mathrm{M}^{(c)}\right]$ and $\left[\mathrm{M}^{(s)}\right]$ are computed in Table 3.5, Table 3.6, Eq.(3.5) and Eq. (3.6). The skew angle functions of L matrix, $\theta^{(c)}(\chi)$ and $\theta^{(s)}(\chi)$ are computed and given in Table 3.10, Table 3.11, Table 3.15 and Table 3.16 . The Γ functions of L matrix, $\Gamma^{(c)}$ and $\Gamma^{(s)}$ are computed and presented in Table 3.8, Table 3.9, Table 3.13 and Table *3.14*.

All inflow states are initialized to zero initially. Then, the state derivatives with respect to non-dimensional time are calculated. Integration of these derivatives yields to inflow states. It is important to note that the derivative is a non-dimensional time derivative where:

$$\bar{t} = \Omega t \text{ where } \Omega \text{ is the angular velocity of rotor in radians.} \tag{3.19}$$

Therefore, the Euler integration of that state a_j^r or b_j^r looks like as follows:

$$a_j^r = a_j^r + \left(a_j^r\right)^* \Delta\bar{t} \;\rightarrow\; a_j^r = a_j^r + \left(a_j^r\right)^* (\Omega\Delta t)\,, \tag{3.20}$$

$$b_j^r = b_j^r + \left(b_j^r\right)^* \Delta\bar{t} \rightarrow b_j^r = b_j^r + \left(b_j^r\right)^* (\Omega\Delta t)\,, \tag{3.21}$$

In above section, all matrices are calculated except the forcing vector $\{\tau_j^r\}$ for both sine and cosine states. The forcing vector is determined by the lift. One can implement any method to calculate lift and generate $\{\tau_j^r\}$. The inflow theory is essentially independent of the lift theory.

In Chapter 4, the isolated rotor model and generating forcing vector, $\{\tau_j^r\}$, is explained.

CHAPTER 4

ISOLATED ROTOR MODEL

4.1. Basic Rotor Dynamics

The helicopter rotor generates lift simply by pulling air from above, accelerating through the rotor disc and pushing air below. This simple mechanic is achieved by complex inflow dynamics mainly the rotation of the blades and partially by the forward velocity of the helicopter.

A control input given by the pilot that is shown in figure below as the $\theta_{bl.}$ This results in an angle of attack for the blade. In return a lift is generated on the blade. The geometric relations are shown in the figure below.

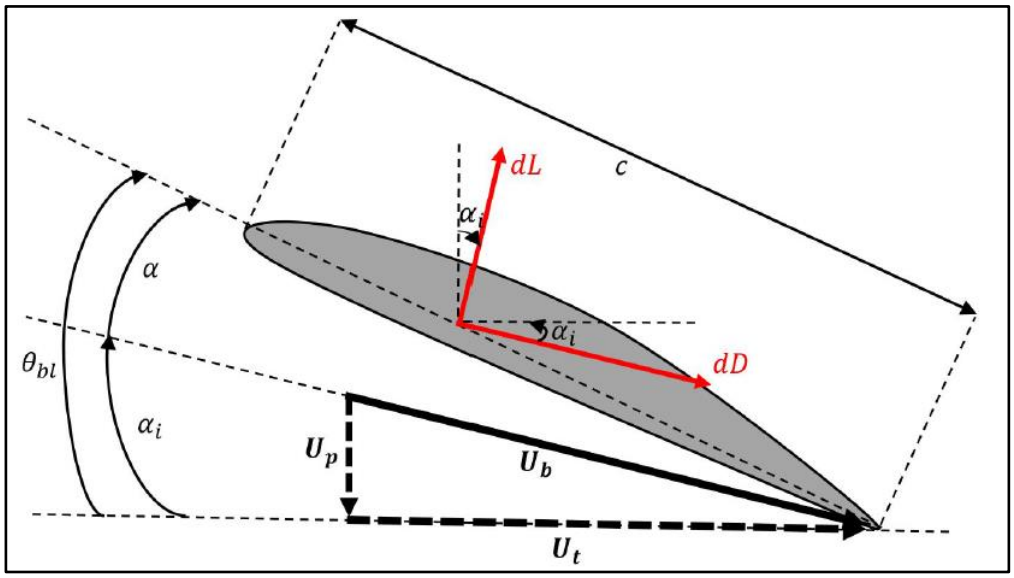

Figure 4.1. Pitch angle corresponding to control input, θ_{bl} [16]

This control input creates and apparent angle of attack with respect to the travel of the blade section due to rotation of rotor and motion of the aircraft.

The control input is the collective and cyclic inputs given in the following equation.

$$\theta_{blade} = \theta_{collective} + \theta_{LatCyc} * \cos(\psi) + \theta_{LonCyc} * sin(\psi) \tag{4.1}$$

In order to write infinitesimal lift dL and infinitesimal drag dD given in equations below, the effective angle of attack α_{eff} is required to be determined.

$$dL = \frac{1}{2} * \rho * V^2 * C_L(\alpha_{eff}, \mu) * c * dr \tag{4.2}$$

$$dD = \frac{1}{2} * \rho * V^2 * C_D(\alpha_{eff}, \mu) * c * dr \tag{4.3}$$

However, the α_{eff} itself depends on the inflow of the rotor. In addition, the inflow states are driven by the lift generated by the rotor which depends on the effective angle of attack in return where α_{eff} is given as:

$$\alpha_{eff} = \theta_{blade} - \text{atan}\left(\frac{U_p}{U_t}\right) \tag{4.4}$$

Where U_p is the perpendicular velocity on the blade element,

U_t is the tangential velocity on the blade element,

ρ is density,

V is total velocity on blade element,

C_L and C_D are lift and drag coefficients respectively,

c is chord,

dr is the infinitesimal element length.

4.2. Calculation of Section Velocities

The determination of lift of the blade is directly depends on the effective angle of attack seen by the infinitesimal blade. There are three main contributors to the perpendicular velocity.

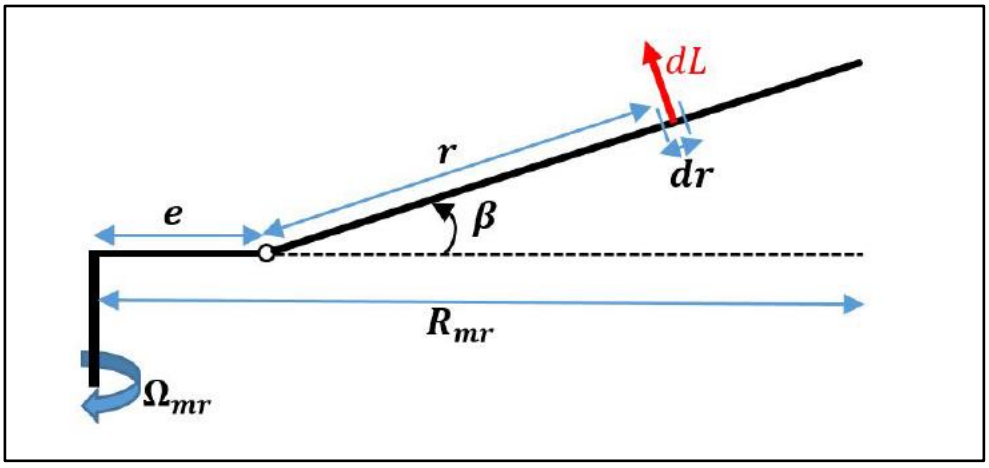

Figure 4.2. Blade length and angles [16]

Considering the figure above, the velocities at station "r" from the hinge is given in the Ref [16] for an articulated blade as below:

$$U_t = \Omega_{MR}(e + r) + u_b \sin(\psi) - v_b \cos(\psi) \tag{4.5}$$

$$U_p = -w_b + u_b\beta \cos(\psi) + v_b\beta \sin(\psi) + v_i + \dot{\beta}r + (e + r)(p\sin(\psi) - q\cos(\psi)) \tag{4.6}$$

Where,

u_b, v_b, w_b are translation velocities of the helicopter in body frame,

p, q are rotational velocities of the helicopter in body frame,

r is the distance from flapping hinge to blade element,

e is the distance from rotor hub to flapping hinge,

v_i is the induced inflow,

β is the flapping angle of the blade around flapping hinge.

In order to compute the forcing vector which depends on the lift of the blade, the blade element theory is used. The values tables of lift and drag coefficients C_L and C_D are given in the Appendix C along with the blade element figure.

It is important to note that "r" and "e" are structural parameters of the helicopter, and $u_b,\ v_b, w_b$ and p, q are states of the helicopter which are calculated by 6-DOF dynamic equations. This left with two important values for the calculation of effective angle of attack, which are β and v_i. These two values are solved simultaneously. The value of equation of motion for β can be written as [4][24][26][32][40]:

$$\sum_{q=0}^{Q}\left[\left(r_q * dL_q\right) + \left(dr * w^2 r_q^2\ m_b \beta\ \right] = I_{blade}\,\ddot{\beta}\right. \tag{4.7}$$

4.3. Rotor Model Procedure

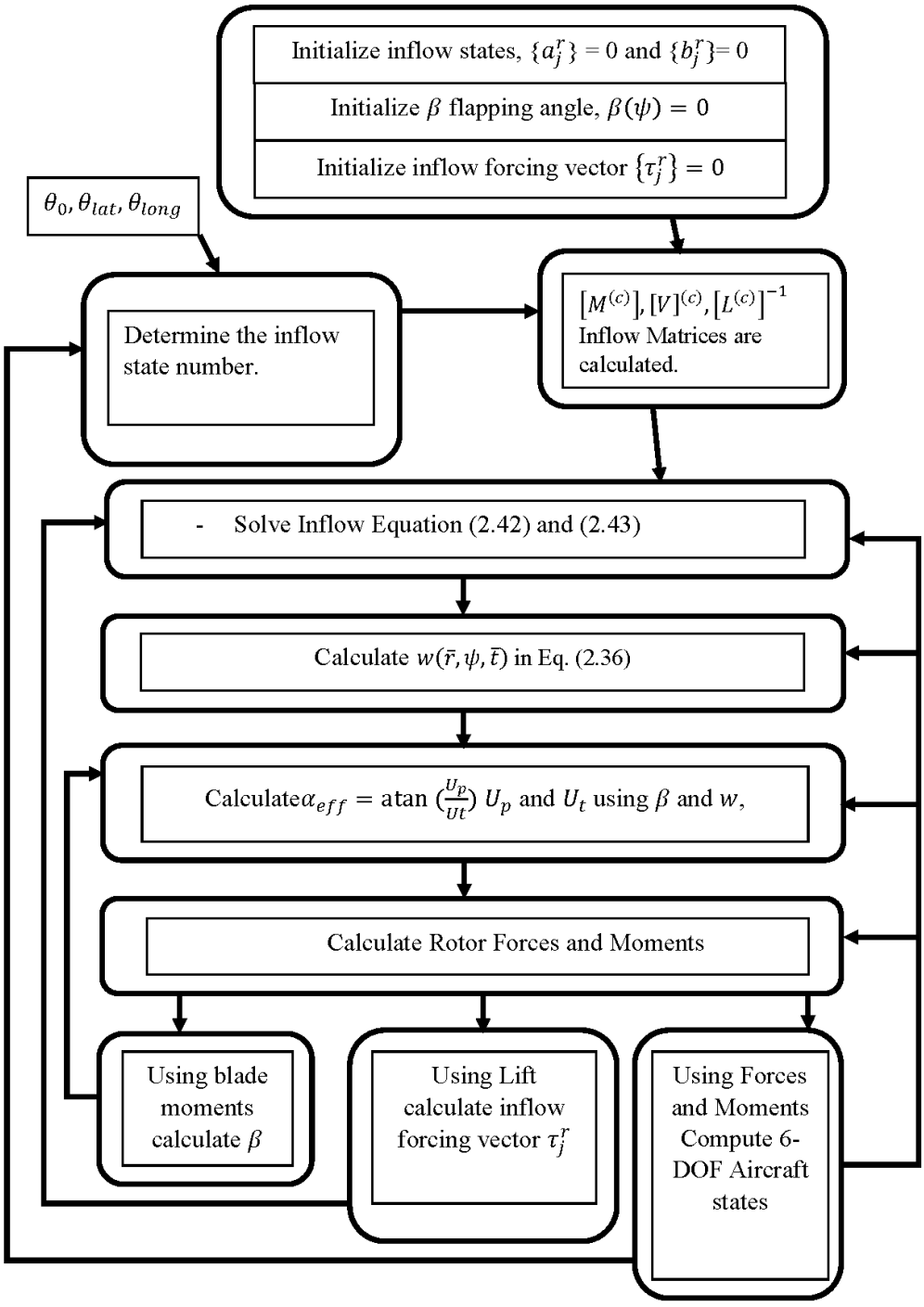

Figure 4.3. Rotor Model Flowchart

In above chart, the basic simulation steps are given for an isolated rotor model. In order to compute the inflow, only missing information is the forcing vector. The equations to compute forcing vector τ is given as follows:

$$\tau_j^0 = \frac{1}{(2\pi)} \sum_{q=1}^{Q} dL * \phi_j^r(\bar{r}) \tag{4.8}$$

$$\tau_j^{r(c)} = \frac{\cos(\psi_q)}{\pi} \sum_{q=1}^{Q} dL * \phi_j^r(\bar{r}) \tag{4.9}$$

$$\tau_j^{r(s)} = \frac{\sin(\psi_q)}{\pi} \sum_{q=1}^{Q} dL * \phi_j^r(\bar{r}) \tag{4.10}$$

Where r and j are the r and j value of the respective inflow states $\{a_j^r\}$ and $\{b_j^r\}$,

Q is the total number of blade elements on a blade,

q is the blade element number,

ψ_q is the azimuth angle of the blade in which the blade element resides.

In the inner-most iteration of the blade element calculations, the forcing vector is generated alongside with the infinitesimal lift dL.

Computation of these τ_j^r completes the Peters – He inflow theory.

4.4. Properties of Isolated Rotor Model

The rotor model used to investigate inflow throughout this thesis is the S-76 helicopter rotor with following parameters.

Table 4.1. *Parameters of S-76 Helicopter [41]*

Rotor Radius [m]	6.7056
Rotor Speed [rpm]	293
Hinge Offset	0.037
Solidity Ratio	0.0748
Airfoil	SC1095
Blade Number	4
Blade Twist	Figure 4.4

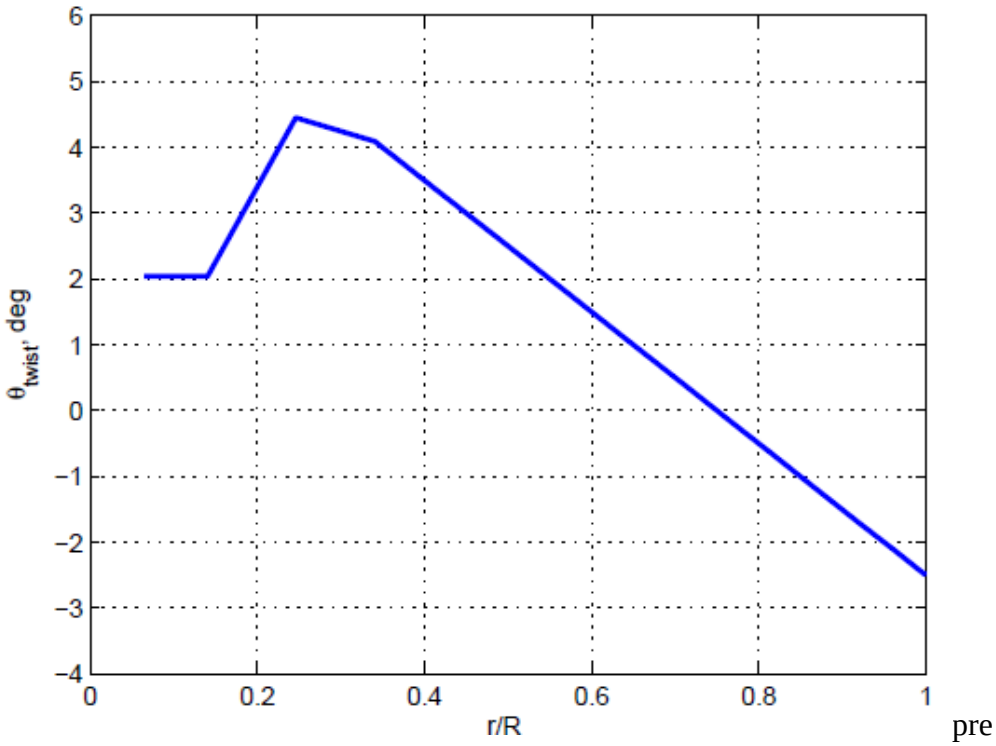

pre

Figure 4.4. Twist along the blade radius [14]

In the rotor model 16 virtual blade is used. Each blade is divided into 20 blade elements. Inflow values are obtained at these stations. An example of the obtained inflow distribution for various flight conditions are given in the following figure.

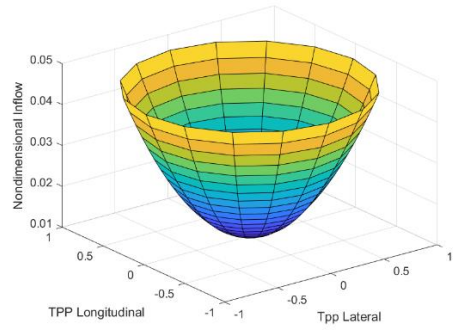

Flight Condition 1 : 6 state zero advance ratio at neutral controls

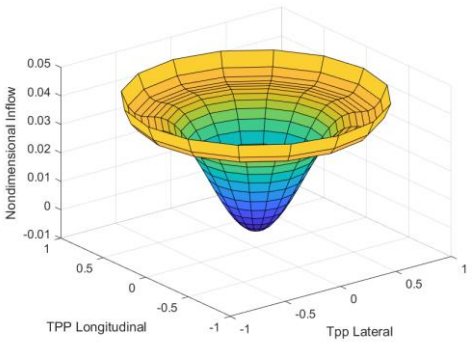

Flight Condition 2: 21 state zero advance ratio at neutral controls

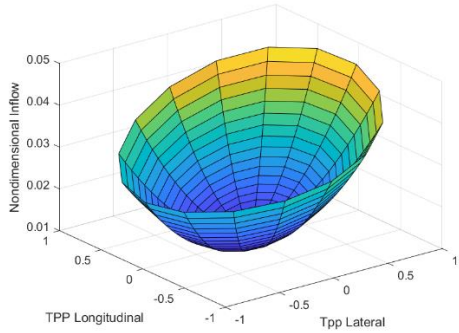

Flight Condition 3: 6 state 0.15 advance ratio at neutral controls

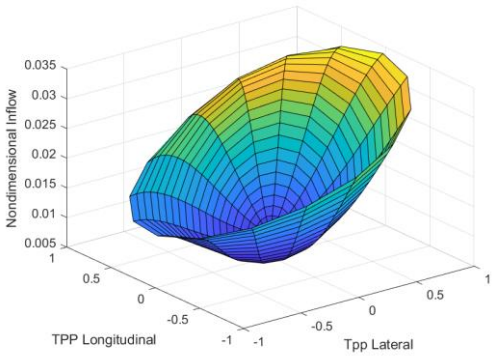

Flight Condition 4: 21 state 0.15 advance ratio at neutral controls

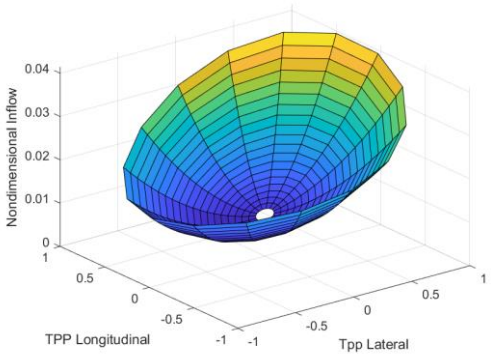

Flight Condition 5: 6 state 0.30 advance ratio at neutral controls

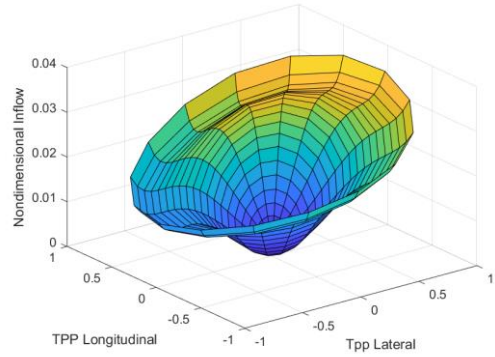

Flight Condition 6: 6 state 0.30 advance ratio at neutral controls

Figure 4.5. Example of inflow distributions

4.5. Error Calculation for Difference Analysis

In the following chapter, a rigorous investigation is made in order to understand the effects of state number to inflow distribution under different advance ratios and control combinations. Therefore, the following error procedure is used throughout Chapter 5 to quantify the difference between two inflow distribution.

Error is calculated by the following procedure:

• The inflow distribution with conventional 21 state Peters – He inflow model is selected as baseline inflow model and used for the calculation of mean inflow.

• For 16 virtual blades and 20 blade elements, total 320 sections inflows are calculated for each state-number inflow model.

• The inflow distribution difference is calculated extracting baseline distribution

model from varying state inflow distribution.

• An error matrix is obtained for 320 elements at each time step (100 Hz.).

• Then, using the following error equation, percentage error is calculated.

$$e_{time=t} = 100 * \left(\sum_{n}^{N} \sum_{q}^{Q} \left| \frac{\left(\lambda_n^q\right) - \lambda_{n_{baseline}}^q}{\lambda_{n_{baseline}}^q} \right| \right) * \frac{1}{N * Q} \tag{4.11}$$

Where n and q show the blade and blade element number respectively, for N blade and Q blade element on each blade.

CHAPTER 5

DYNAMIC INFLOW DISTRIBUTION SIMULATIONS

5.1. Introduction

In this chapter, the effects of advance ratio and control inputs to Peters – He inflow distribution are thoroughly investigated for 6, 10, 15 and 21 State Peters – He inflow models.

Throughout this chapter, it is assumed that the high-number-state model is better for the simulation fidelity [15][16][28][29]. Therefore, a 21 State inflow model is selected as the baseline inflow model. All other inflow models such as 6, 10, and 15 inflow distributions are compared with the 21 State inflow model. The purpose of this is to determine flight condition regions where a low – state inflow distribution do not greatly differ from the 21-state model and thus can be employed in that regions instead. Furthermore, an error line at 15% percent is drawn in all figures. This error limit is utilized in the Chapter 6 to determine a switching logic for varying state inflow model.

5.2. Collective – Inflow Relations

In this section simulations in *Table 5.1* are done in order to determine effects of collective to inflow distributions and transition from a state – number to another state -number.

The 8 tests conditions given in *Table 5.1* are repeated for 6, 10, 15 and 21 constant state inflow models making a total of 32 test combined. The results are presented such that for a given advance ratio and collective command 5-State, 10-State and 15-State are compared with the 21-State model. An example comparison at t=12 for these tests are given in the Appendix B.

Table 5.1. *Collective Tests*

Collective Simulations						
#	Collective (Deg)	Long Cyclic (Deg)	Lateral Cyclic (Deg)	Input Type	Input Time (Second)	Advance Ratio
1	5 to 20	0.0	0.0	Ramp	Between 2 - 12	0.00
2	5 to 20	0.0	0.0	Ramp	Between 2 - 12	0.10
3	5 to 20	0.0	0.0	Ramp	Between 2 - 12	0.20
4	5 to 20	0.0	0.0	Ramp	Between 2 - 12	0.30
5	20 to 5	0.0	0.0	Ramp	Between 2 - 12	0.00
6	20 to 5	0.0	0.0	Ramp	Between 2 - 12	0.10
7	20 to 5	0.0	0.0	Ramp	Between 2 - 12	0.20
8	20 to 5	0.0	0.0	Ramp	Between 2 - 12	0.30

5.2.1. Collective Up

The following collective input given in Figure 5.1 are given to the simulations run below for continuous collective up tests.

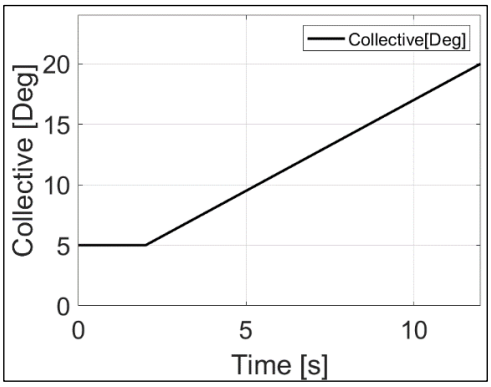

Figure 5.1. Collective Up Command for tests in Table 5.1. *Collective Tests* (1-2-3-4)

5.2.1.1. Advance Ratio: 0.0

The simulation results are presented below.

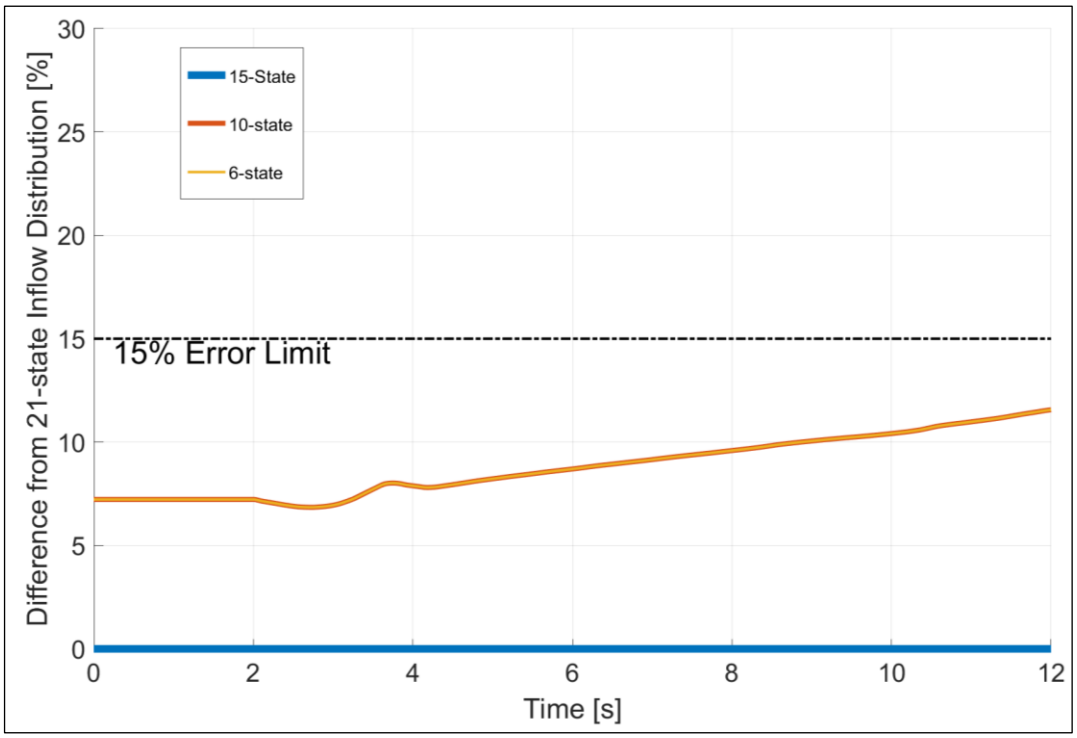

Figure 5.2. Continuous Collective Up at 0.0 advance ratio

In the Figure 5.2 the difference from 21-State inflow is same for 6 and 10 state inflow models because of the fact that both have the same number of "mean inflow" inflow states given in *Table 3.1* when r =2 , j = 0 for 6 state and r =3 , j = 0 for 10 state. Same holds for 15 and 21 state inflow distributions.

In the table below, 15% error crossings are given at zero advance ratio for collective up input.

Table 5.2. *15% Error Crossing Collective Values for Zero Advance Ratio*

State Number	15% Error Crossing Collective (deg)
6	-
10	-
15	-

Since none of the simulations for given inflow states crosses the 15% error at zero advance ratio, for varying-state implementation, during hover, 6 – state inflow model can be used for all collective range instead of 21 state.

5.2.1.2. Advance Ratio: 0.1

The simulation results are presented below.

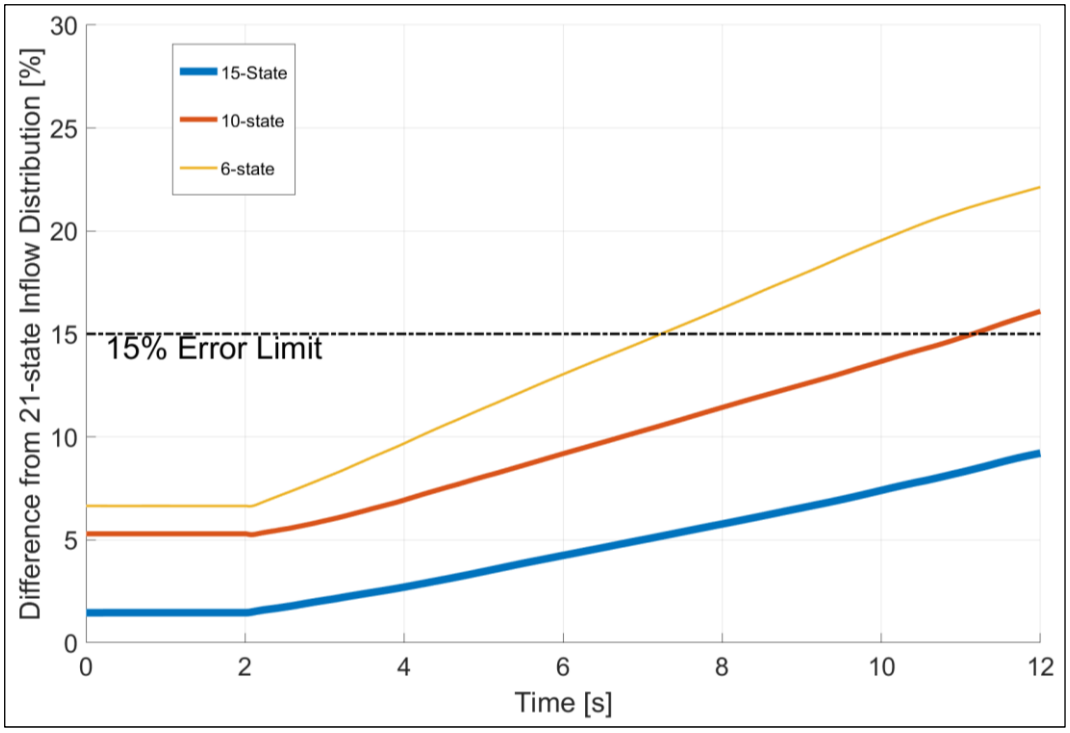

Figure 5.3. Continuous Collective Up at 0.1 advance ratio

As advance ratio increases, the asymmetry of inflow increases. Therefore, the difference between low-state and high-state inflow distribution increases.

In the table below, 15% error crossings are given at 0.1 advance ratio for collective up input.

Table 5.3. *15% Error Crossing Collective Values for 0.1 Advance Ratio*

State Number	15% Error Crossing Collective (deg)
6	12.00
10	17.00
15	-

The 6-State crosses 15% error threshold at 11 degrees collective input whereas 10 - State model crosses the threshold at 16 degrees. Note that 15 – State does not cross 15% error at 0.1 advance ratio.

5.2.1.3. Advance Ratio: 0.2

The simulation results are presented below.

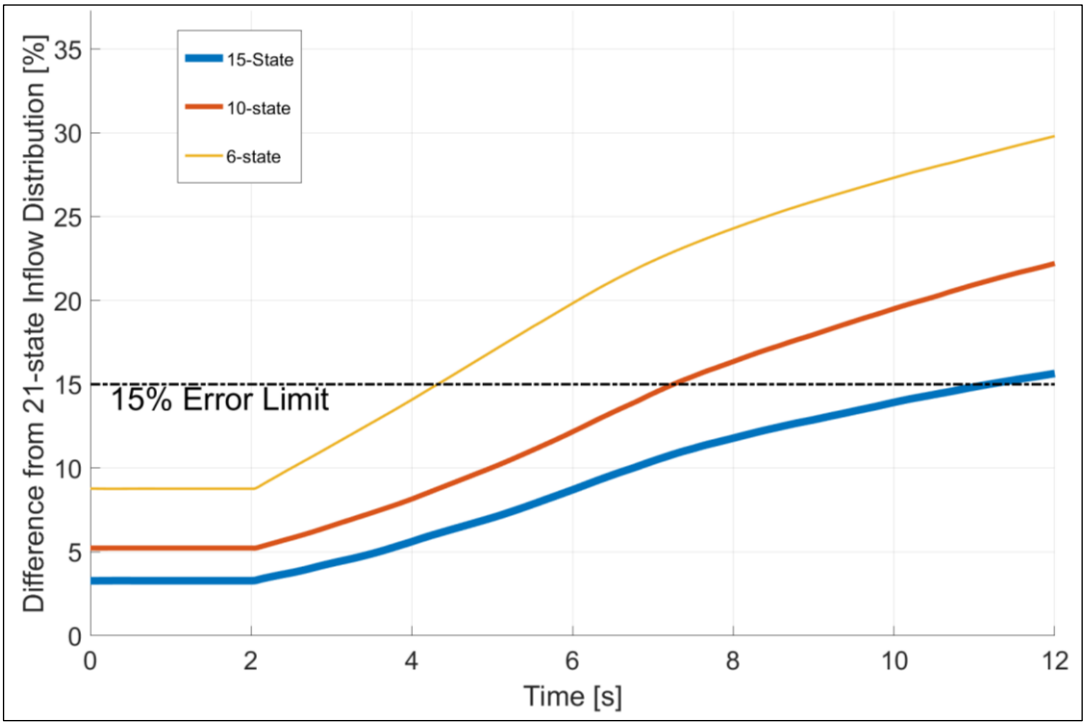

Figure 5.4. Continuous Collective Up at 0.2 advance ratio

In the table below, 15% error crossings are given at 0.2 advance ratio for collective up input.

Table 5.4. *15% Error Crossing Collective Values for 0.2 Advance Ratio*

State Number	15% Error Crossing Collective (deg)
6	8.00
10	12.00
15	18.00

5.2.1.4. Advance Ratio: 0.3

The simulation results are presented below.

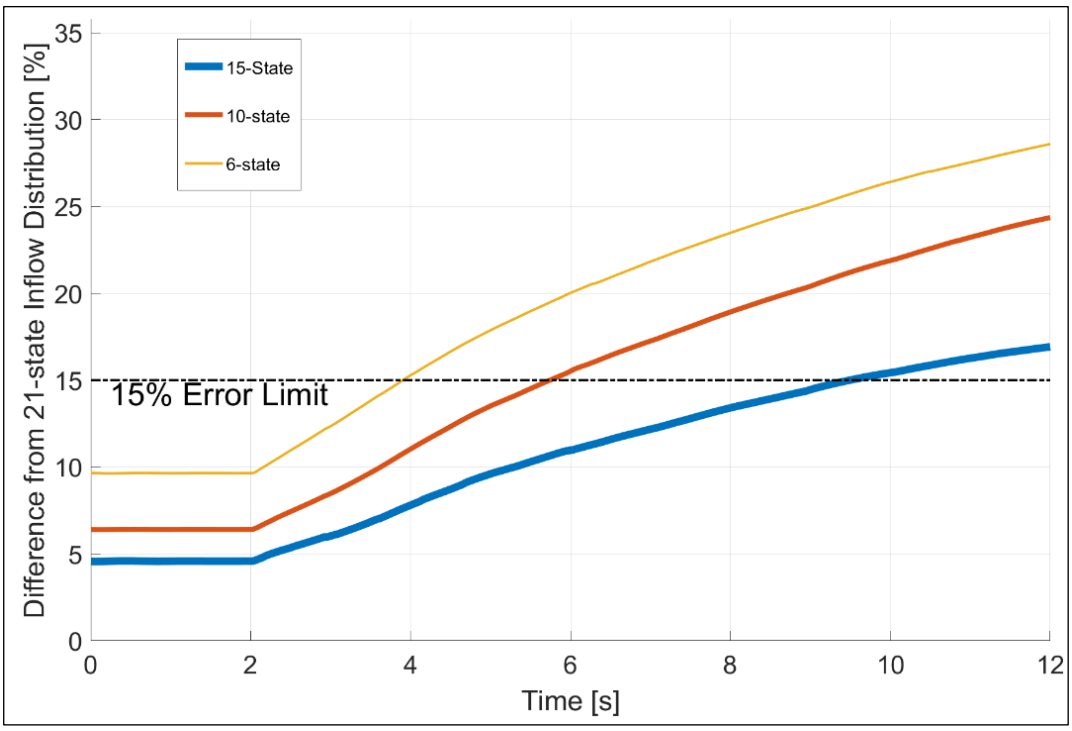

Figure 5.5. Continuous Collective Up at 0.3 advance ratio

In the table below, 15% error crossings are given at 0.3 advance ratio for collective up input.

Table 5.5. *15% Error Crossing Collective Values for 0.3 Advance Ratio*

State Number	15% Error Crossing Collective (deg)
6	7.00
10	10.00
15	15.00

5.2.2. Collective Down

The following collective input given in Figure 5.6 are given to the simulations run below for continuous collective down tests.

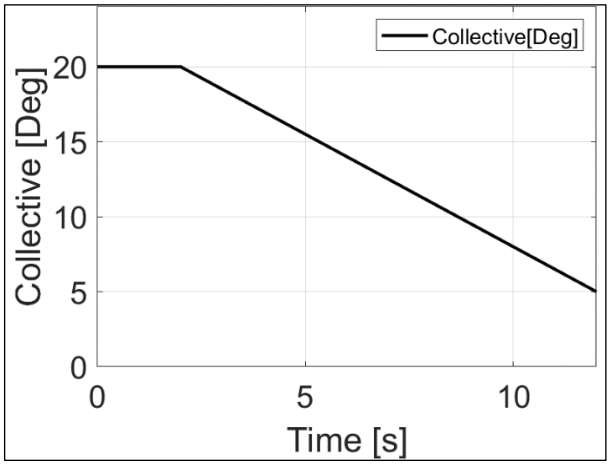

Figure 5.6. Collective Down Command for tests in Table 5.1. *Collective Tests* (5-6-7-8)

5.2.2.1. Advance Ratio: 0.0

The simulation results are presented below.

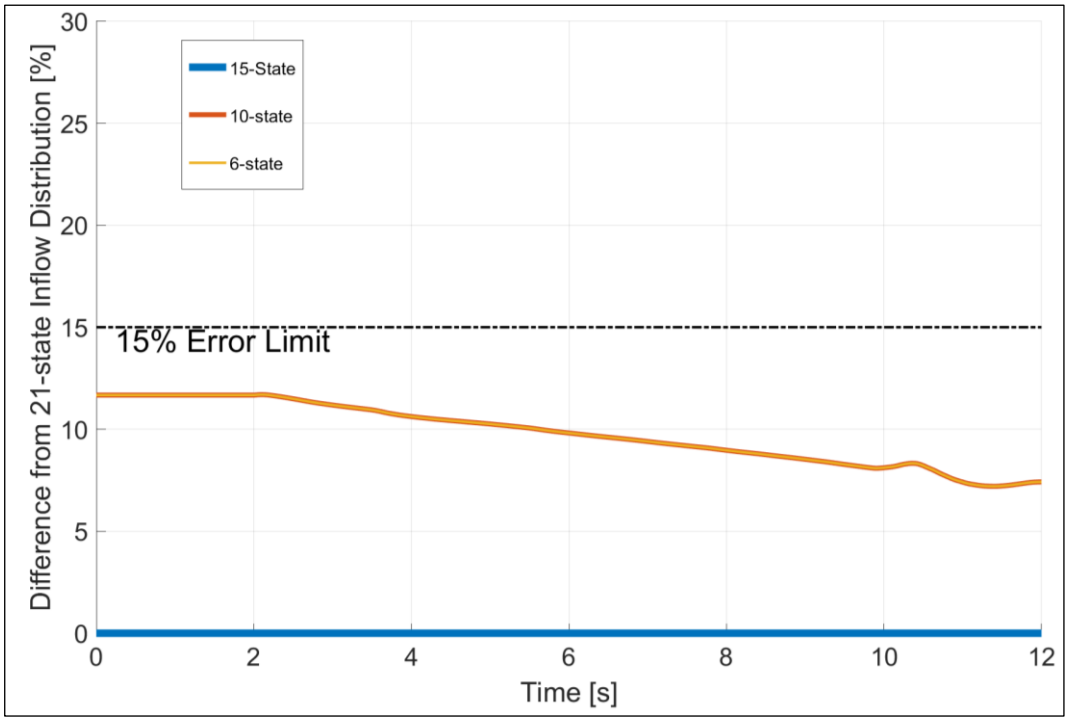

Figure 5.7. Continuous Collective Down at 0.0 advance ratio

In the table below, 15% error crossings are given at 0.0 advance ratio for collective down input.

Table 5.6. *15% Error Crossing Collective Values for 0.0 Advance Ratio*

State Number	15% Error Crossing Collective (deg)
6	-
10	-
15	-

5.2.2.2. Advance Ratio: 0.1

The simulation results are presented below.

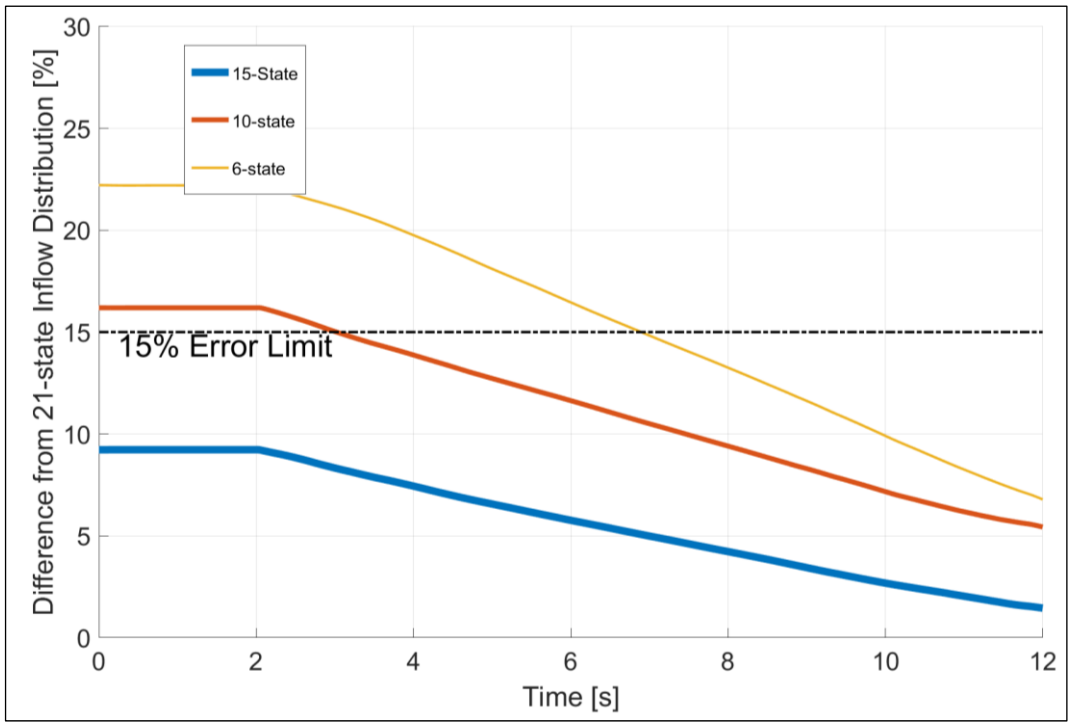

Figure 5.8. Continuous Collective Down at 0.1 advance ratio

In the table below, 15% error crossings are given at 0.1 advance ratio for collective down input.

Table 5.7. *15% Error Crossing Collective Values for 0.1 Advance Ratio*

State Number	15% Error Crossing Collective (deg)
6	13.00
10	18.00
15	-

5.2.2.3. Advance Ratio: 0.2

The simulation results are presented below.

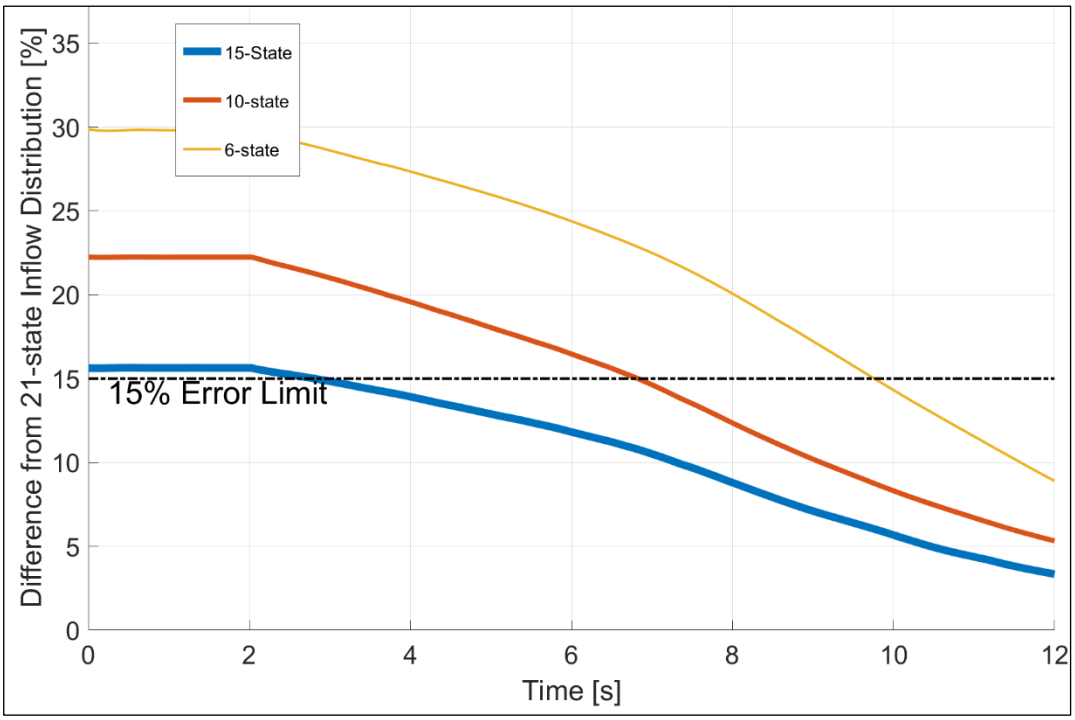

Figure 5.9. Continuous Collective Down at 0.2 advance ratio

In the table below, 15% error crossings are given at 0.2 advance ratio for collective down input.

Table 5.8. *15% Error Crossing Collective Values for 0.2 Advance Ratio*

State Number	15% Error Crossing Collective (deg)
6	8.00
10	13.00
15	19.00

5.2.2.4. Advance Ratio: 0.3

The simulation results are presented below.

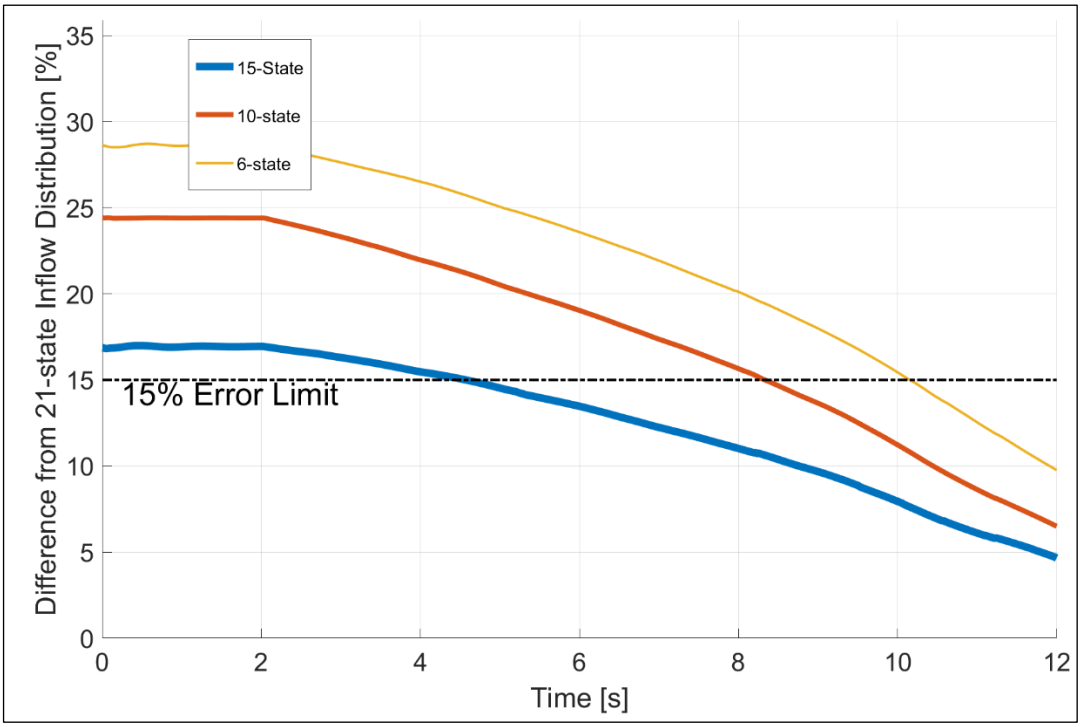

Figure 5.10. Continuous Collective Down at 0.3 advance ratio

In the table below, 15% error crossings are given at 0.3 advance ratio for collective down input.

Table 5.9. *15% Error Crossing Collective Values for 0.3 Advance Ratio*

State Number	15% Error Crossing Collective (deg)
6	7.00
10	11.00
15	17.00

5.3. Lateral Cyclic – Inflow Relations

In this section simulations in *Table 5.10* are done in order to determine effects of lateral cyclic to inflow distributions and transition from a state – number to another state - number.

The 8 tests conditions given in *Table 5.10* are repeated for 6, 10, 15 and 21 constant state inflow models making a total of 32 test combined. The results are presented such that for a given advance ratio and commands 5-State, 10-State and 15-State are compared with the 21-State model. An example comparison at t=12 for these tests are given in the Appendix B.

Table 5.10. *Lateral Cyclic Tests*

Lateral Cyclic Simulations						
#	Collective (Deg)	Long Cyclic (Deg)	Lateral Cyclic (Deg)	Input Type	Input Time (Second)	Advance Ratio
1	8.0	0.0	0 to 20	Ramp	Between 2 - 12	0.00
2	8.0	0.0	0to 20	Ramp	Between 2 - 12	0.10
3	8.0	0.0	0 to 20	Ramp	Between 2 - 12	0.20
4	8.0	0.0	0 to 20	Ramp	Between 2 - 12	0.30
5	8.0	0.0	0 to -20	Ramp	Between 2 - 12	0.00
6	8.0	0.0	0 to -20	Ramp	Between 2 - 12	0.10
7	8.0	0.0	0 to -20	Ramp	Between 2 - 12	0.20
8	8.0	0.0	0 to -20	Ramp	Between 2 - 12	0.30

5.3.1. Lateral Cyclic Right

The following lateral cyclic input given in Figure 5.11 are given to the simulations run below for lateral cyclic right tests.

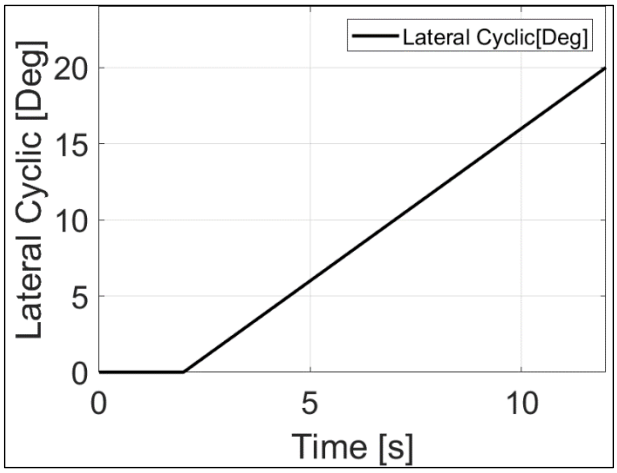

Figure 5.11. Lateral Cyclic Command for tests in Table 5.10 (Tests 1-2-3-4)

5.3.1.1. Advance Ratio: 0.0

The simulation results are presented below.

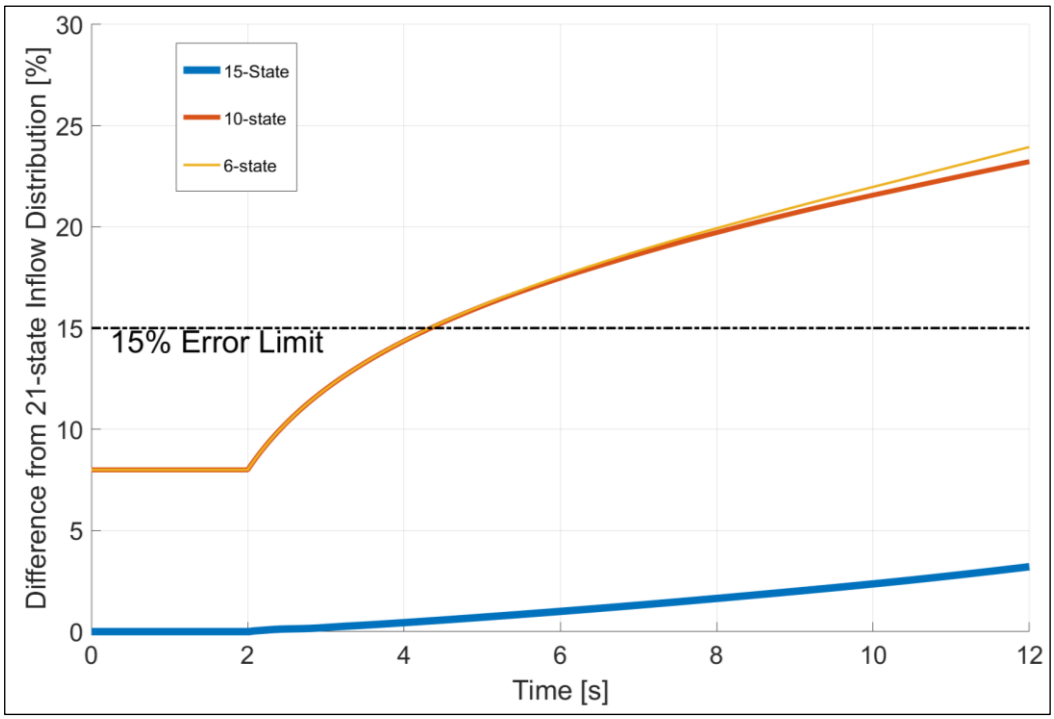

Figure 5.12. Lateral Cyclic Right at 0.0 advance ratio

In the table below, 15% error crossings are given at zero advance ratio for lateral cyclic right input.

Table 5.11. *15% Error Crossing Lateral* Cyclic *Values for Zero Advance Ratio*

State Number	15% Error Crossing Lateral Cyclic (deg)
6	4.00
10	4.00
15	-

5.3.1.2. Advance Ratio: 0.1

The simulation results are presented below.

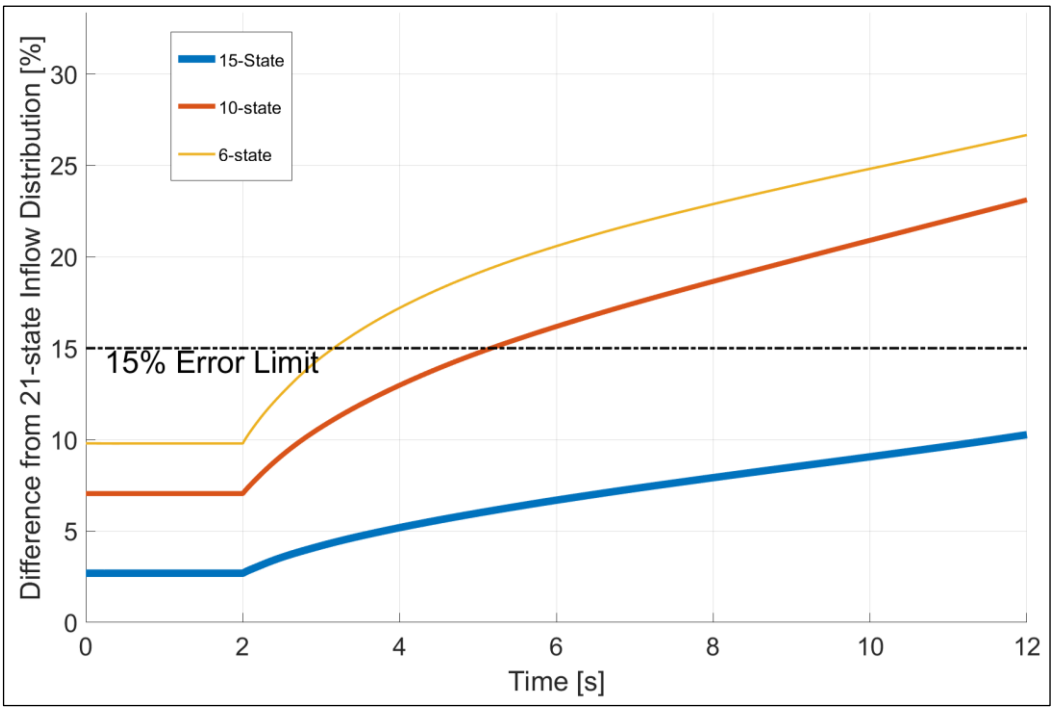

Figure 5.13. Lateral Cyclic Right at 0.1 advance ratio

In the table below, 15% error crossings are given at 0.1 advance ratio for lateral cyclic right input.

Table 5.12. *15% Error Crossing* Lateral Cyclic *Values for 0.1 Advance Ratio*

State Number	15% Error Crossing Lateral Cyclic (deg)
6	2.00
10	6.00
15	-

5.3.1.3. Advance Ratio: 0.2

The simulation results are presented below.

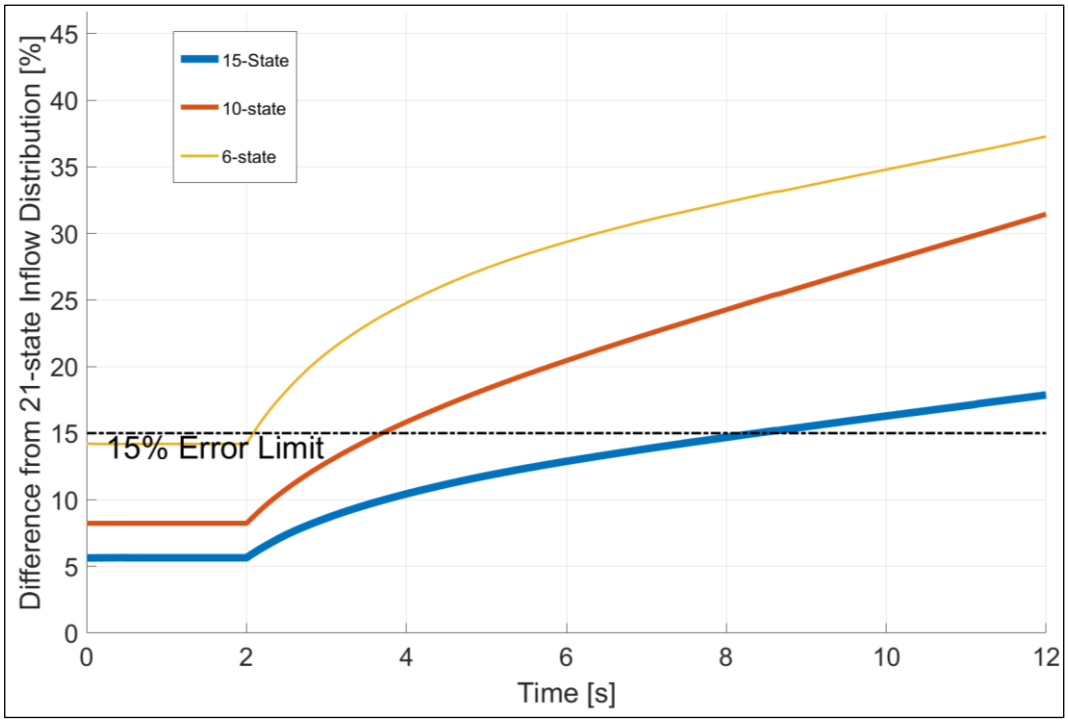

Figure 5.14. Lateral Cyclic Right at 0.2 advance ratio

In the table below, 15% error crossings are given at 0.2 advance ratio for lateral cyclic right input.

Table 5.13. *15% Error Crossing* Lateral Cyclic *Values for 0.2 Advance Ratio*

State Number	15% Error Crossing Lateral Cyclic (deg)
6	1.00
10	4.00
15	12.00

5.3.1.4. Advance Ratio: 0.3

The simulation results are presented below.

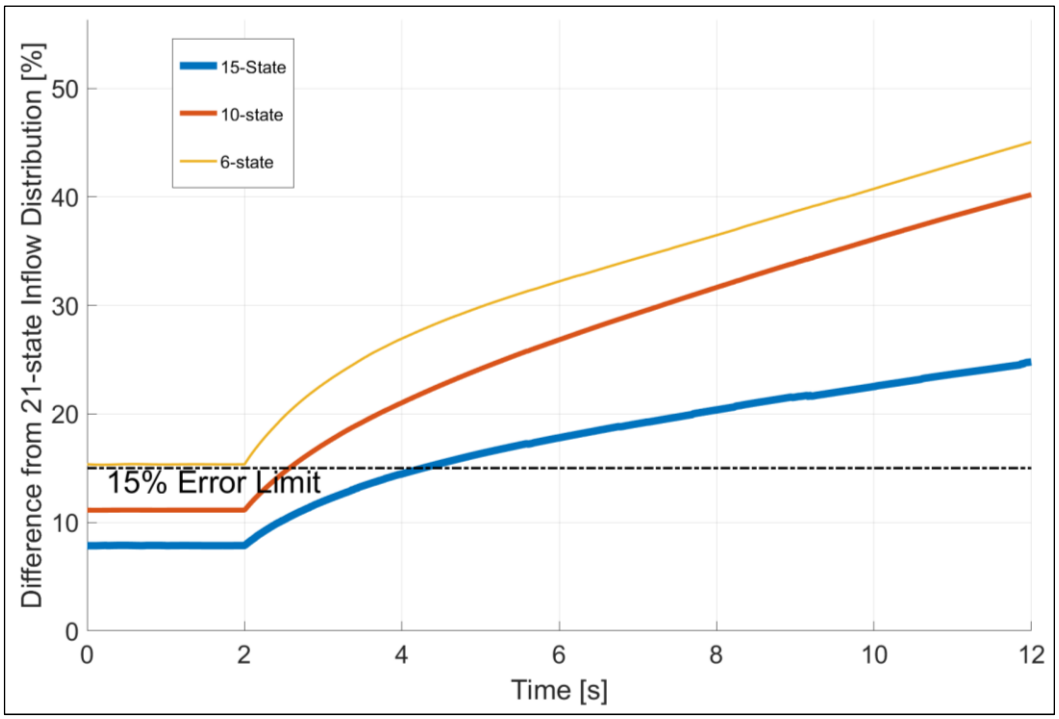

Figure 5.15. Lateral Cyclic Right at 0.3 advance ratio

In the table below, 15% error crossings are given at 0.3 advance ratio for lateral cyclic right input.

Table 5.14. *15% Error Crossing Lateral Cyclic Values for 0.3 Advance Ratio*

State Number	15%Error Crossing Lateral Cyclic (deg)
6	0.00
10	1.00
15	4.00

5.3.2. Lateral Cyclic Left

The following lateral cyclic input given Figure 5.16 are given to the simulations run below lateral cyclic left tests.

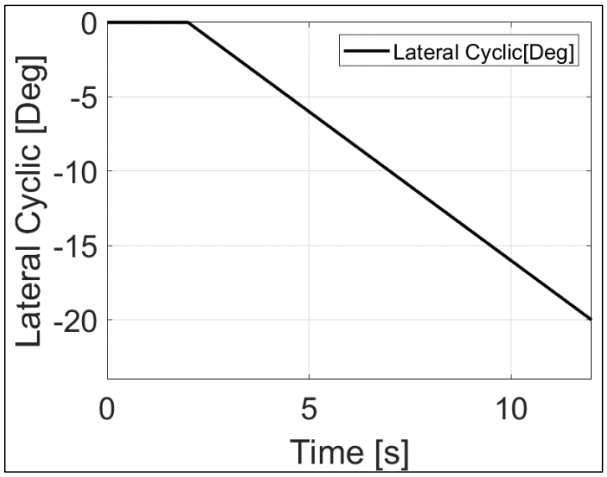

Figure 5.16. Lateral Cyclic Command for tests in Table 5.10 (Tests 5-6-7-8)

5.3.2.1. Advance Ratio: 0.0

The simulation results are presented below.

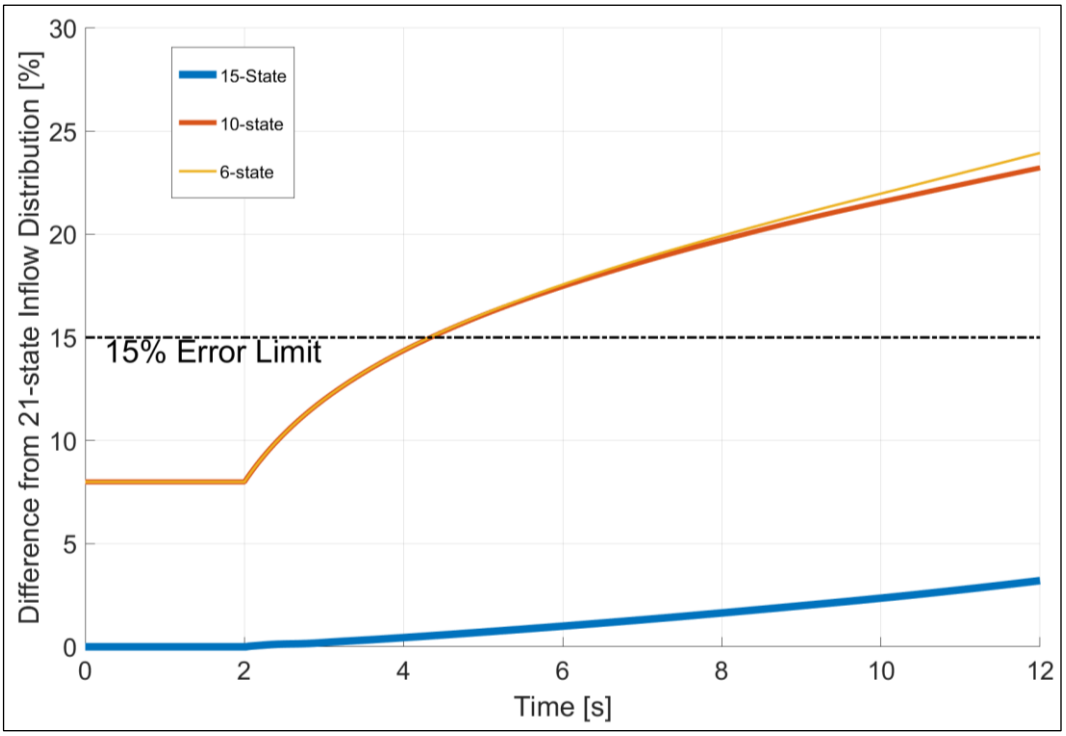

Figure 5.17. Lateral Cyclic Left at 0.0 advance ratio

In the table below, 15% error crossings are given at 0.0 advance ratio for lateral cyclic left input.

Table 5.15. *15% Error Crossing Lateral Cyclic Values for 0.0 Advance Ratio*

State Number	15%Error Crossing Lateral Cyclic (deg)
6	4.00
10	4.00
15	-

5.3.2.2. Advance Ratio: 0.1

The simulation results are presented below.

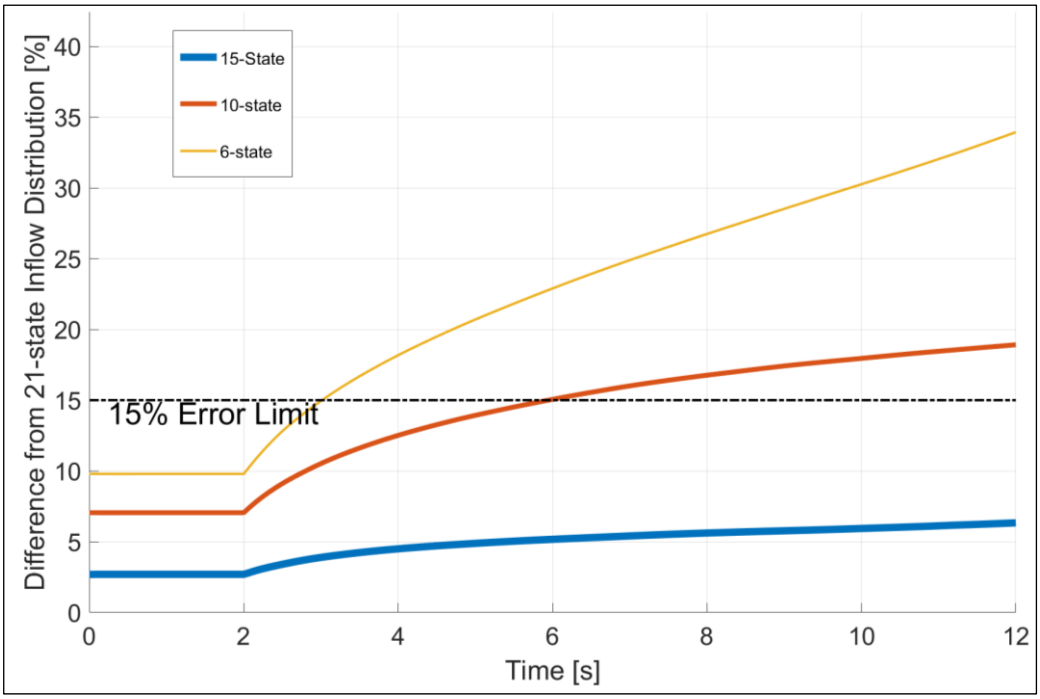

Figure 5.18. Lateral Cyclic Left at 0.1 advance ratio

In the table below, 15% error crossings are given at 0.1 advance ratio for lateral cyclic input.

Table 5.16. *15% Error Crossing Lateral Cyclic Values for 0.1 Advance Ratio*

State Number	15%Error Crossing Lateral Cyclic (deg)
6	2.00
10	8.00
15	-

5.3.2.3. Advance Ratio: 0.2

The simulation results are presented below.

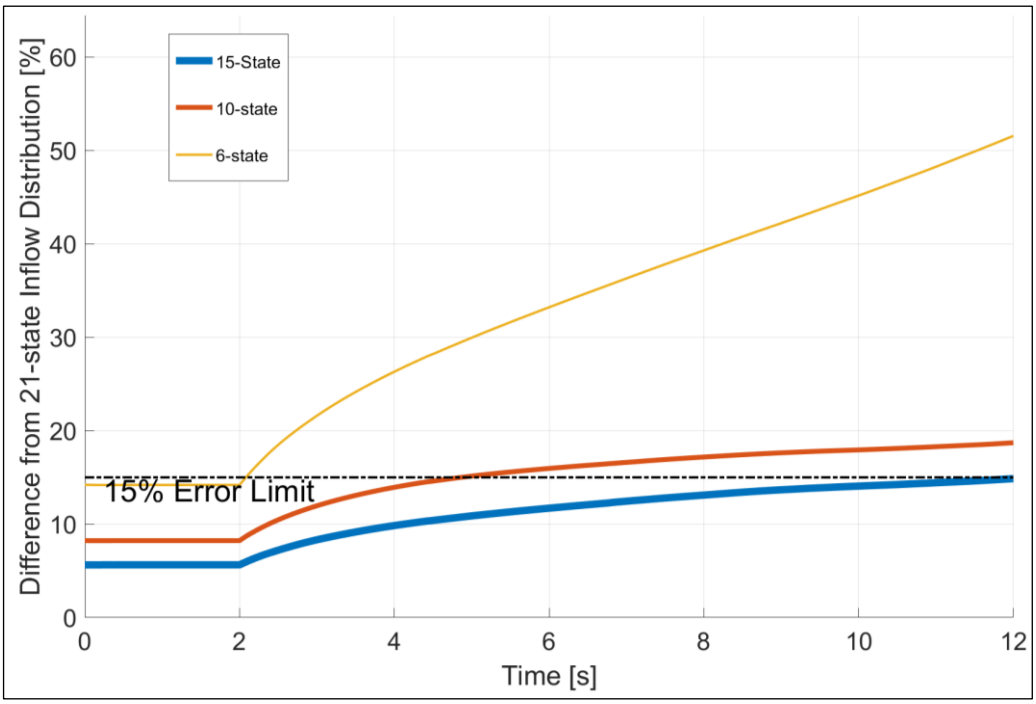

Figure 5.19. Lateral Cyclic Left at 0.2 advance ratio

In the table below, 15% error crossings are given at 0.2 advance ratio for lateral cyclic input.

Table 5.17. *15% Error Crossing Lateral Cyclic Values for 0.2 Advance Ratio*

State Number	15%Error Crossing Lateral Cyclic (deg)
6	0.00
10	5.00
15	20.00

5.3.2.4. Advance Ratio: 0.3

The simulation results are presented below.

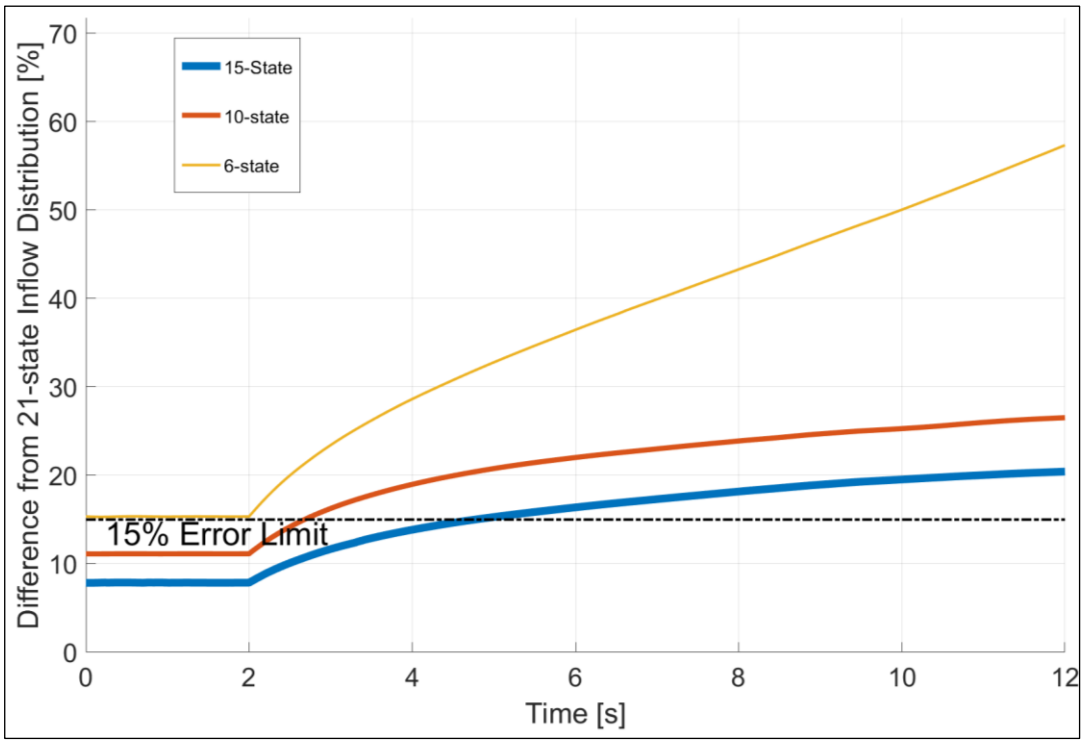

Figure 5.20. Lateral Cyclic Left at 0.3 advance ratio

In the table below, 15% error crossings are given at 0.3 advance ratio for lateral cyclic input.

Table 5.18. *15% Error Crossing Lateral Cyclic Values for 0.3 Advance Ratio*

State Number	15%Error Crossing Lateral Cyclic (deg)
6	0.00
10	1.50
15	6.00

5.4. Longitudinal Cyclic – Inflow Relations

In this section simulations in *Table 5.19* are done in order to determine effects of longitudinal cyclic to inflow distributions and transition from a state – number to another state -number.

The 8 tests conditions given in *Table 5.19* are repeated for 6, 10, 15 and 21 constant state inflow models making a total of 32 test combined. The results are presented such that for a given advance ratio and commands 5-State, 10-State and 15-State are compared with the 21-State model. An example comparison at t=12 for these tests are given in the Appendix B.

Table 5.19 *Longitudinal Cyclic Tests*

Longitudinal Cyclic Simulations						
#	Collective (Deg)	Long Cyclic (Deg)	Lateral Cyclic (Deg)	Input Type	Input Time (Second)	Advance Ratio
1	8.0	0 to 20	0.0	Ramp	Between 2 - 12	0.00
2	8.0	0to 20	0.0	Ramp	Between 2 - 12	0.10
3	8.0	0 to 20	0.0	Ramp	Between 2 - 12	0.20
4	8.0	0 to 20	0.0	Ramp	Between 2 - 12	0.30
5	8.0	0 to -20	0.0	Ramp	Between 2 - 12	0.00
6	8.0	0 to -20	0.0	Ramp	Between 2 - 12	0.10
7	8.0	0 to -20	0.0	Ramp	Between 2 - 12	0.20
8	8.0	0 to -20	0.0	Ramp	Between 2 - 12	0.30

5.4.1. Longitudinal Cyclic Forward

The following longitudinal cyclic input given in Figure 5.21 are given to the simulations run below for longitudinal cyclic forward tests.

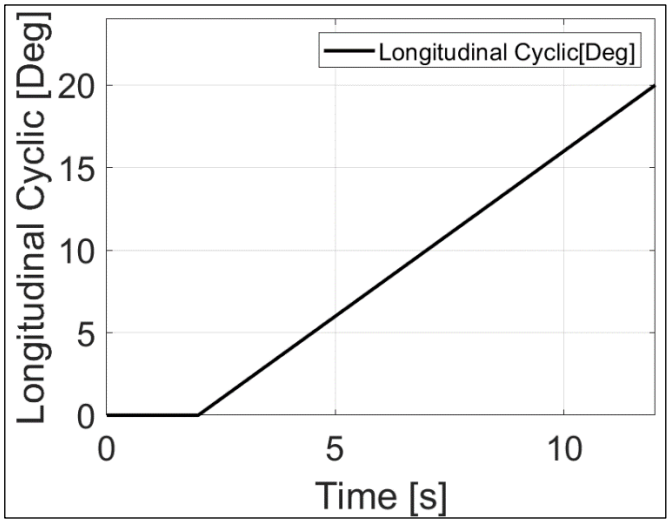

Figure 5.21. Longitudinal Cyclic Command for tests in Table 5.19 (Tests 1-2-3-4)

5.4.1.1. Advance Ratio: 0.0

The simulation results are presented below.

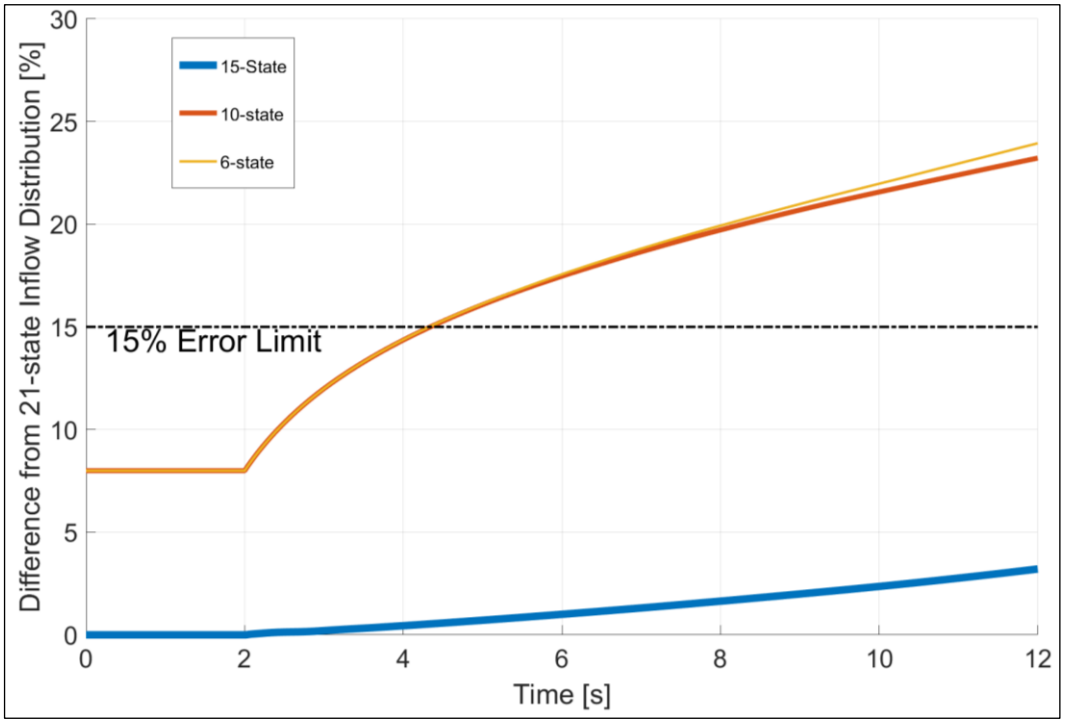

Figure 5.22. Longitudinal Cyclic Forward at 0.0 advance ratio

In the table below, 15% error crossings are given at zero advance ratio for longitudinal cyclic forward input.

Table 5.20. *15% Error Crossing Long* Cyclic *Values for Zero Advance Ratio*

State Number	15%Error Crossing Longitudinal Cyclic (deg)
6	4.00
10	4.00
15	-

5.4.1.2. Advance Ratio: 0.1

The simulation results are presented below.

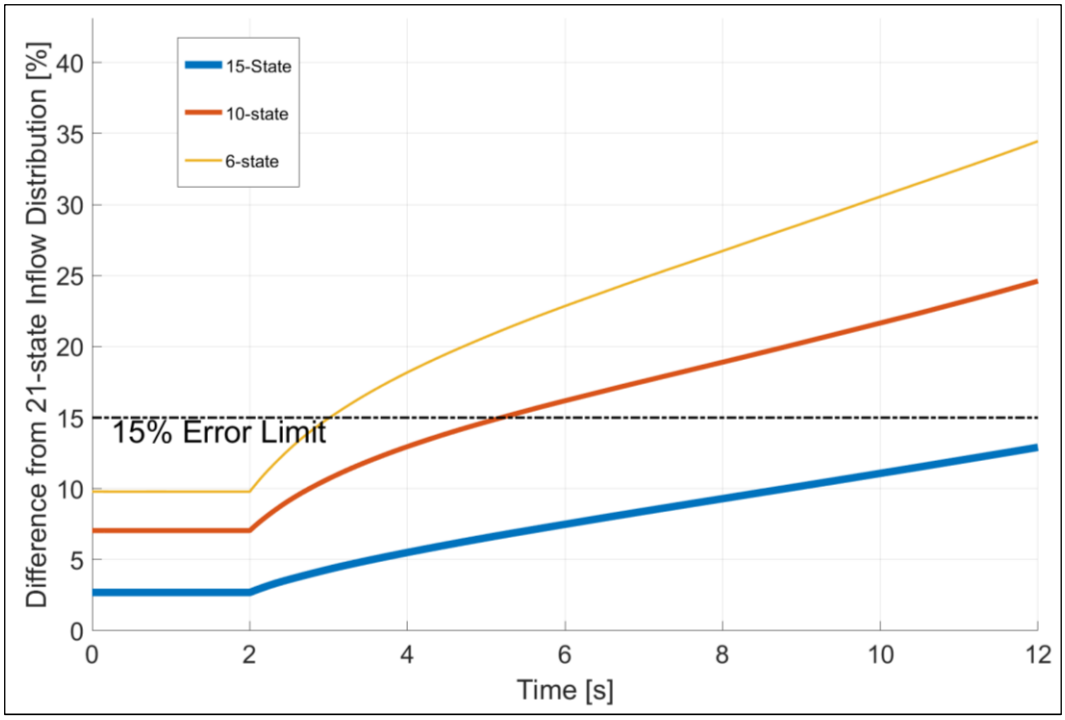

Figure 5.23. Longitudinal Cyclic Forward at 0.1 advance ratio

In the table below, 15% error crossings are given at 0.1 advance ratio for longitudinal cyclic input.

Table 5.21. *15% Error Crossing Long Cyclic Values for 0.1 Advance Ratio*

State Number	15%Error Crossing Longitudinal Cyclic (deg)
6	2.00
10	6.00
15	-

5.4.1.3. Advance Ratio: 0.2

The simulation results are presented below.

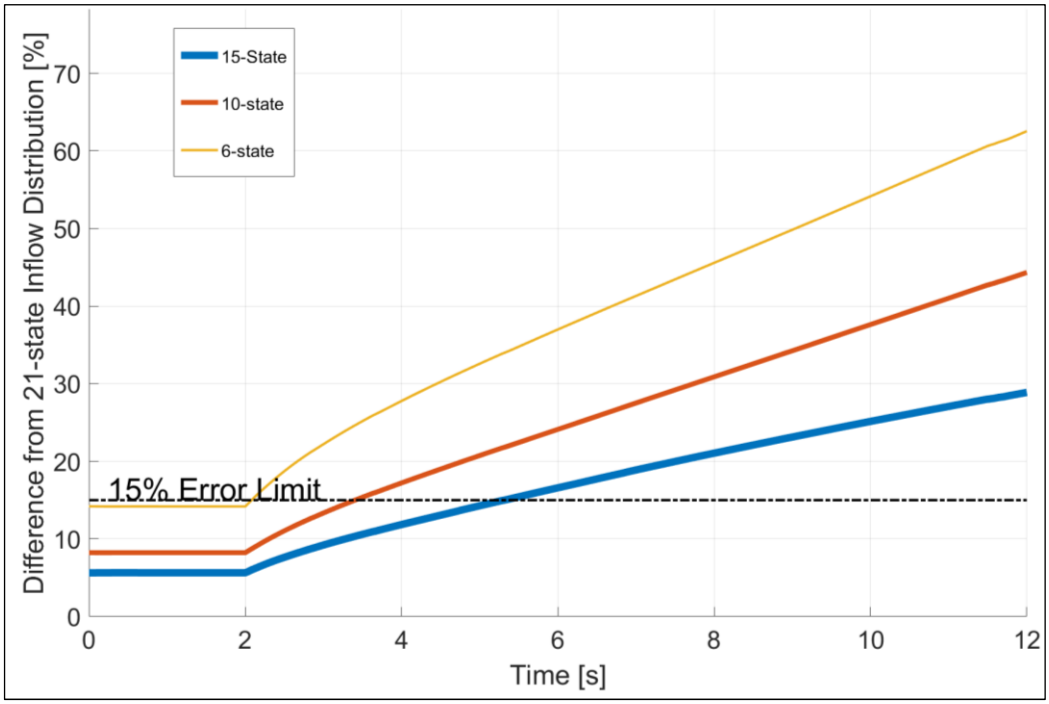

Figure 5.24. Longitudinal Cyclic Forward at 0.2 advance ratio

In the table below, 15% error crossings are given at 0.2 advance ratio for longitudinal cyclic input.

Table 5.22. *15% Error Crossing Long Cyclic Values for 0.2 Advance Ratio*

State Number	15% Error Crossing Longitudinal Cyclic (deg)
6	1.00
10	3.00
15	7.00

5.4.1.4. Advance Ratio: 0.3

The simulation results are presented below.

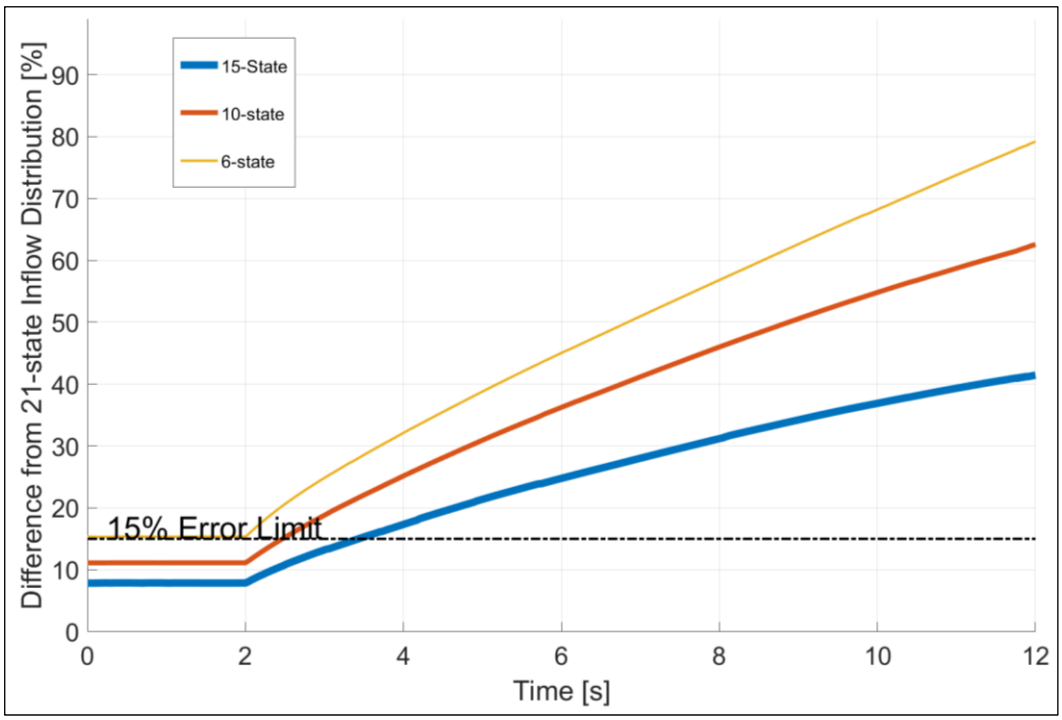

Figure 5.25. Longitudinal Cyclic Forward at 0.3 advance ratio

In the table below, 15% error crossings are given at 0.3 advance ratio for longitudinal cyclic input.

Table 5.23. *15% Error Crossing Long Cyclic Values for 0.3 Advance Ratio*

State Number	15% Error Crossing Longitudinal Cyclic (deg)
6	1.00
10	2.00
15	4.00

5.4.2. Longitudinal Cyclic Aftward

The following longitudinal cyclic input in Figure 5.26 are given to the simulations of longitudinal cyclic aftward tests.

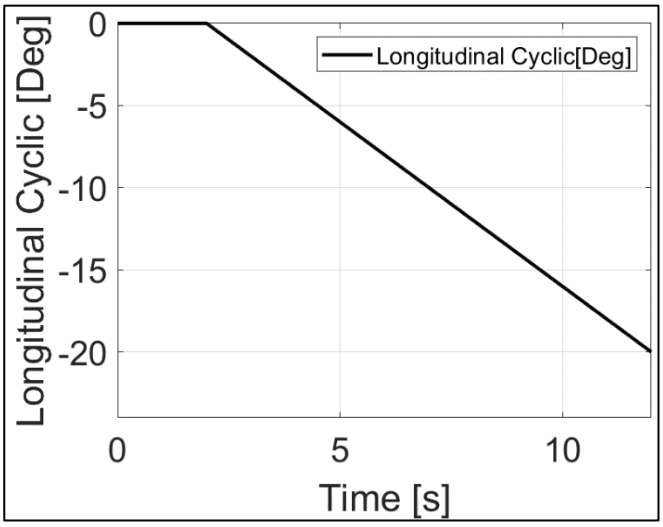

Figure 5.26. Longitudinal Cyclic Command for tests in Table 5.19 (Tests 5-6-7-8)

5.4.2.1. Advance Ratio: 0.0

The simulation results are presented below.

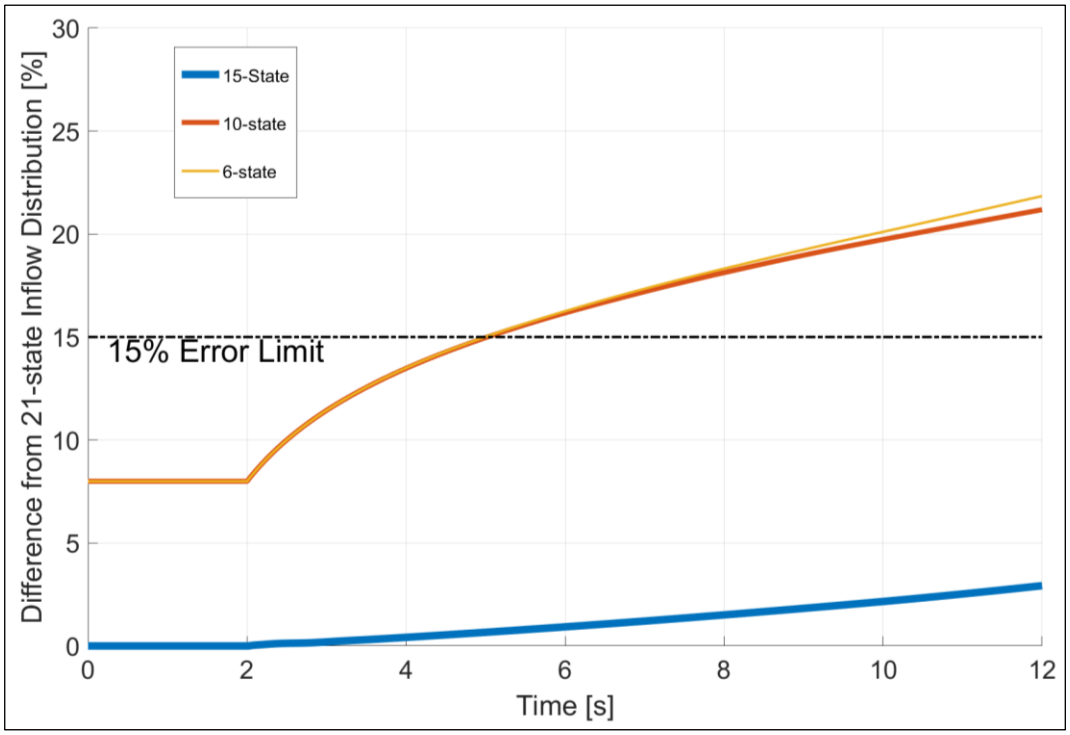

Figure 5.27. Longitudinal Cyclic Aftward at 0.0 advance ratio

In the table below, 15% error crossings are given at 0.0 advance ratio for longitudinal cyclic input.

Table 5.24. *15% Error Crossing Long Cyclic Values for 0.0 Advance Ratio*

State Number	15%Error Crossing Longitudinal Cyclic (deg)
6	5.00
10	5.00
15	-

5.4.2.2. Advance Ratio: 0.1

The simulation results are presented below.

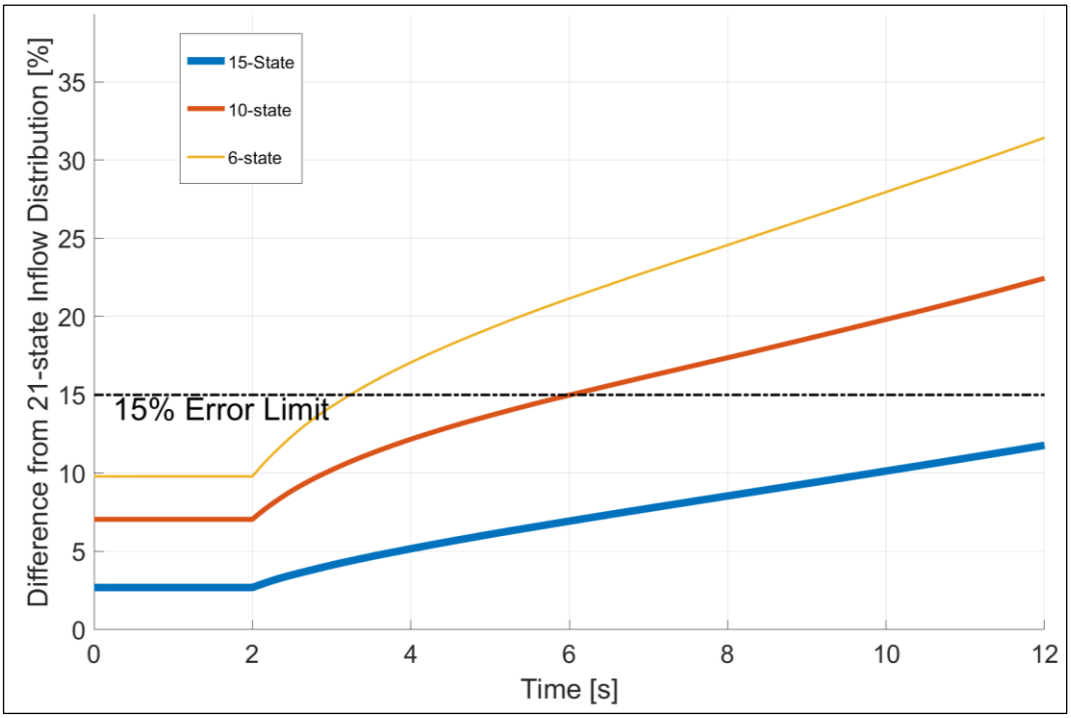

Figure 5.28. Longitudinal Cyclic Aftward at 0.1 advance ratio

In the table below, 15% error crossings are given at 0.1 advance ratio for longitudinal cyclic input.

Table 5.25. *15% Error Crossing Long Cyclic Values for 0.1 Advance Ratio*

State Number	15% Error Crossing Longitudinal Cyclic (deg)
6	2.00
10	8.00
15	-

5.4.2.3. Advance Ratio: 0.2

The simulation results are presented below.

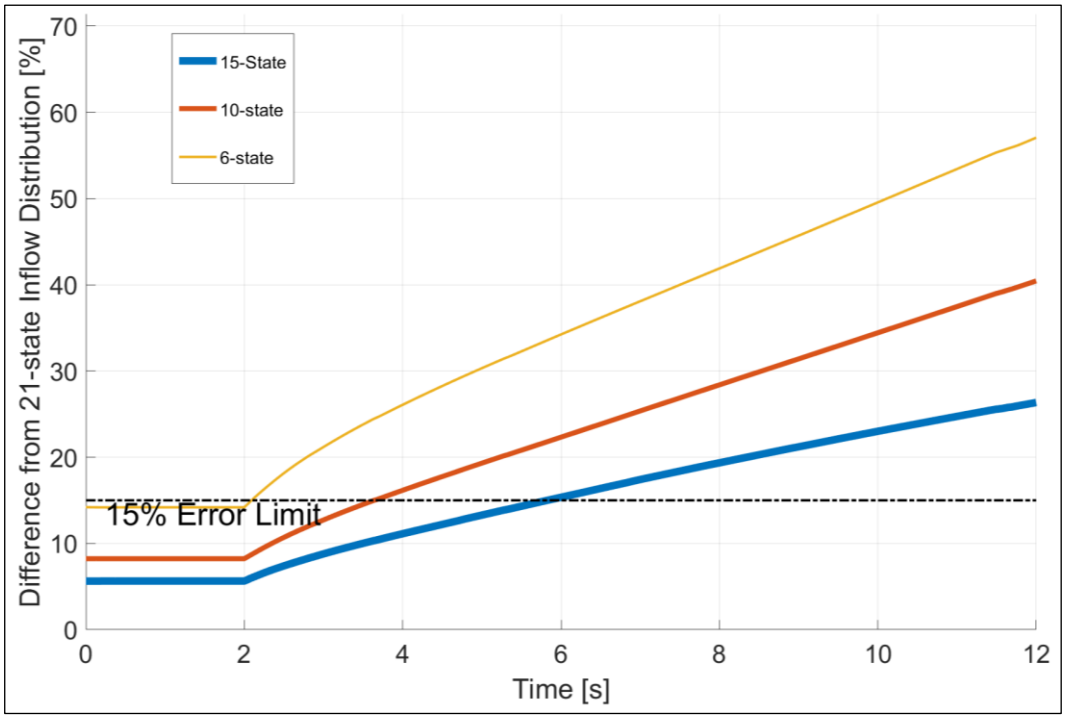

Figure 5.29. Longitudinal Cyclic Aftward at 0.2 advance ratio

In the table below, 15% error crossings are given at 0.2 advance ratio for longitudinal cyclic input.

Table 5.26. *15% Error Crossing Long Cyclic Values for 0.2 Advance Ratio*

State Number	15% Error Crossing Longitudinal Cyclic (deg)
6	1.00
10	3.00
15	7.00

5.4.2.4. Advance Ratio: 0.3

The simulation results are presented below.

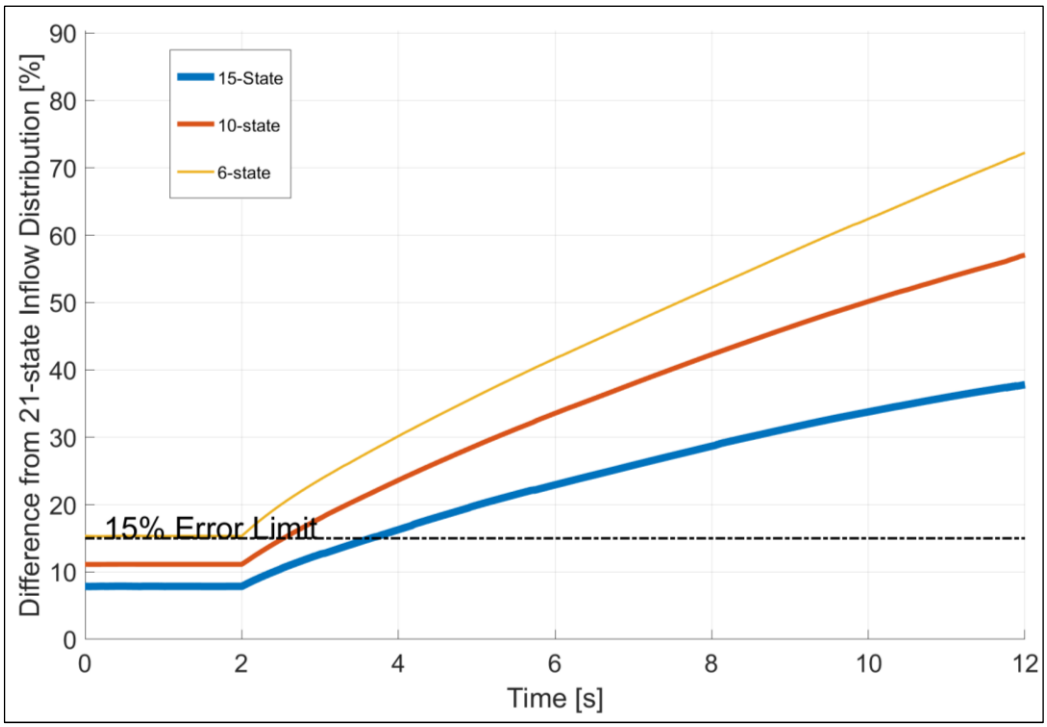

Figure 5.30 Longitudinal Cyclic Aftward at 0.3 advance ratio

In the table below, 15% error crossings are given at 0.3 advance ratio for longitudinal cyclic input.

Table 5.27. *15% Error Crossing Long Cyclic Values for 0.3 Advance Ratio*

State Number	15% Error Crossing Longitudinal Cyclic (deg)
6	1.00
10	2.00
15	5.00

CHAPTER 6

SIMULATIONS WITH VARYING STATE PETERS – HE MODEL

6.1. State Number Switching Logic

Throughout the Chapter 6, the limits of the control inputs -at which the respective state numbers for Peters – He inflow distribution differentiate from the 21 State inflow- are investigated. These limits for given advance ratio and control position combinations are given in from *Table 5.2* to *Table 5.27*. These limits are used to determine the Peters – He state number for varying state model implementation.

In following sections, the control position limits for given advance ratios are shown. Inside yellow limits 6-state inflow model, inside red limits 10-state inflow model and inside blue limits 15-state inflow model is used. Outside these limits 21-state model is used to represent inflow distribution.

6.2. Rectangular Cyclic Limits

In this section, the cyclic limits are given as a rectangle which computed throughout the Chapter 5. In the following long tests under this section 6.2 are implemented using rectangular limits for cyclic controls.

6.2.1. Zero Advance Ratio

When rotor is at zero advance ratio, for varying number inflow implementation, following figures are taken as references.

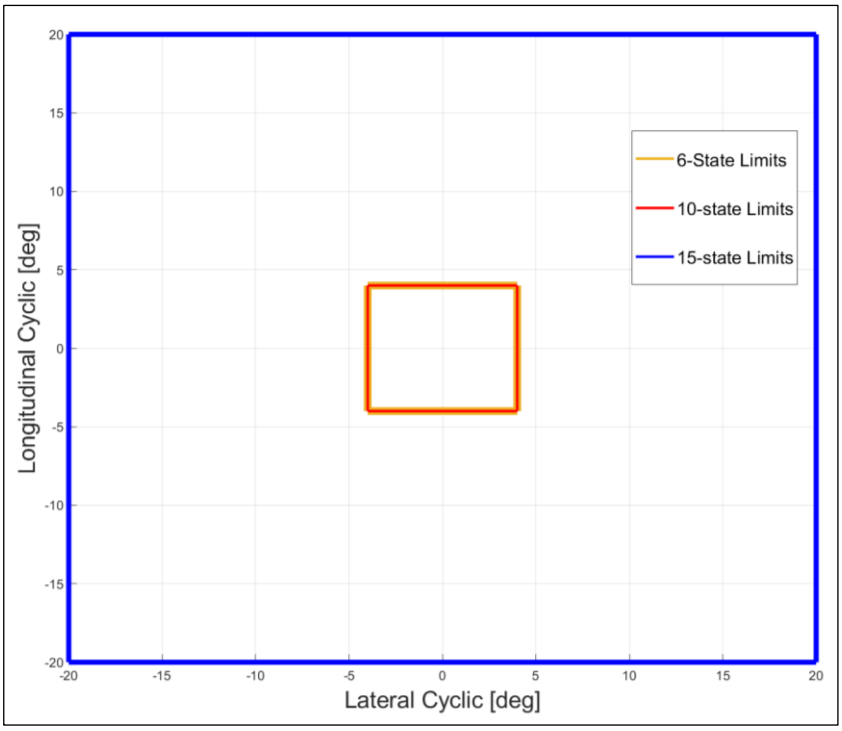

Figure 6.1. Cyclic limits at zero advance ratio

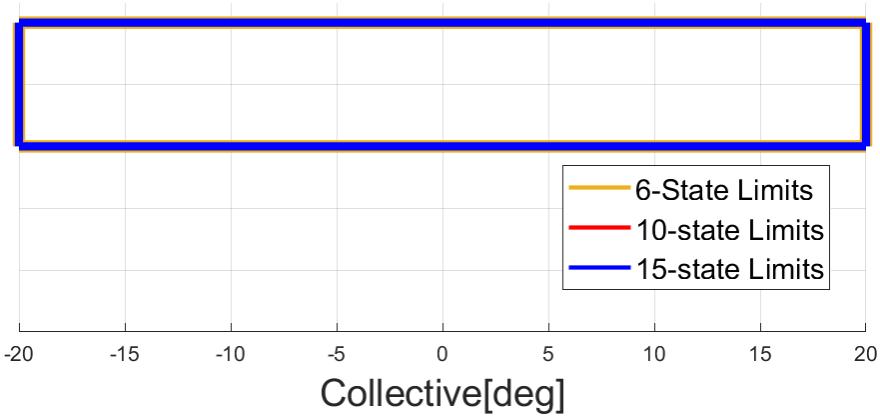

Figure 6.2. Collective limit at zero advance ratio

6.2.2. 0.1 Advance Ratio

When rotor is at 0.1 advance ratio, for varying state number inflow implementation, following figures are taken as references.

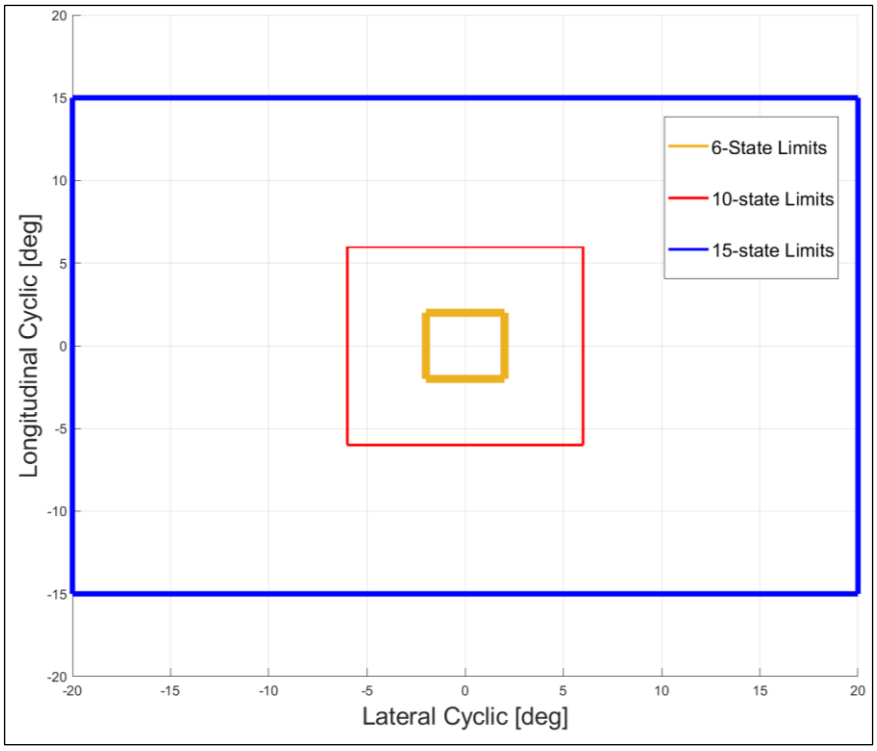

Figure 6.3. Cyclic limits at 0.1 advance ratio

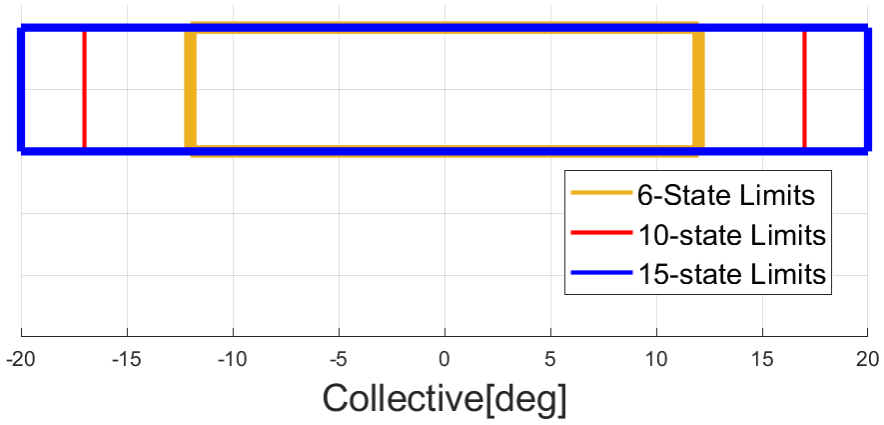

Figure 6.4. Collective limit at 0.1 advance ratio

6.2.3. 0.2 Advance Ratio

When rotor is at 0.2 advance ratio, for varying state number inflow implementation, following figures are taken as references.

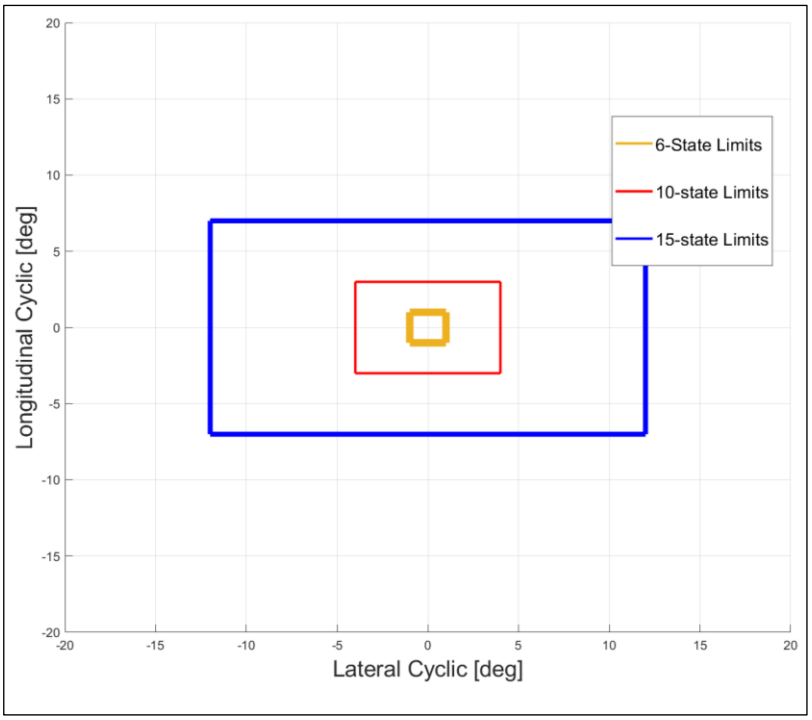

Figure 6.5. Cyclic limits at 0.2 advance ratio

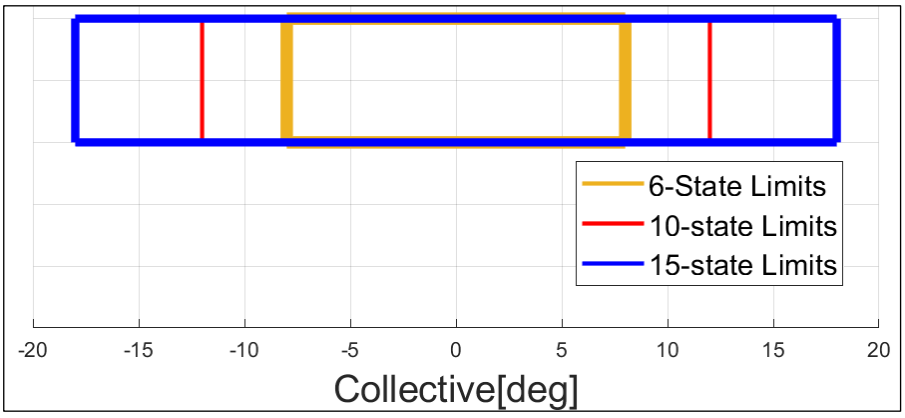

Figure 6.6. Collective limit at 0.2 advance ratio

6.2.4. 0.3 Advance Ratio

When rotor is at 0.3 advance ratio, for varying state number inflow implementation, following figures are taken as references.

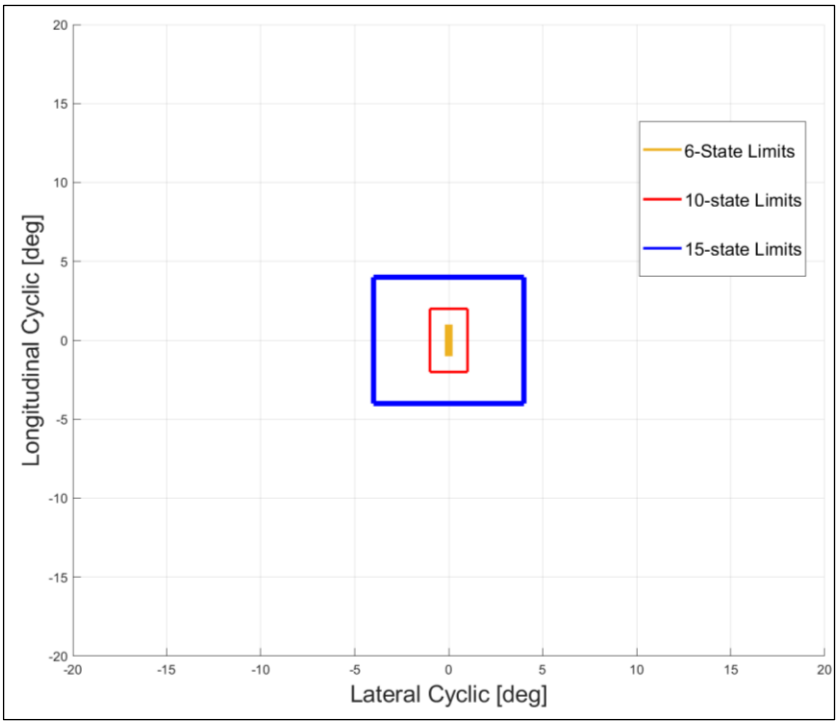

Figure 6.7. Cyclic limits at 0.3 advance ratio

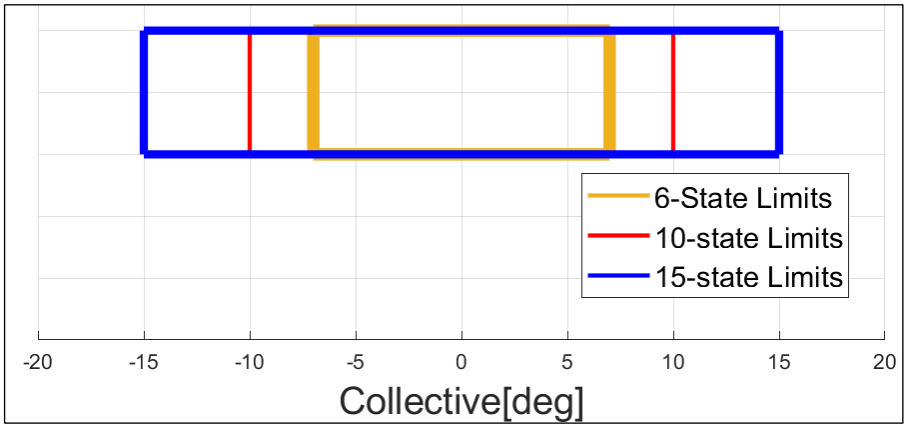

Figure 6.8. Collective limit at 0.3 advance ratio

6.2.5. Simulation Comparison for Rectangular Limits

A state switching logic is implemented using the control limits at given advance ratios given in section 6.2. Then two simulations are made with varying state inflow model. First one is a increasing-advance-ratio test where the advance ratio is gradually increased and triangle waves with different phases and frequencies are fed as collective & longitudinal cyclic & lateral cyclic inputs. A representation of speed up maneuver is aimed with such inputs to model. Secondly, a descreasing-advance-ratio simulation is run with same inputs for collective and cyclic inputs. The results are investigated below.

6.2.5.1. Increasing Advance Ratio Simulation

In this section, a 140-second-long increasing-advance-ratio simulation is run. Advance ratio and collective and cyclic inputs are given in below figures.

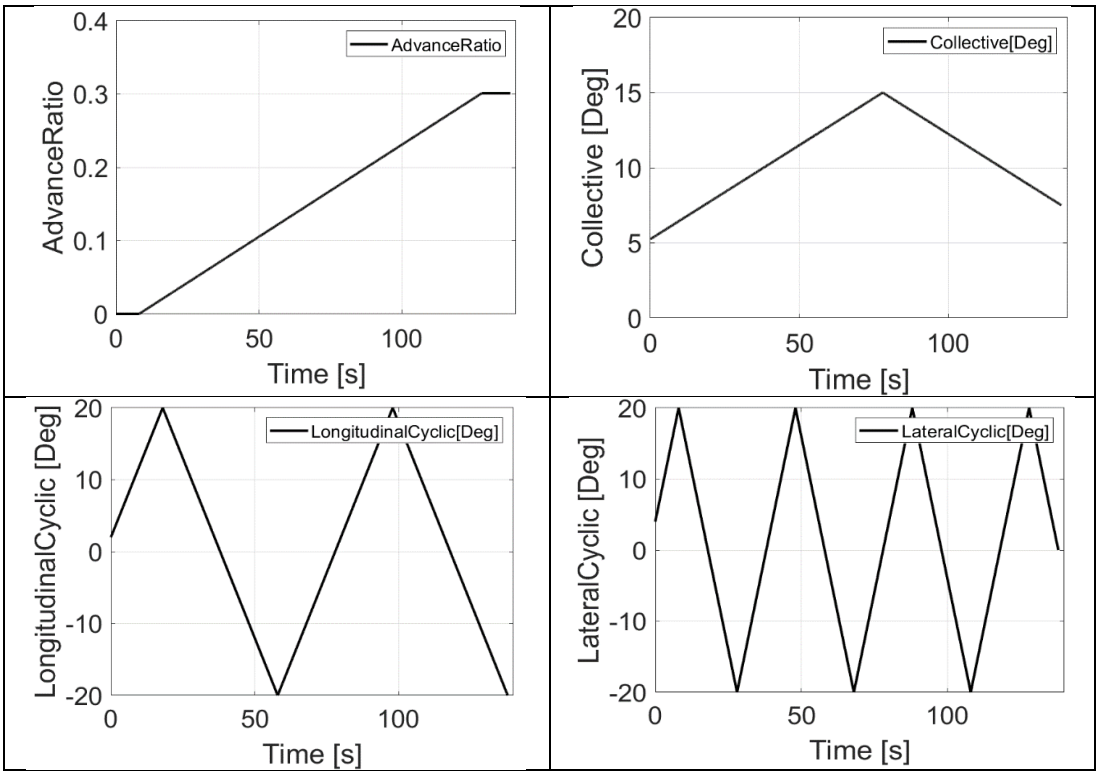

Figure 6.9. Speed Up Test Inputs

In the figure below the difference with respect to 21 state inflow is investigated for varying state inflow model.

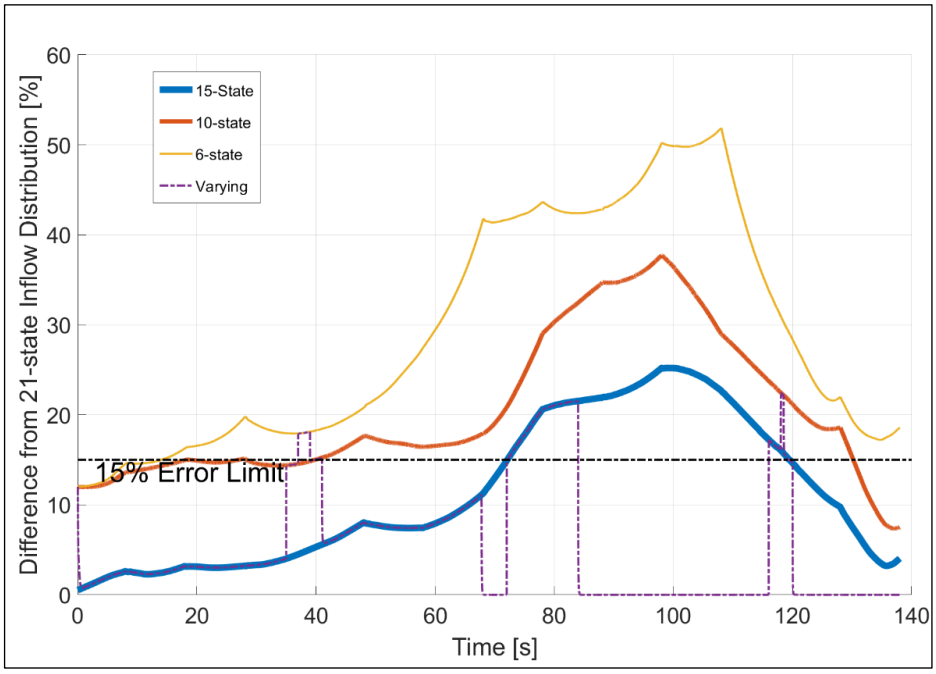

Figure 6.10. Speed up test with varying state inflow model

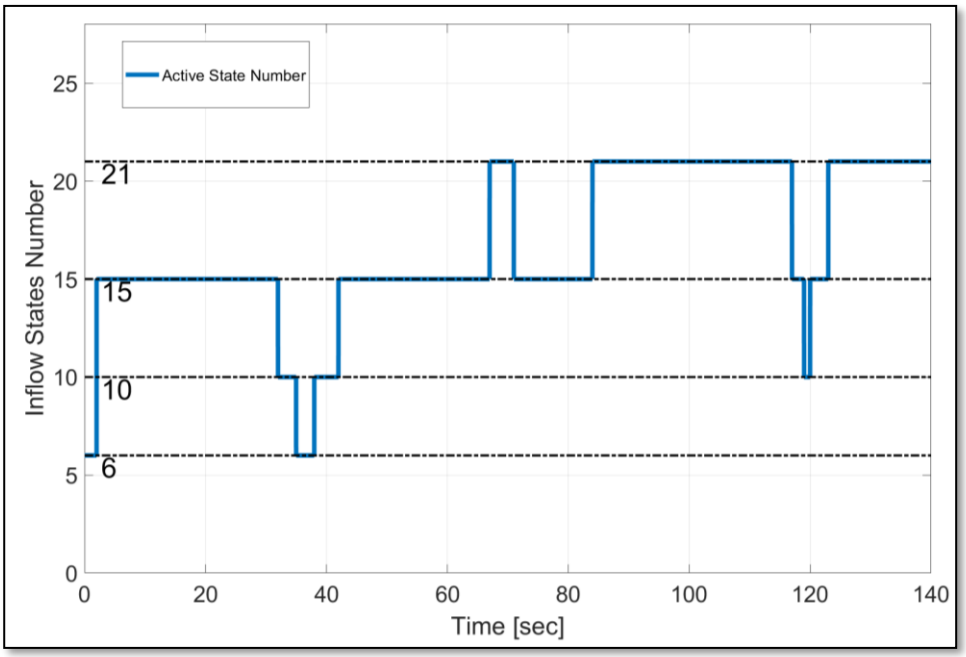

Figure 6.11. Active State Number

When the limits determined in the section 6.1 are applied, above figure is obtained for difference from 21-state inflow. At the peak of varying state difference line, it hits 23% difference at t=117 s. In the below figure, mean error vs. execution time is presented.

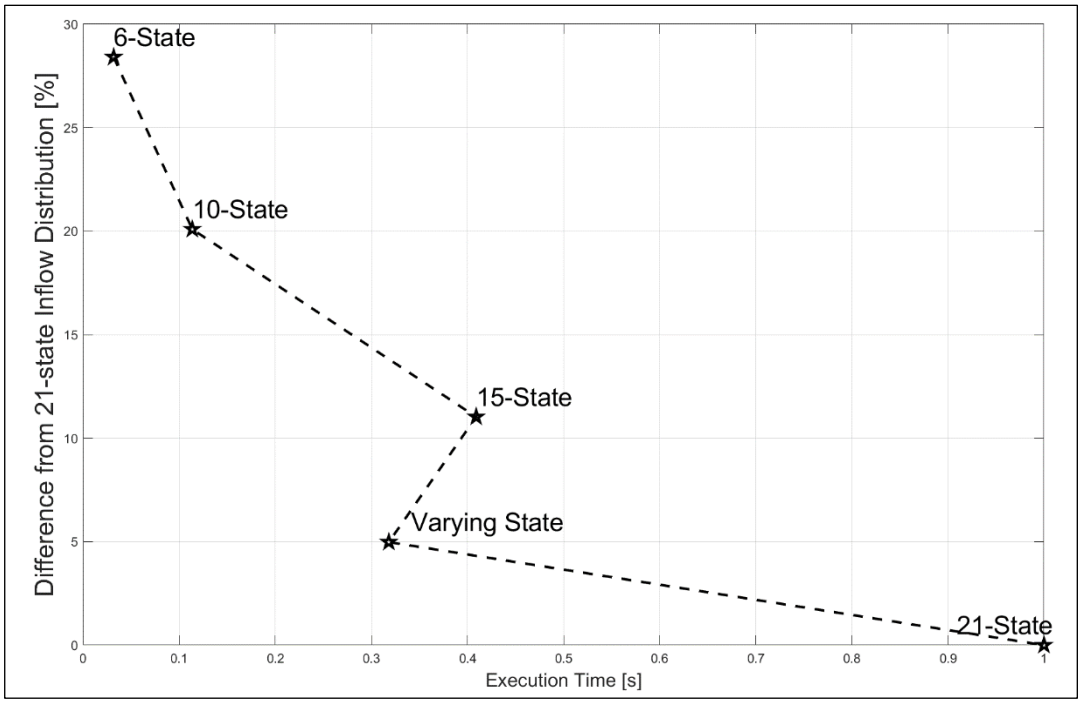

Figure 6.12. Mean Error vs. Non-dimensional Execution Time (Speed Up)

The varying-state inflow model run faster and with lower-errors with respect to 15-state inflow model.

6.2.5.2. Decreasing Advance Ratio Simulation

In this section, a 140-second-long speed down simulation is run. Advance ratio and collective and cyclic inputs are given in below figures.

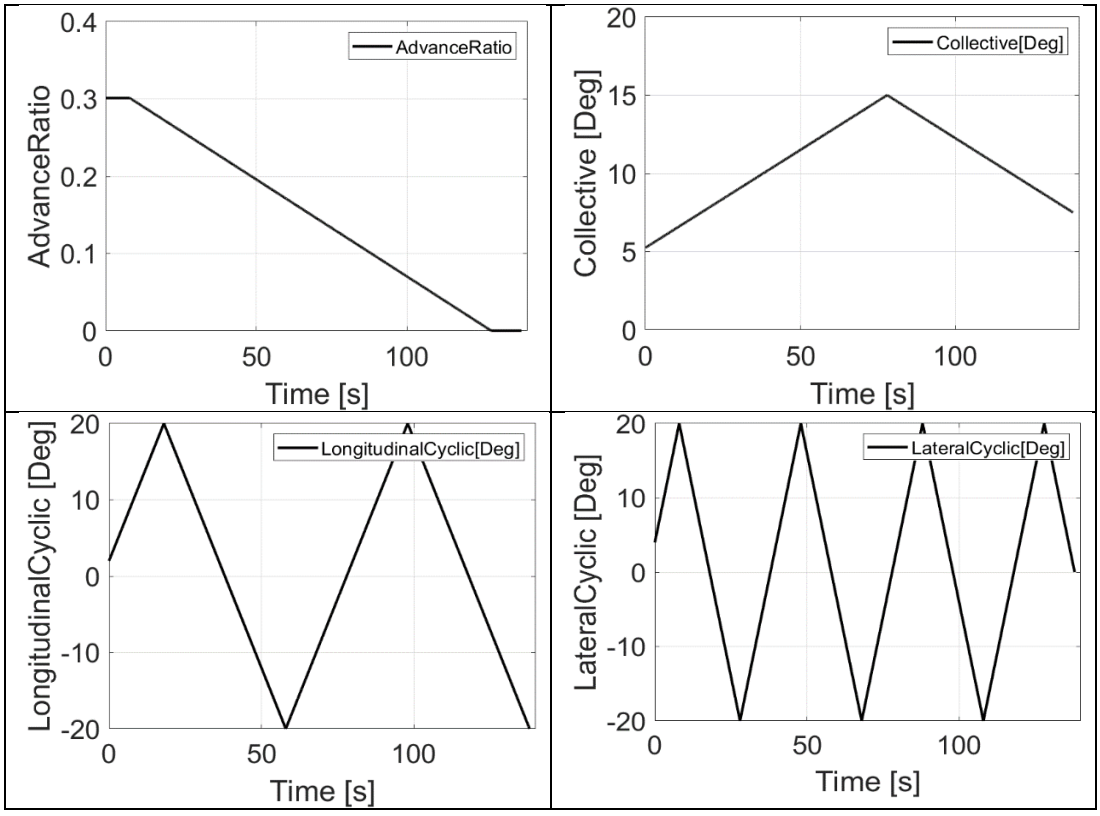

Figure 6.13. Speed Down Test Inputs

The varying-state inflow model run faster and with lower-errors with respect to 15-state inflow model. For this simulation the difference from 21-state inflow distribution figure is obtained as follows:

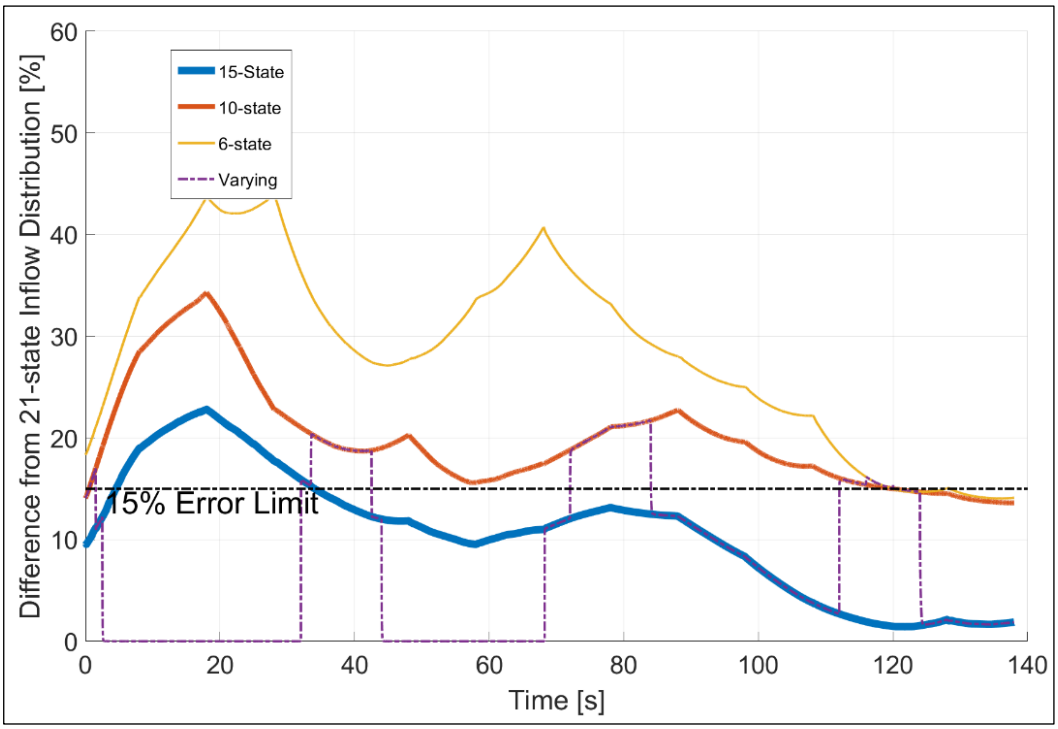

Figure 6.14. Speed Down test with varying state inflow model (Speed Down)

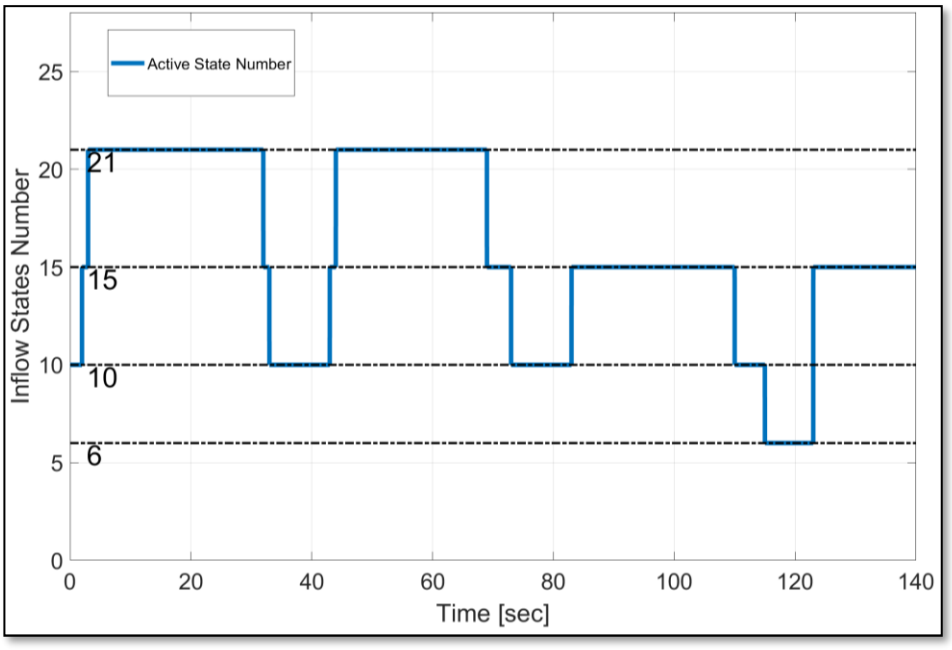

Figure 6.15. Active State Number

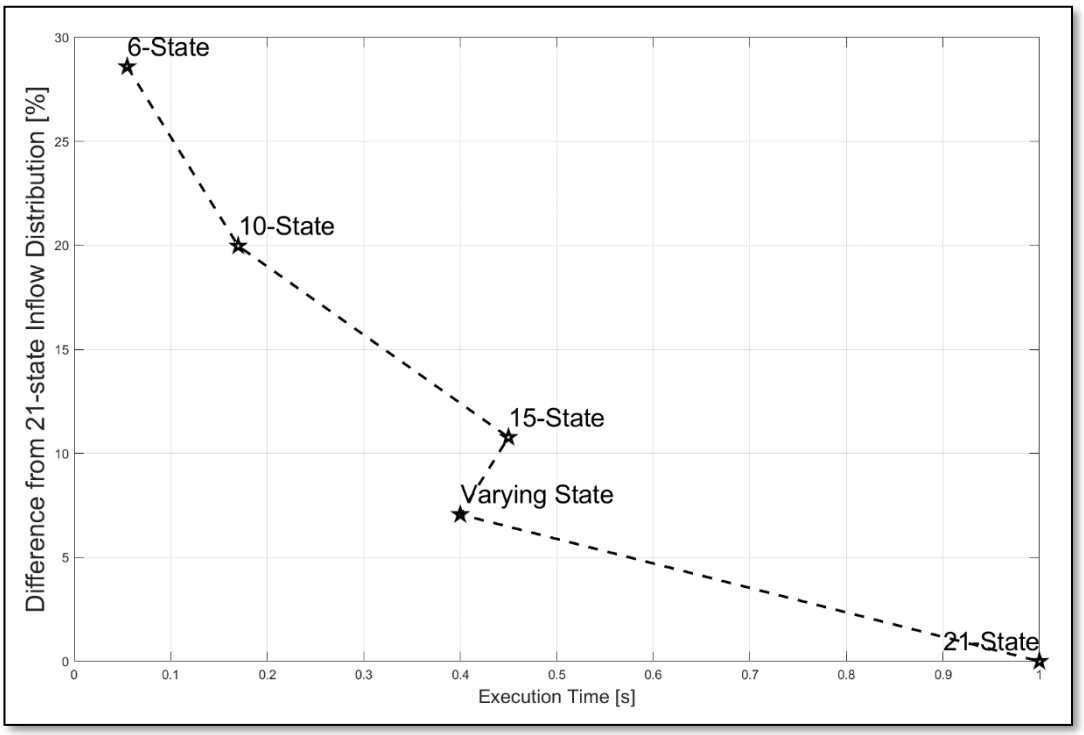

Figure 6.16. Mean Error vs. Non-dimensional Execution Time (Speed Down)

6.2.5.3. Observations for Rectangular Cyclic Limits

In the above simulations, the error limits in the long tests are exceeded the intended limit of 15% error. There are two main reasons for such results. First one is that, the combination of longitudinal and lateral cyclic are resulted higher deviations from 21-state model, even both cyclic inputs are below the limitations. Second one is that the input combinations are not appropriate representations of real-life input. Therefore, following solutions are suggested to solve these problems, using elliptical limits for cyclic in order to change the active inflow states and using sinusoidal inputs for long tests.

6.3. Ellipsoidal Cyclic Limits

The cyclic limits presented in the sections 6.2.1, 6.2.2, 6.2.3 and 6.2.4 are the limits of cyclic for state-switching mechanism. These limits are computed by using isolated inputs for the given channel. For example, in order to determine the deviation from 21-state inflow with respect to changing longitudinal cyclic, only longitudinal cyclic input is applied. However, this reduce the performance of model when combinations of lateral and longitudinal cyclic inputs are applied to the model. Therefore, these limits are converted into ellipsoidal limits which are given in the following figures. Note that the collective limits are same with section 6.2.

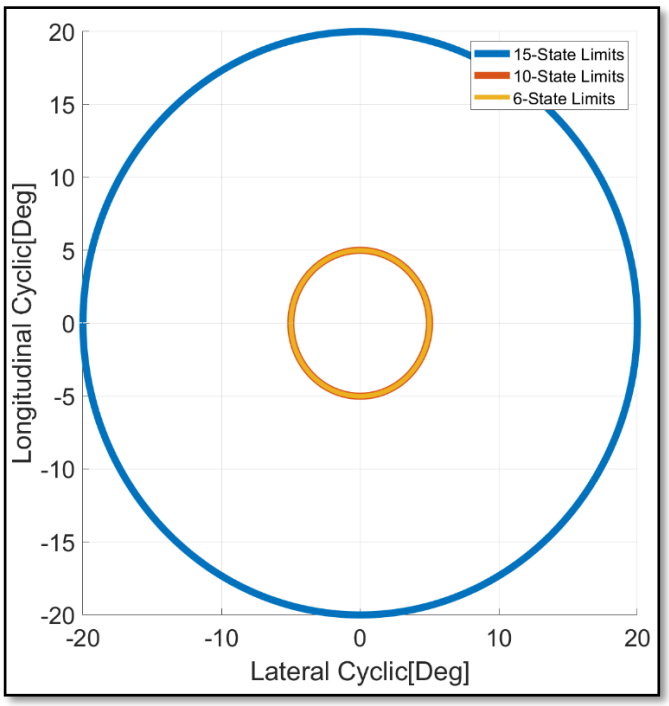

Figure 6.17. Cyclic limits at zero advance ratio

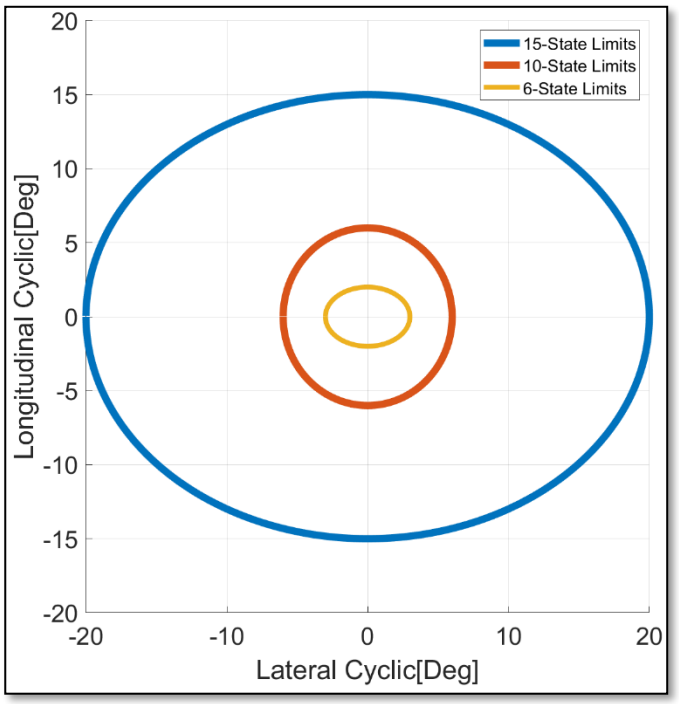

Figure 6.18. Cyclic limits at 0.1 advance ratio

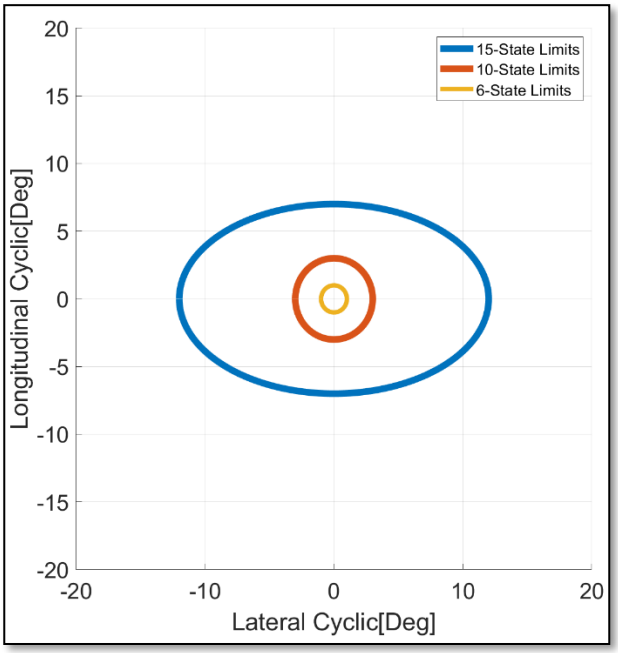

Figure 6.19. Cyclic limits at 0.2 advance ratio

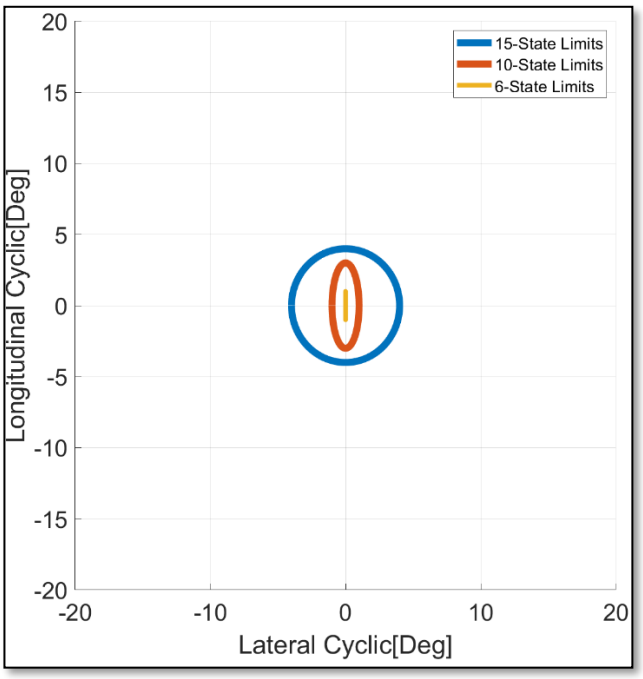

Figure 6.20. Cyclic limits at 0.3 advance ratio

6.3.1. Increasing Advance Ratio with Ellipsoid Cyclic Limits

In this section, a 140-second-long increasing-advance-ratio simulation is run. Advance ratio and collective and cyclic inputs are given in below figures.

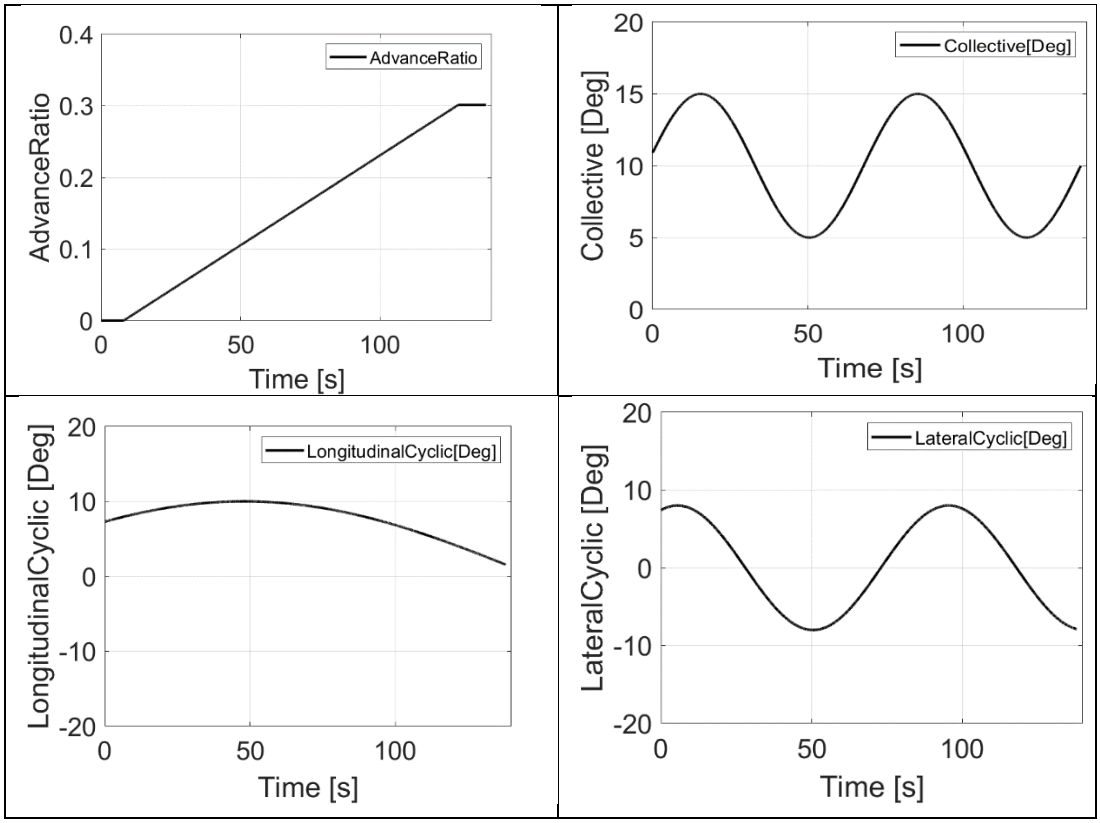

Figure 6.21. Increasing-Advance-Ratio Test Inputs

When the limits in section 6.3 are applied in a test where the advance ratio is increased gradually with the given collective and cyclic inputs in Figure 6.21 the following figure is obtained.

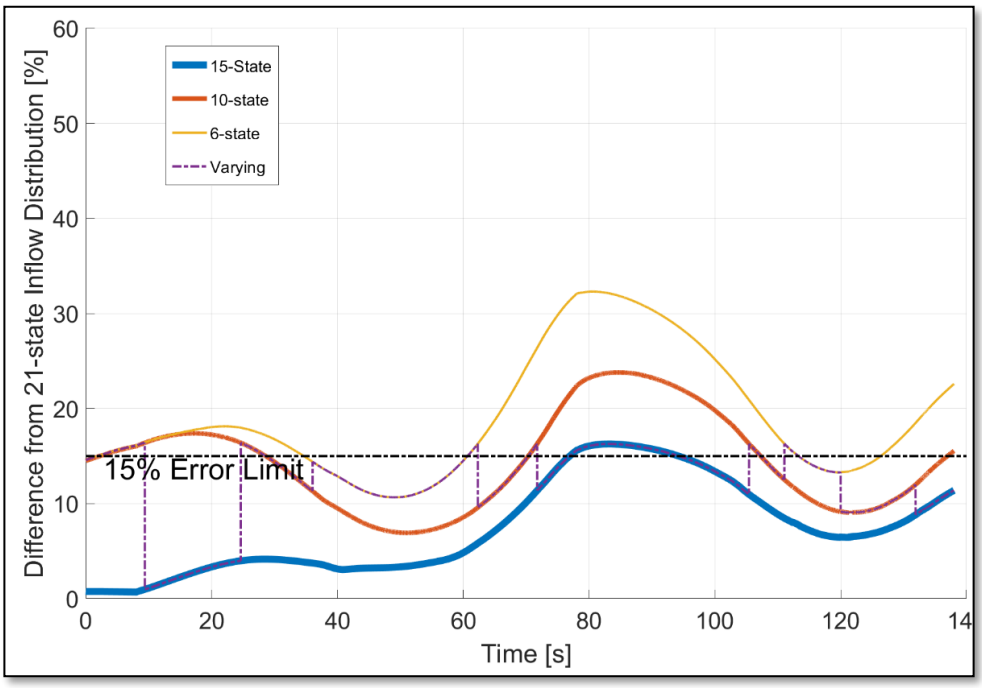

Figure 6.22. Increasing-advance-ratio test with varying state inflow model

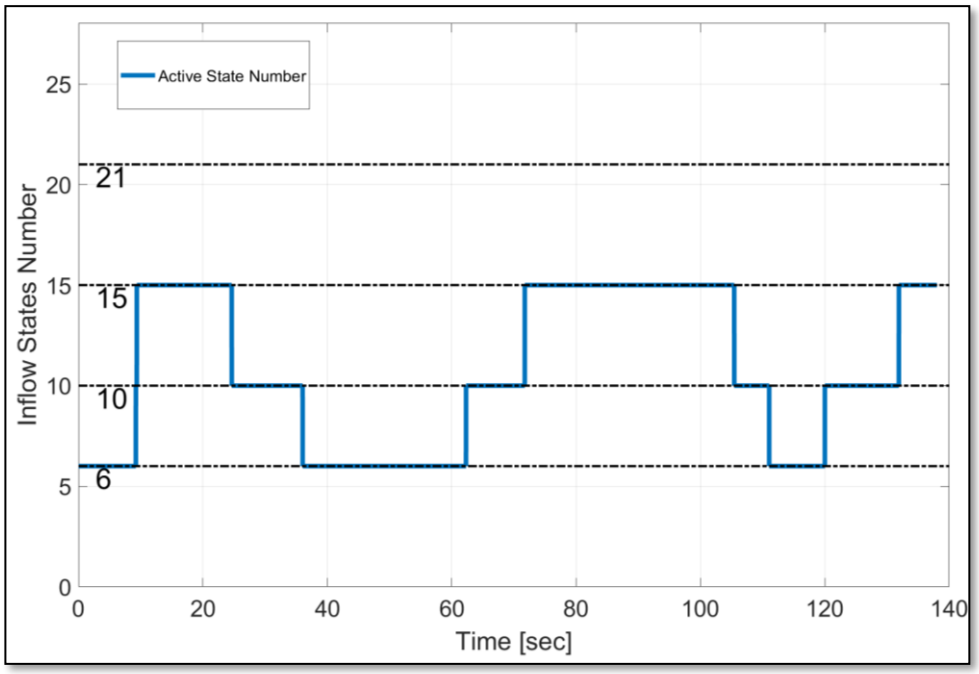

Figure 6.23. Active State Number

Using the ellipsoidal cyclic limits to switch between states keep the error limits almost at required levels at 15%. In addition, in this simulation the inputs are given as sinusoidal to be a better representation of real time applications. This resulted in a fewer discrete events in the switching mechanism.

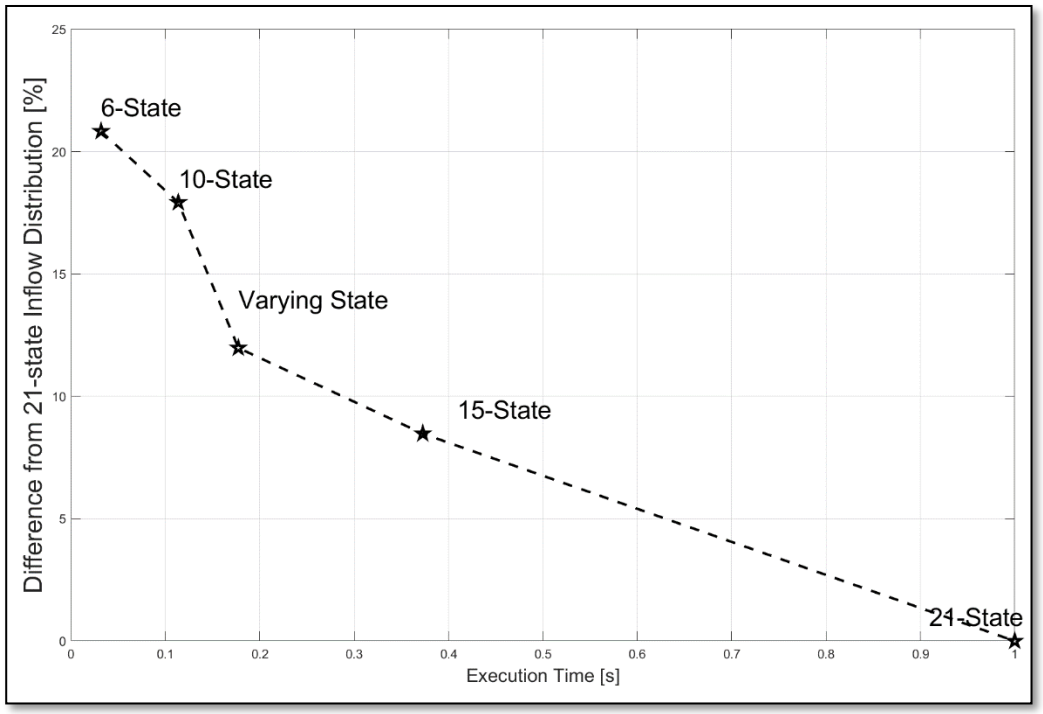

Figure 6.24. Mean Deviation vs. Non-Dimensional Execution Time

6.3.2. Decreasing Advance Ratio with Ellipsoid Cyclic Limits

In this section, a 140-second-long decreasing-advance-ratio simulation is run. Advance ratio and collective and cyclic inputs are given in below figures.

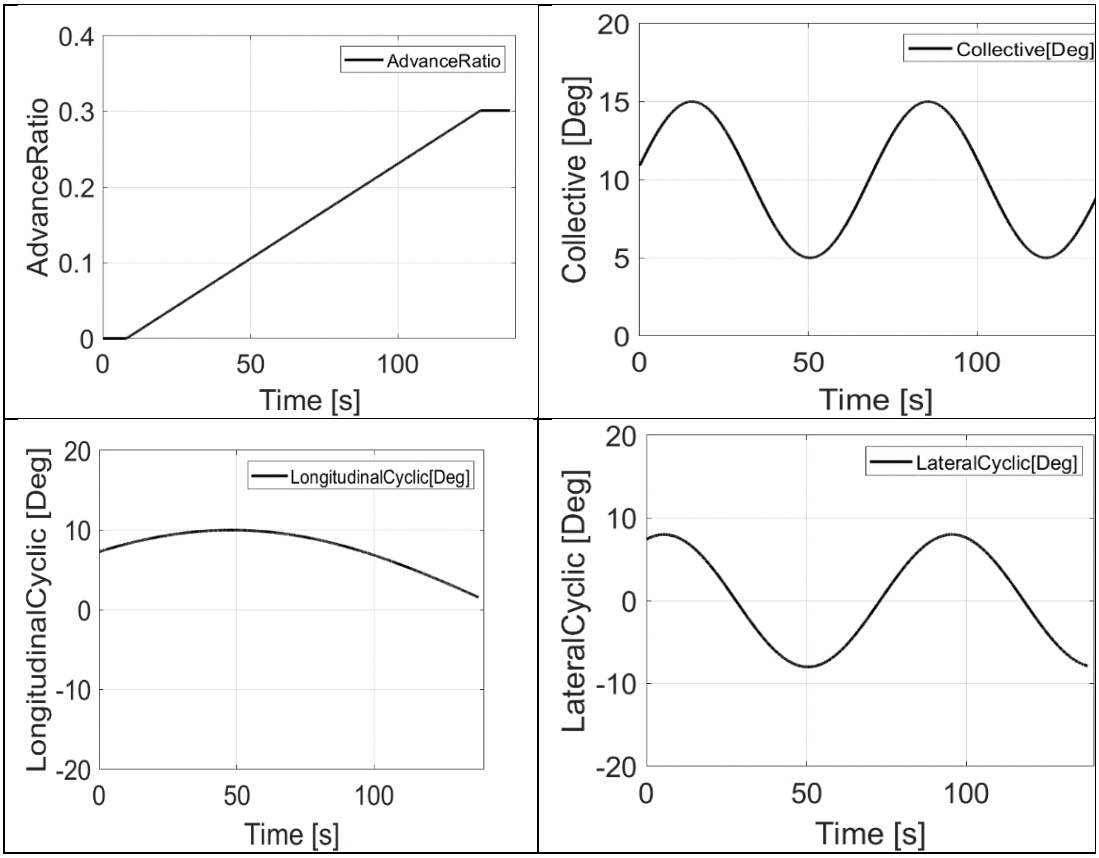

Figure 6.25. Decreasing-Advance-Ratio Test Inputs

When the limits in section 6.3 are applied in a test where the advance ratio is decreased gradually with the given collective and cyclic inputs in Figure 6.25 the following figure is obtained.

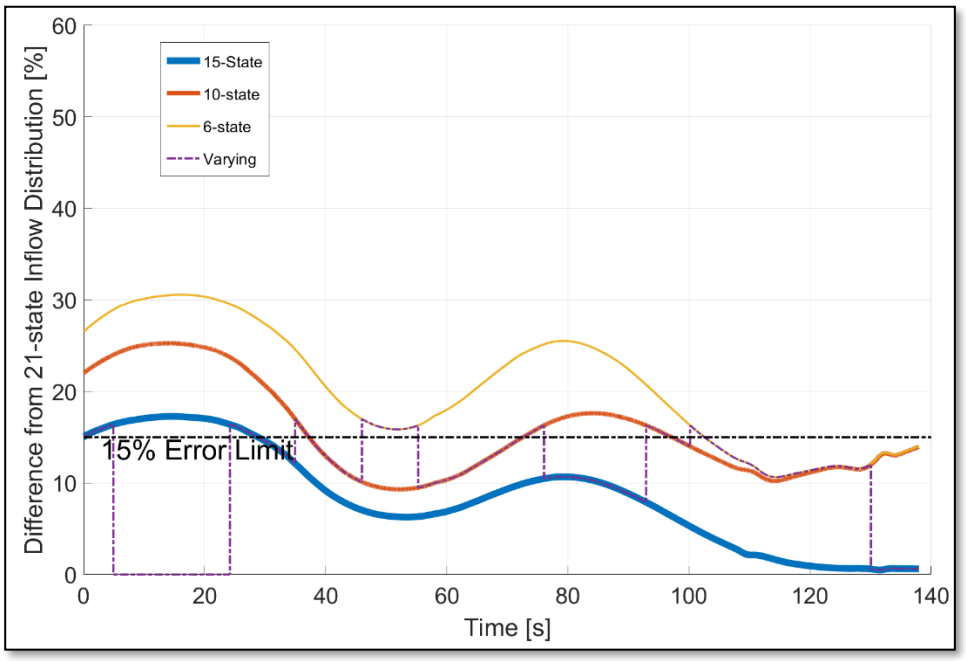

Figure 6.26. Decreasing-advance-ratio test with varying state inflow model

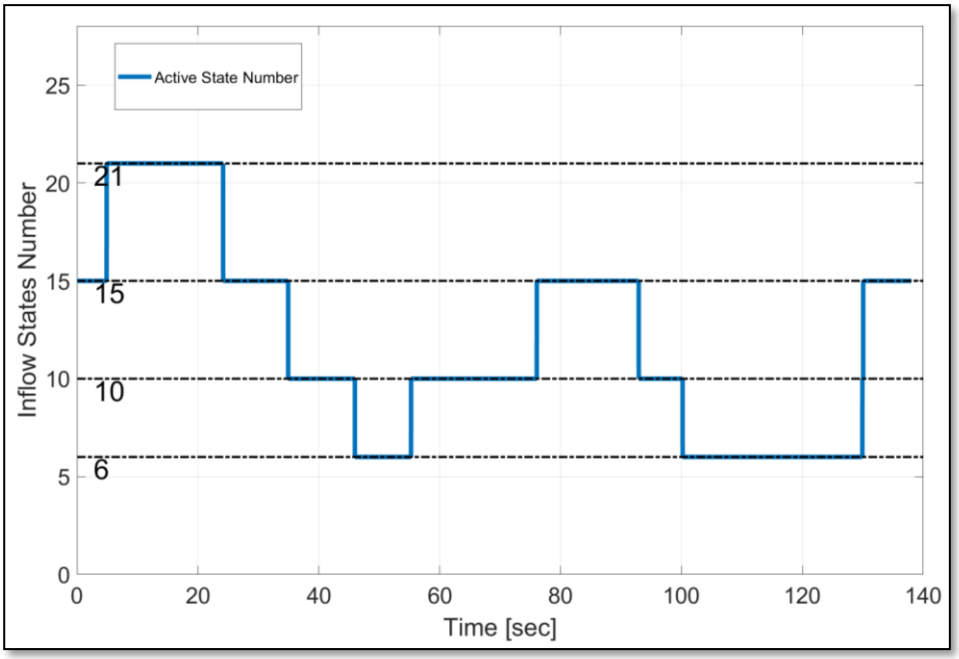

Figure 6.27. Active State Number

Using the ellipsoidal cyclic limits allow the varying state model to perform below the 15% deviation range. The following graph shows the mean deviation vs. execution time.

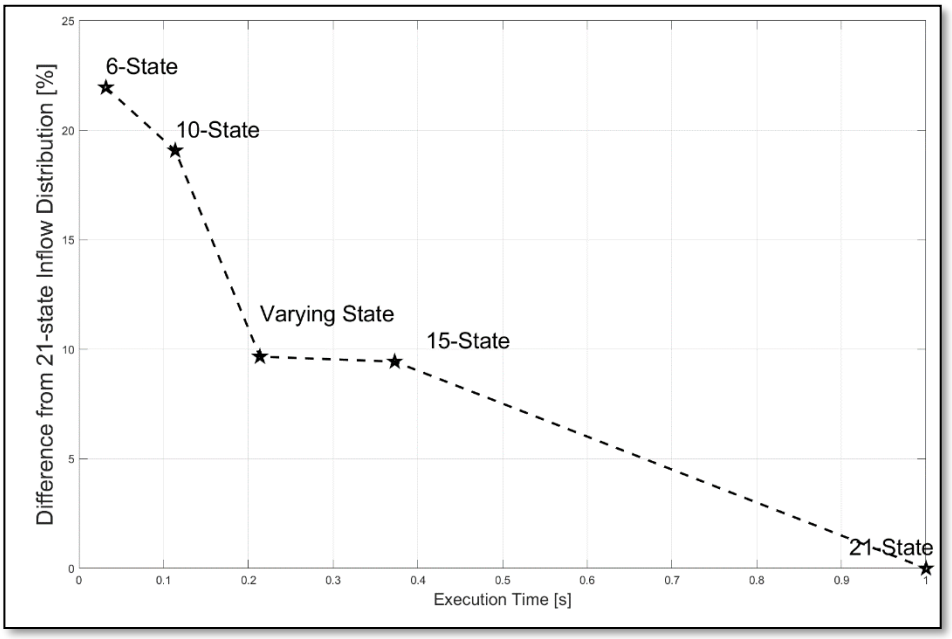

Figure 6.28. Mean Deviation vs. Non-Dimensional Execution Time

CHAPTER 7

CONCLUSIONS

7.1. Summary

The modeling of the inflow dynamics of a rotorcraft has been an important topic. There are well-established non-uniform inflow theories in the literature mainly divided into static and dynamic inflow. In the literature survey section, the studies on inflow theories are presented. All dynamic inflow theories that presented have fixed number of dynamic states throughout its simulation. In this thesis a new method to compute dynamic inflow is proposed that the dynamic inflow states are changed in run-time with respect to the changing conditions. The effects of advance ratio and pilot inputs are investigated to determine conditions in which the selected number of state inflow model operates without deviating from higher number state models.

7.2. Observations

In this thesis, the effects of inflow state number in Peters – He inflow models are investigated for various advance ratio and control input configurations. Throughout Chapter 2 and Chapter 3 a rigorous explanation for analytical background of the theory and a clear procedure to implement Peters – He inflow model are aimed. In Chapter 4, the method for implementing varying state model with the lift theory is explained using a rotor model. In Chapter 5, the model is used to determine the difference between 21-State, 15-State, 10-State and 6-State inflow model distributions. These differences are used to create a logic to switch between state-numbers when implementing the varying state inflow model. From these analyses, following conclusions are obtained.

- The advance ratio is the most dominant parameters which affects the inflow distributions between 6, 10, 15, and 21 state dynamic inflow models. As the advance ratio is increased, the lateral distribution on actuator disc becomes more asymmetrical. The low-state inflow models lack the required states which represents the lateral distribution.

- In hover and without cyclic inputs, the difference between models are mostly negligible. However, when cyclic inputs are applied, there exist distribution differences between inflow models. The main observation related to this issue is that 6-state and 10-state models are identical whereas 15-state and 21-state are identical.

- The magnitude of the input directly correlates with the difference between inflow models with different state numbers.

- The response of the inflow differences of 6, 10,15 state models from 21 state model with lateral or longitudinal cyclic inputs are similar. Especially during hover, the responses to longitudinal and lateral cyclic inputs are same. However, as advance ratio is increased, the sensitivity to lateral cyclic between different-number-state models are increased, due to the already existing lateral asymmetry with respect to non-zero advance ratio.

- The high number of inflow states implies significantly higher computation costs due the matrix inversion made in the inflow calculations. Calculation of 21 state inflow model took 20 times more time that 6-state. The 28-state inflow model is unable to compute real-time at 100 Hz. Therefore, 28 and higher states are excluded in this thesis.

- ❖ In the Speed Up and Speed Down tests run in Chapter 6, variable-state inflow model is run faster and with lower-error than 15 state model. However, one should assess the benefits of a variable-state inflow model instead of 15-state model considering the implementation effort involved in variable-state inflow model.
- ❖ The rectangular limits for cyclic given in Chapter 6 were unable to keep the deviation below 15% when the lateral and longitudinal cyclics are applied simultaneously. Therefore, the limits are mapped as ellipses. In addition, the triangle wave inputs are not proper representations of cyclic commands given by actual pilot to a rotor. Thus, sinusoidal input tests are made. Those tests show that using varying-number state method reduced the computation time significantly in mild conditions.

7.3. Recommendations for Future Work

There are possible recommendations to improve the varying-state inflow model. These recommendations can be listed as follows:

1. The angular rates (p, q, r) of the rotor can be incorporated into the state number selection logic.
2. The entry and exit of an inflow state can be filtered to reduce discrete events.
3. This inflow model can be tested with different rotor configurations.
4. The difference between higher number of inflow states can be investigated.
5. Varying-state dynamic inflow model can be integrated to a full helicopter simulation to assess its fidelity.

REFERENCES

[1] Banerjee, D., Crews, S. T., & Hohenemser, K. H. (1979). Parameter Identification Applied to Analytic Hingeless Rotor Modeling. *Journal of the American Helicopter Society*, *24*(1).

[2] Banerjee, D., Crews, S. T., Hohenemser, K. H., & Yin, S. K. (1977). *Identification of state variables and dynamic inflow from rotor model dynamic tests*.

[3] Bhagwat, M. J., & Leishman, J. G. (2001). Transient Rotor Inflow Using a Time-Accurate Free-Vortex Wake Model. *39th AIAA Aerospace Sciences Meeting & Exhibit*, (January).

[4] Bramwell, A. R. ., Done, G., & Balmford, D. (2001). *Bramwell ' s Helicopter Dynamics*.

[5] Brotherhood, P. (1947). An Investigation in Flight of Induced Velocity Distribution Under a Helicopter Rotor When Hovering. *ARC RAE Report No. Aero2212*.

[6] Brown, R. E., & Houston, S. S. (2000). Comparison of induced velocity models for helicopter flight mechanics. *Journal of Aircraft*, *37*(4), 623–629. https://doi.org/10.2514/2.2644

[7] Chen, R. T. N. (1990). A survey of nonuniform inflow models for rotorcraft flight dynamics and control applications. *Nasa Technical Memorandum*, *14*(2), 147–184.

[8] Coleman, R. P., Feingold, A. M., & Stempin, C. W. (1945). Evaluation of the induced velocity field of an idealized helicopter rotor. *Naca Arr. No. L5E10*.

[9] Curtiss, H. C., & Shupe, N. K. (1971). A Stability and Control Theory for Hingeless Rotors. *Proceedings of the 27th Anmual Natial Forum of the American Helicopter Society*. Washington, D.C.

[10] Drees, J. M. J. (1949). A Theory of Airflow Through Rotors and its application to Some Helicopter Problems. *Helicopter Assoc. Great Britain*, *3*(2).

[11] Gaonkar, G. H., & Peters, D. A. (1986). Review of Dynamic Inflow Modeling for Rotorcraft Flight Dynamics. *Collection of Technical Papers - AIAA/ASME/ASCE/AHS/ASC Structures, Structural Dynamics and Materials Conference*, (pt 2), 89–115.

[12] Glauert, H. (1922). *An Aerodynamic Theory of the Airscrew*. Retrieved from https://books.google.com.tr/books?id=mDgHtwAACAAJ

[13] Glauert, H. (1926). A General Theory of the Autogyro. *Scientific Research Air Ministry - Reports and Memoranda No. 1111*, 41.

[14] Güner, F. (2016). *Comparison of Rotor Inflow Models for Flight Simulation*. Middle East Technical University.

[15] Guner, F., Gursoy, G., & Yavrucuk, I. (2016). Performance evaluation and comparison of dynamic inflow models for rotorcraft simulation. *Annual Forum Proceedings - AHS International*, *3*, 2441–2462.

[16] Gürler, M. (2018). *MATHEMATICAL MODELING OF A SMALL-SCALE HELICOPTER AND MRAC DESIGN WITH TIME BASED UNCERTAINTY PARAMETRIZATIONS*. Middle East Technical University.

[17] Harris, F. D. (2009). Articulated Rotor Blade Flapping Motion at Low Advance Ratio. *Journal of the American Helicopter Society*, *17*(2), 46–46. https://doi.org/10.4050/jahs.17.46

[18] Harris, F. D., & McVeigh, M. A. (1976). Uniform Downwash With Rotors Having a Finite Number of Blades. *Journal of the American Helicopter Society*, *21*(1), 9–20.

[19] He, C. J. (1989). *Development and application of a generalized dynamic wake theory for lifting rotors*. Georgia Institute of Technology.

[20] Houston, S. S. (2002). Analysis of rotorcraft flight dynamics in autorotation. *Journal of Guidance, Control, and Dynamics*, *25*(1), 33–39. https://doi.org/10.2514/2.4872

[21] Houston, S. S., & Tarttelin, P. C. (1991). Validation of mathematical simulations of helicopter vertical response characteristics in hover. *Journal of the American Helicopter Society*, *36*(1), 45–57.

[22] Howlett, J. J. (1981). *Black Hawk Engineering Simulation Program*. *1*.

[23] Jepson, D., Moffitt, R., Hilzinger, K., & Bissel, J. (1983). Analysis and Correlation of Test Data From an Advanced Technology Rotor System. *NASA Contractor Reports*, (August).

[24] Johnson, W. (1980). Helicopter Theory. In *Helicopter Theory*. https://doi.org/10.1108/eb030686

[25] Kitaplioglu, C. (1990). *Analysis of Small-Scale Rotor Hover Performance Data*. *0772346*.

[26] Leishman, J. G. (2006). *Principles of Helicopter* (Second). Cambridge University Press.

[27] Mangler, K. W., & Squire, H. B. (1953). *The Induced Velocity Field of a Rotor* (Vol. 2642). Vol. 2642. Ministry of Supply, Aeronautical Research Council Reports and Memoranda.

[28] Murakami, Y., & Houston, S. S. (2008). Dynamic inflow modelling for autorotating rotors. *Aeronautical Journal*, *112*(1127), 47–53. https://doi.org/10.1017/S0001924000001986

[29] Murakami, Yoh. (2008). *A New Appreciation of Inflow Modelling for Autorotative Rotors*. University of Glasgow.

[30] Nagle, R. K., B. Saff, E., & David Snider, A. (2012). *Fundamentals of DifferentialEquations* (eighth).

[31] Ormiston, R. A., & Peters, D. A. (1972). Hingeless helicopter rotor response with nonuniform inflow and elastic blade bending. *Journal of Aircraft*, *9*(10), 730–736. https://doi.org/10.2514/3.59070

[32] Padfield, G. D. (2018). Helicopter Flight Dynamics. In *Helicopter Flight Dynamics*. https://doi.org/10.1002/9781119401087

[33] Payne, P. R. (1959). *Helicopter Dynamics and Aerodynamics*. Pitman.

[34] Peters, D. A. (n.d.). *Momentum Theory, Dynamic Inflow, and the Vortex-Ring State*.

[35] Peters, D. A., Boyd, D. D., & He, C. J. (1989). Finite-state induced-flow model for rotors in hover and forward flight. *Journal of the American Helicopter Society*, *34*(4), 5–17. https://doi.org/10.4050/JAHS.34.5

[36] Peters, D. A., Karunamoorthy, S., & Cao, W. M. (1995). Finite state induced flow models. Part I: Two-dimensional thin airfoil. *Journal of Aircraft*, *32*(2), 313–322. https://doi.org/10.2514/3.46718

[37] Peters, D. A., & Ninh, H. (1988). Dynamic inflow for practical applications. *Journal of the American Helicopter Society*, *33*(4), 64–68.

[38] Pitt, D. M. (1980). *Rotor Dynamic Inflow Derivatives and Time-constants from various models*. Washington University Sever Institute of Technology.

[39] Pitt, D. M., & Peters, D. A. (1980). *Theoretical Prediction of Dynamic-Inflow Derivatives*. (47).

[40] Prouty, R. W. (2002). *Helicopter Performance, Stability and Control* (Reprint). Krieger Publishing Company.

[41] Shinoda, P. M., & Johnson, W. (1993). Performance Results from a Test of an S-76 Rotor in the NASA Ames 80 by 120 Foot Wind Tunnel. *AIAA-93-3414-CP*.

[42] Sissingh, G. (1951). The Effect of Induced Velocity Variation on Helicopter Rotor Damping in Pitch or Roll. *Aeronautical Research Council Technical Report*, (101).

[43] Van Hoydonck, W. R. M., Haverdings, H., & Pavel, M. D. (2009). A review of rotorcraft wake modeling methods for flight dynamics applications. *35th European Rotorcraft Forum 2009, ERF 2009*, *1*, 27–53.

[44] Von Kinner, W. (1936). *Die kreisförmige tragflache auf potentialtheoretıscher Grundlage*. *5*(1925).

[45] Wheatley, J. (1934). An aerodynamic analysis of the autogiro with a comparison between calculated and experimental results. *NACA Report No. 487*.

[46] White, F., & Blake, B. B. (1979). Improved Method Of Predicting Helicopter Control Response And Gust Sensitivity. *Boeing Vertol Co.*

[47] Wood, E. R., & Hermes, M. E. (1969). Rotor Induced Velocities in Forward Flight by Momentum Theory. *AIAA/AHS Vtol Research, Design, and Operations Meeting*, (69).

[48] Zhao, J. (2005). *Dynamic Wake Distortion Model For Helicopter Maneuvering Flight*. Georgia Institute of Technology.

APPENDICES

A. ELLIPSOIDAL COORDINATE SYSTEM

Ellipsoidal coordinates (v, ψ, η) are defined by (x, y, z) as follows:

$$x = -\sqrt{1+\eta^2}\sqrt{1-v^2}\cos(\psi) \tag{A.1}$$

$$y = \sqrt{1+\eta^2}\sqrt{1-v^2}\,sin(\psi) \tag{A.2}$$

$$z = -\eta v \tag{A.3}$$

The upper and lower surfaces of the rotor is given as:

$$v < 0 : z > 0, \text{ lower surface} \tag{A.4}$$

$$v > 0 : z < 0, \text{ upper surface} \tag{A.5}$$

$$grad(\phi) = e_v\sqrt{\frac{1-v^2}{v^2+\eta^2}}\frac{\partial\Phi}{\partial v} + e_\psi\frac{1}{\sqrt{(1+\eta^2)(1-v^2)}}\frac{\partial\phi}{\partial\psi} + e_\eta\sqrt{\frac{1+\eta^2}{v^2+\eta^2}}\frac{\partial\Phi}{\partial\eta} \tag{A.6}$$

$$\begin{aligned} div(V) = \frac{1}{v^2+\eta^2}\Bigg[&\frac{\partial}{\partial v}\left(\sqrt{(1-v^2)(v^2+\eta^2)}\;V_1\right) \\ &+ \frac{\partial}{\partial\psi}\left(\frac{\eta^2+v^2}{\sqrt{(1+\eta^2)(1-v^2)}}V_2\right) \\ &+ \frac{\partial}{\partial\eta}\left(\sqrt{(v^2+\eta^2)(1+\eta^2)}\,V_3\right)\Bigg] \end{aligned} \tag{A.7}$$

$$\nabla(\phi) = \frac{1}{v^2+\eta^2}\left[\frac{\partial}{\partial v}(1-v^2)\left(\frac{\partial \phi}{\partial v}\right) + \frac{\partial}{\partial \psi}\left(\frac{v^2+\eta^2}{(1+\eta^2)(1-v^2)}\right)\left(\frac{\partial \phi}{\partial \psi}\right) + \frac{\partial}{\partial \eta}(1+\eta^2)\left(\frac{\partial \phi}{\partial \eta}\right)\right] \quad \text{(A.8)}$$

Where ϕ and $V = \{V_1, V_2, V_3\}$ are arbitrary scalar and vector functions respectively.

B. INFLOW DISTRIBUTION

In this section the lateral distribution of the inflow model is investigated at a given time t = 12 for Chapter 5.

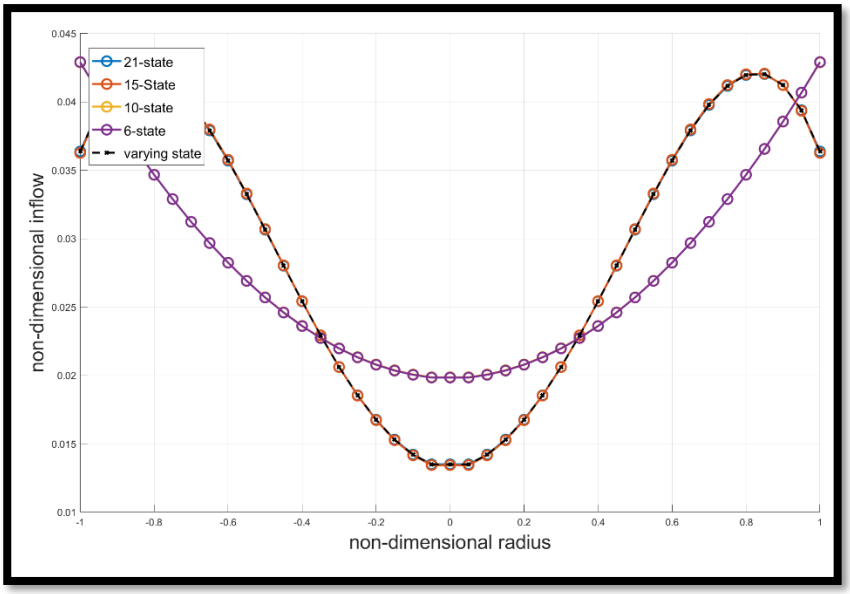

Figure B.1. $\mu = 0.0,\ \theta_0 = 20°, \theta_{1c} = 0°, \theta_{1s} = 0°$,azimuth

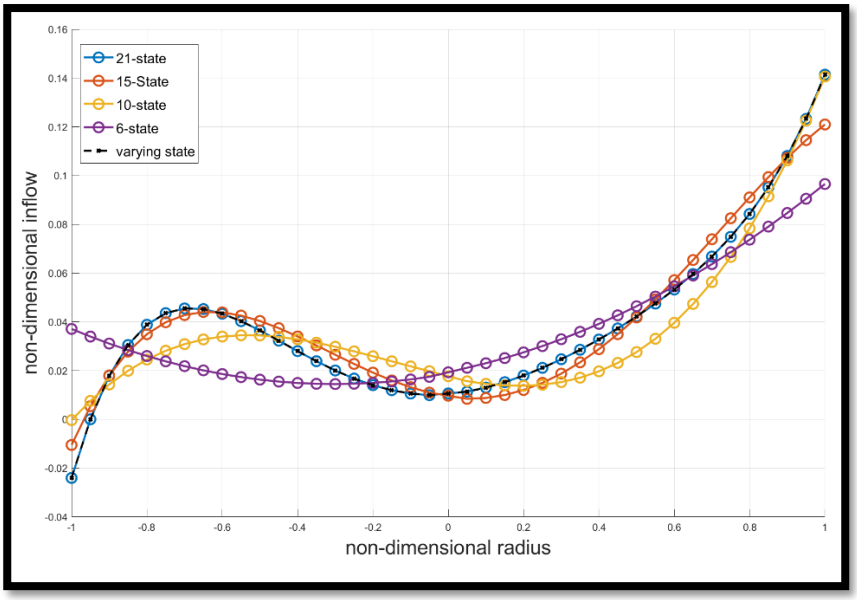

Figure B.2. $\mu = 0.1,\ \theta_0 = 20°, \theta_{1c} = 0°, \theta_{1s} = 0°$

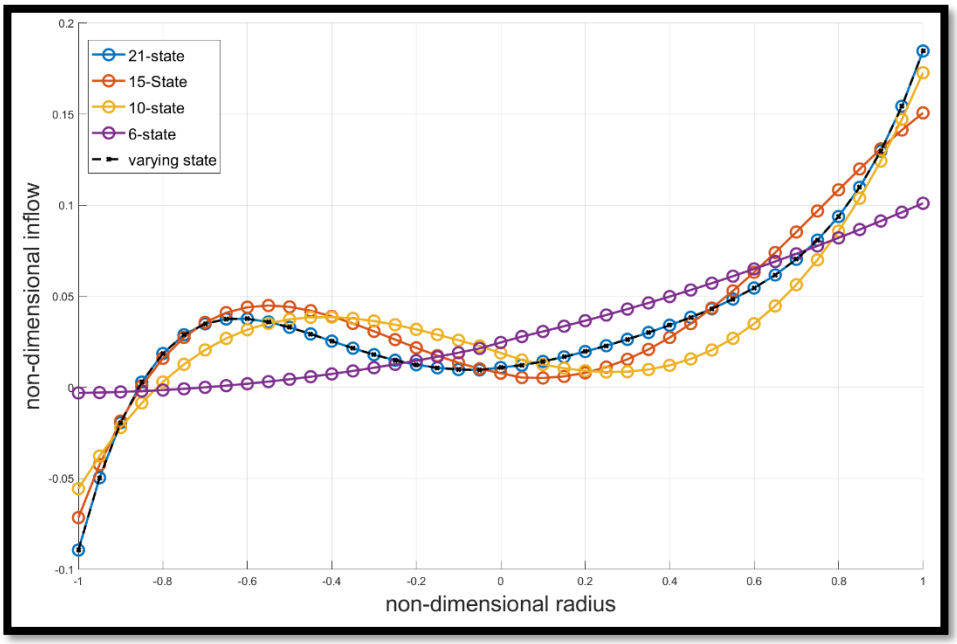

Figure B.3. $\mu = 0.2,\ \theta_0 = 20°, \theta_{1c} = 0°, \theta_{1s} = 0°$

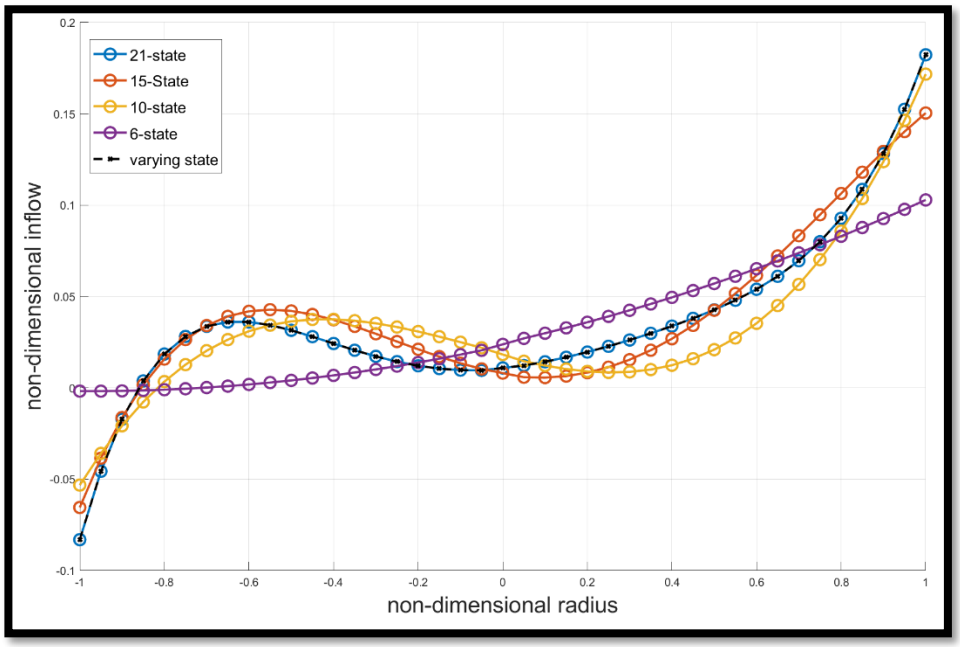

Figure B.4. $\mu = 0.3,\ \theta_0 = 20°, \theta_{1c} = 0°, \theta_{1s} = 0°$

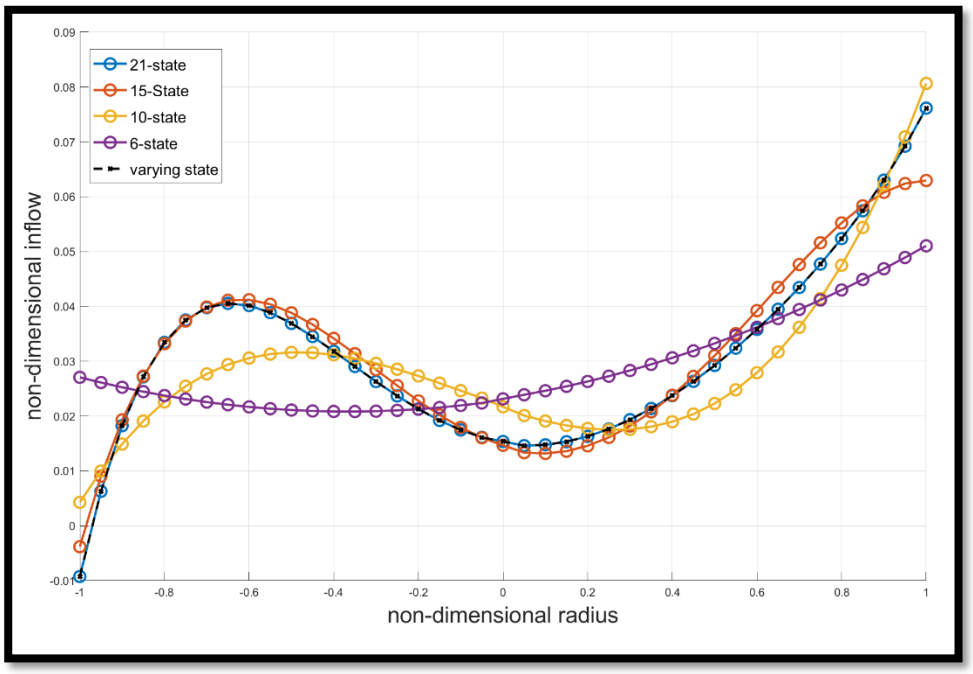

Figure B.5. $\mu = 0.1,\ \theta_0 = 8°, \theta_{1c} = 0°, \theta_{1s} = 20°$

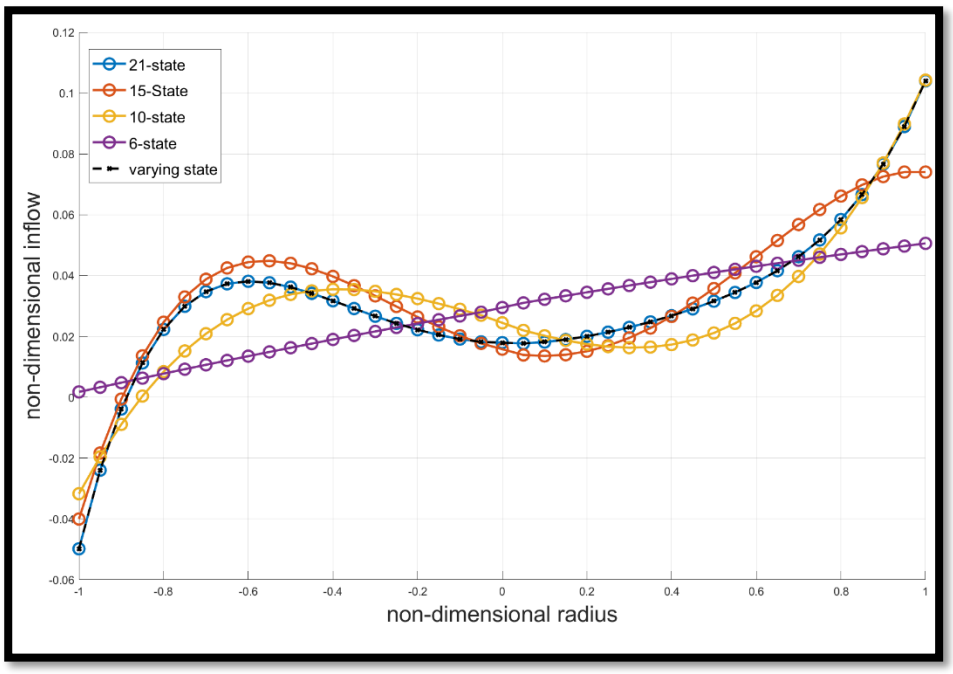

Figure B.6. $\mu = 0.2,\ \theta_0 = 8°, \theta_{1c} = 0°, \theta_{1s} = 20°$

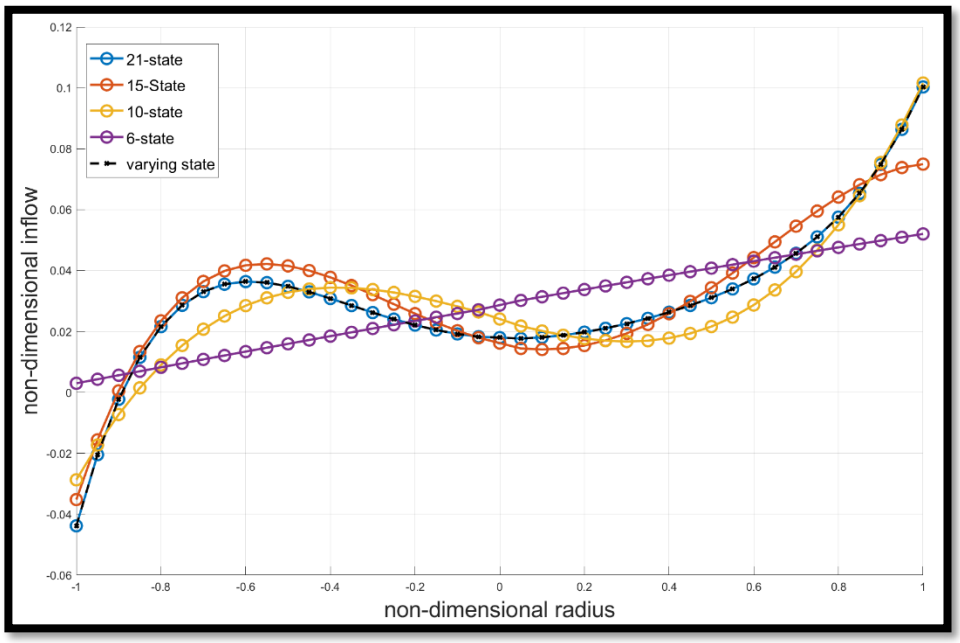

Figure B.7. $\mu = 0.3,\ \theta_0 = 8°, \theta_{1c} = 0°, \theta_{1s} = 20°$

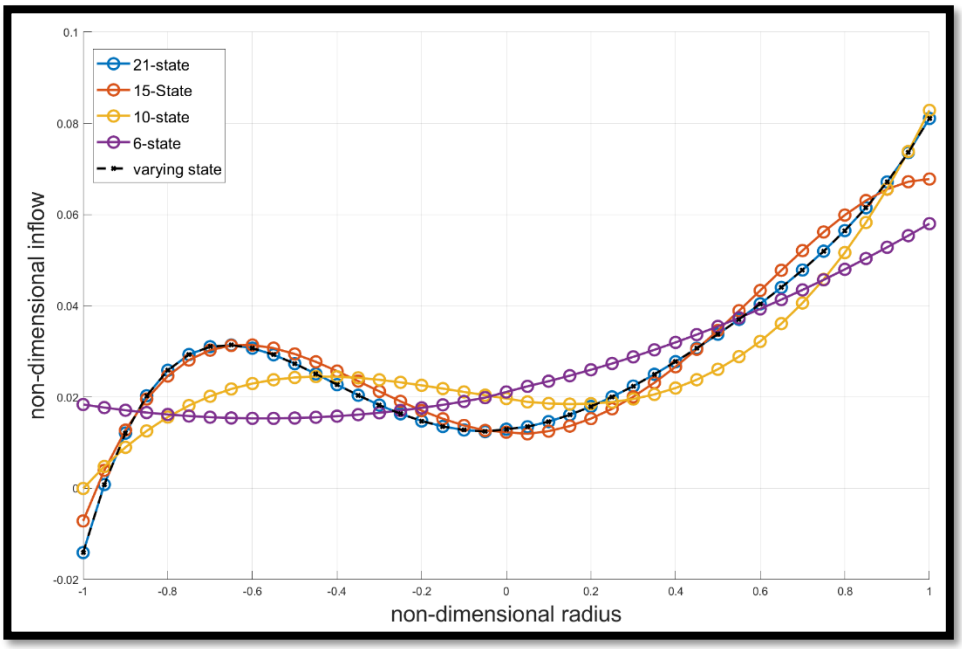

Figure B.8. $\mu = 0.1,\ \theta_0 = 8°, \theta_{1c} = 20°, \theta_{1s} = 0°$

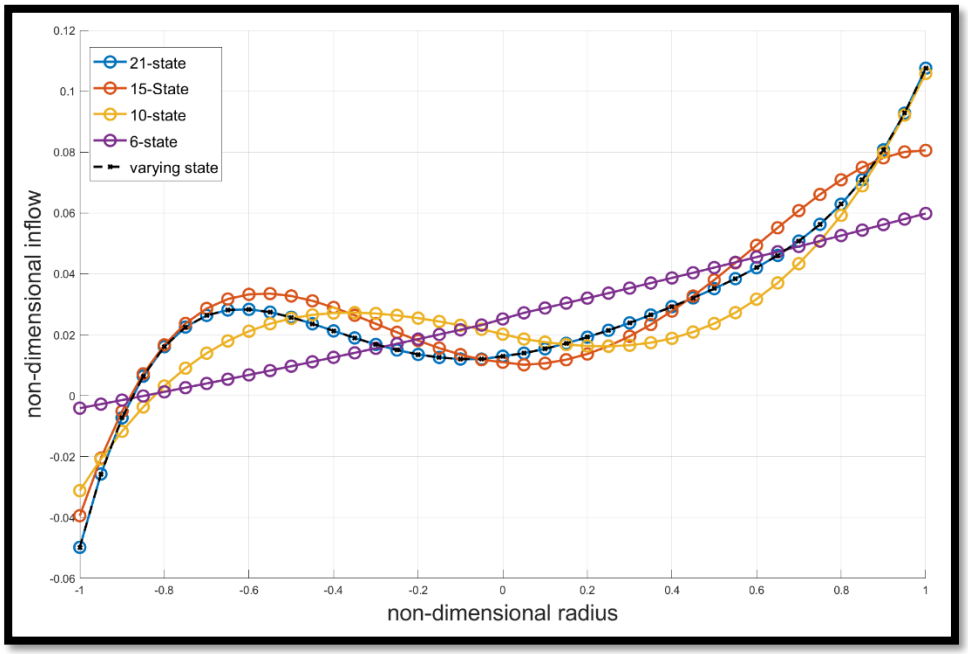

Figure B.9. $\mu = 0.2,\ \theta_0 = 8°, \theta_{1c} = 20°, \theta_{1s} = 0°$

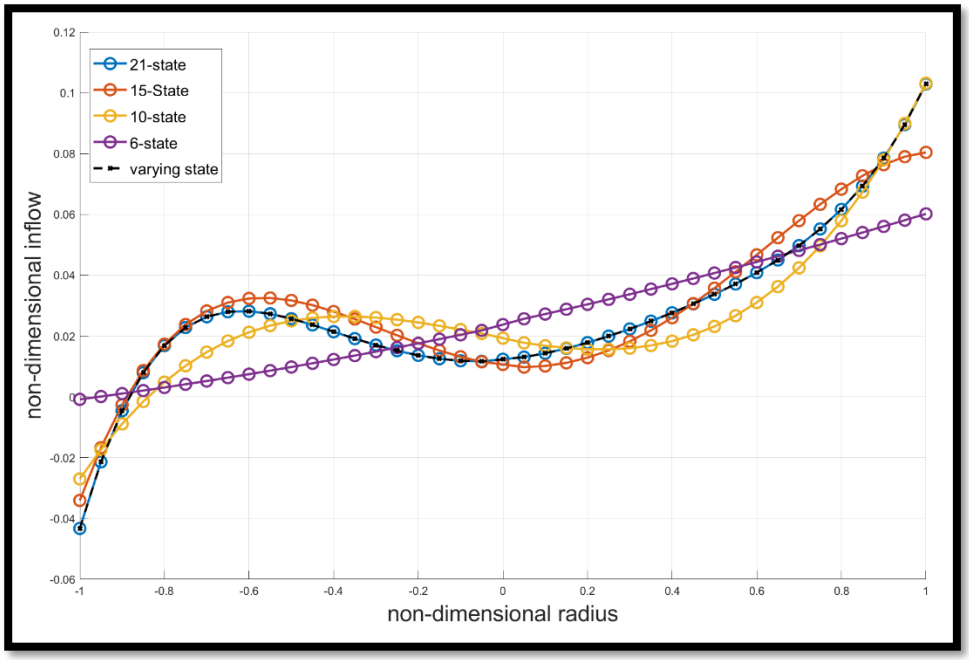

Figure B.10. $\mu = 0.3,\ \theta_0 = 8°, \theta_{1c} = 20°, \theta_{1s} = 0°$

C. ROTOR AIRFOIL SC1095

The airfoil data of the Helicopter S-76 is given as:

Table C.1 $Lift\ Coefficient\ Data\ (C_L)\ of\ the\ SC1095\ Airfoil$[23]

Aoa \ Mach	0	0.3	0.4	0.5	0.6	0.7	0.75	0.8	0.9	1	2
-180	0.000	0.000	0.00	0.00	0.00	0.00	0.00	0.00	0.00	0.00	0.00
-172	0.780	0.780	0.78	0.78	0.78	0.78	0.78	0.78	0.78	0.78	0.78
-160	0.640	0.640	0.64	0.64	0.64	0.64	0.64	0.64	0.64	0.64	0.64
-150	0.950	0.950	0.95	0.95	0.95	0.95	0.95	0.95	0.95	0.95	0.95
-30	-1.000	-1.000	-1.00	-1.00	-1.00	-1.00	-1.00	-0.95	-0.95	-0.95	-0.95
-15	-0.910	-0.910	-0.69	-0.79	-0.66	-0.75	-0.79	-0.81	-0.74	-0.71	-0.71
-10	-0.880	-0.880	-0.58	-0.72	-0.54	-0.66	-0.72	-0.81	-0.74	-0.63	-0.63
-8	-0.760	-0.760	-0.64	-0.72	-0.59	-0.71	-0.73	-0.75	-0.70	-0.62	-0.62
-6	-0.600	-0.600	-0.58	-0.61	-0.61	-0.74	-0.73	-0.69	-0.66	-0.62	-0.62
-5	-0.500	-0.500	-0.52	-0.52	-0.58	-0.72	-0.72	-0.58	-0.58	-0.52	-0.52
-3	-0.300	-0.300	-0.33	-0.48	-0.35	-0.52	-0.52	-0.36	-0.40	-0.33	-0.33
0	0.041	0.041	0.04	-0.04	0.08	-0.26	0.07	0.07	-0.15	-0.05	-0.05
2	0.269	0.269	0.29	0.26	0.36	-0.09	0.48	0.35	0.13	0.20	0.20
4	0.496	0.496	0.53	0.55	0.65	0.08	0.70	0.56	0.39	0.45	0.45
6	0.723	0.723	0.78	0.84	0.86	0.83	0.75	0.71	0.64	0.70	0.70
8	0.951	0.951	1.02	1.03	0.91	0.87	0.79	0.81	0.77	0.81	0.81
9	1.065	1.065	1.12	1.07	0.93	0.89	0.81	0.84	0.79	0.83	0.83
10	1.157	1.157	1.18	1.08	0.95	0.91	0.83	0.84	0.81	0.85	0.85
12	1.200	1.200	1.14	1.05	1.01	0.96	0.87	0.85	0.83	0.87	0.87
15	1.015	1.015	0.99	0.98	1.09	1.03	0.93	0.85	0.86	0.89	0.89
30	1.000	1.000	1.00	1.00	1.00	1.00	1.00	1.00	1.00	1.00	1.00
150	-0.950	-0.950	-0.95	-0.95	-0.95	-0.95	-0.95	-0.95	-0.95	-0.95	-0.95
156	-0.700	-0.700	-0.70	-0.70	-0.70	-0.70	-0.70	-0.70	-0.70	-0.70	-0.70
158	-0.660	-0.660	-0.66	-0.66	-0.66	-0.66	-0.66	-0.66	-0.66	-0.66	-0.66
160	-0.640	-0.640	-0.64	-0.64	-0.64	-0.64	-0.64	-0.64	-0.64	-0.64	-0.64
172	-0.780	-0.780	-0.78	-0.78	-0.78	-0.78	-0.78	-0.78	-0.78	-0.78	-0.78
180	0.000	0.000	0.00	0.00	0.00	0.00	0.00	0.00	0.00	0.00	0.00

Table C.2 $Drag\ Coefficient\ Data\ (C_D)\ of\ the\ SC1095\ Airfoil$[23]

Aoa\ Mach	0	0.3	0.4	0.5	0.6	0.7	0.75	0.8	0.9	1	2
-180	0.020	0.020	0.02	0.02	0.02	0.02	0.02	0.02	0.02	0.02	0.02
-179	0.025	0.025	0.03	0.03	0.03	0.03	0.03	0.03	0.03	0.03	0.03
-175	0.065	0.065	0.07	0.07	0.07	0.07	0.07	0.07	0.07	0.07	0.07
-172	0.110	0.110	0.11	0.11	0.11	0.11	0.11	0.11	0.11	0.11	0.11
-150	0.642	0.642	0.64	0.64	0.64	0.64	0.64	0.64	0.64	0.64	0.64
-115	1.880	1.880	1.88	1.88	1.88	1.88	1.88	1.88	1.88	1.88	1.88
-90	2.080	2.080	2.08	2.08	2.08	2.08	2.08	2.08	2.08	2.08	2.08
-65	1.880	1.880	1.88	1.88	1.88	1.88	1.88	1.88	1.88	1.88	1.88
-30	0.630	0.630	0.63	0.63	0.63	0.63	0.63	0.63	0.63	0.63	0.63
-10	0.210	0.210	0.22	0.02	0.02	0.21	0.19	0.23	0.26	0.30	0.30
-9	0.102	0.102	0.16	0.03	0.03	0.18	0.16	0.19	0.23	0.27	0.27
-8	0.042	0.042	0.10	0.05	0.04	0.15	0.14	0.16	0.20	0.25	0.25
-7	0.018	0.018	0.05	0.04	0.04	0.13	0.12	0.13	0.18	0.23	0.23
-6	0.011	0.011	0.02	0.02	0.04	0.10	0.09	0.10	0.15	0.20	0.20
-5	0.009	0.009	0.01	0.01	0.03	0.07	0.07	0.08	0.13	0.18	0.18
-4	0.009	0.009	0.01	0.01	0.01	0.04	0.05	0.07	0.12	0.15	0.15
-3	0.008	0.008	0.01	0.01	0.01	0.02	0.03	0.04	0.09	0.14	0.14
-1	0.009	0.009	0.01	0.01	0.01	0.01	0.01	0.03	0.06	0.10	0.10
0	0.008	0.008	0.01	0.01	0.01	0.01	0.01	0.02	0.05	0.09	0.09
1	0.009	0.009	0.01	0.01	0.01	0.01	0.01	0.03	0.06	0.10	0.10
2	0.009	0.009	0.01	0.01	0.01	0.01	0.02	0.04	0.08	0.12	0.12
3	0.009	0.009	0.01	0.01	0.01	0.02	0.05	0.07	0.10	0.14	0.14
4	0.010	0.010	0.01	0.01	0.01	0.04	0.07	0.09	0.12	0.15	0.15
5	0.011	0.011	0.01	0.01	0.02	0.07	0.09	0.11	0.14	0.18	0.18
6	0.014	0.014	0.01	0.01	0.04	0.09	0.11	0.13	0.17	0.20	0.20
7	0.019	0.019	0.01	0.02	0.07	0.12	0.14	0.15	0.19	0.23	0.23
8	0.037	0.037	0.01	0.03	0.09	0.14	0.16	0.17	0.21	0.25	0.25
9	0.100	0.100	0.02	0.06	0.11	0.16	0.18	0.20	0.24	0.27	0.27
10	0.210	0.210	0.02	0.09	0.13	0.19	0.21	0.23	0.26	0.30	0.30
15	0.315	0.315	0.22	0.24	0.23	0.31	0.32	0.34	0.37	0.41	0.38
30	0.630	0.630	0.63	0.63	0.63	0.63	0.63	0.63	0.63	0.63	0.63
65	1.880	1.880	1.88	1.88	1.88	1.88	1.88	1.88	1.88	1.88	1.88
90	2.080	2.080	2.08	2.08	2.08	2.08	2.08	2.08	2.08	2.08	2.08
150	0.640	0.640	0.64	0.64	0.64	0.64	0.64	0.64	0.64	0.64	0.64
172	0.110	0.110	0.11	0.11	0.11	0.11	0.11	0.11	0.11	0.11	0.11
175	0.065	0.065	0.07	0.07	0.07	0.07	0.07	0.07	0.07	0.07	0.07
179	0.025	0.025	0.03	0.03	0.03	0.03	0.03	0.03	0.03	0.03	0.03
180	0.020	0.020	0.02	0.02	0.02	0.02	0.02	0.02	0.02	0.02	0.02